



TECHNICAL UNIVERSITY OF CRETE
SCHOOL OF MINERAL RESOURCES ENGINEERING

POSTGRADUATE PROGRAM IN PETROLEUM ENGINEERING

**Advanced Numerical Methods for
Modeling Pressure Maintenance
Strategies during Secondary and
Tertiary Oil Recovery in Stratified
Petroleum Reservoirs**

Author:

Anastasia DOLLARI

Supervisor:

Nicolas KALOGERAKIS

February 15, 2018

Acknowledgments

I would like to express my sincere gratitude to Dr. Christos Chatzichristos and Dr. Andreas Yiotis for their valuable advice and support throughout the conduct of the current thesis. I would also like to thank NCSR Demokritos for giving me the opportunity to conduct my thesis there.

Finally, many thanks are addressed to my family and friends for their support.

Abstract

The current thesis focuses on the numerical modeling of pore-to-field scale couplings in hydrodynamic dispersion and immiscible flows in porous media using the standard finite element framework provided by the commercially available software COMSOL Multiphysics.

The single-phase flow is handled through the study of hydrodynamic dispersion during an ideal tracer injection by using COMSOL's readily available *Physics* interfaces. The coefficient of hydrodynamic dispersion is explicitly calculated through rigorous pore-scale simulations in 2D porous domains and from the results obtained, a homogeneous model for porous media is defined using the calculated effective transport properties. The upscaling from the pore-scale to the REV-scale as far as transport properties of the porous medium are concerned is evaluated through the hydrodynamic dispersion coefficient and an appropriate volume-averaged expression of the mass conservation equation. Results indicated that statistical properties conveniently derived at the REV-scale, can successfully be used for the precise calculation of pore-scale transport properties.

The two-phase incompressible flow during a waterflooding oil recovery process in a stratified petroleum reservoir is simulated via two numerical models; one that includes the gravitational terms and one that omits them. The equations of the mathematical flow model are derived under specific assumptions and formulated according to the fractional flow approach. The PDE modes in the general and coefficient form for time dependent analysis are utilized for their numerical implementation in COMSOL Multiphysics.

An appropriate, numerically stable, formulation of the black oil model is then used for the simulation of two-phase compressible flow during a waterflooding process in an undersaturated petroleum reservoir. The model is based on the oil phase pressure

and total velocity formulation. Its implementation in COMSOL is made with the time-dependent PDE interfaces.

The physical models of the waterflooding processes are also implemented in ECLIPSE 100 simulator and the results from the two simulators are compared so as to evaluate the performance of the newly-developed COMSOL PDE modules in quantifying and interpreting relevant physical phenomena. The results from the incompressible fluid flow modeling revealed that both COMSOL models are generally in good agreement with ECLIPSE 100 as far as recovery is concerned, with the COMSOL model that neglects the gravity exhibiting a better matching. The results obtained from the implemented formulation of the black oil model are also very close to the ones from ECLIPSE 100 regarding hydrocarbons production rates. That indicates that COMSOL Multiphysics can efficiently be used as a trustworthy tool in hydrocarbons recovery predictions and also for the solution of more complex physics phenomena in reservoir simulation problems.

Table of Contents

Acknowledgments	I
Abstract	III
1 Literature Review	1
1.1 Oil Recovery Techniques	1
1.1.1 Waterflooding	2
1.2 Tracers Injection for Reservoir Characterization	3
1.3 Hydrodynamic Dispersion	3
1.4 The Continuum Approach to Porous Media	5
2 The COMSOL Multiphysics Platform	6
2.1 Introduction	6
2.2 Equation Modeling with PDEs	7
2.3 The Finite Element Method	9
3 Modeling Hydrodynamic Dispersion	11
3.1 Introduction	11

3.2	Transport Equations	12
3.2.1	Single-Phase Flow	12
3.2.2	Transport of Diluted Species	13
3.2.3	Dispersion in a Single Capillary	14
3.3	Pore-scale Modeling	16
3.3.1	Model Implementation in COMSOL Multiphysics	16
3.3.2	Results and Discussion	18
3.4	REV-scale Modeling	23
3.4.1	Model Implementation in COMSOL Multiphysics	23
3.4.2	Results and Discussion	26
3.5	Conclusions	29
4	Modeling Two-phase Incompressible Flow	30
4.1	Introduction	30
4.2	Two-phase Fluid Flow in Porous Media	32
4.2.1	Two-phase Flow Equations	32
4.2.2	Fractional Flow Formulation	33
4.3	Model Implementation in COMSOL Multiphysics	34
4.3.1	Model including Gravity	36
4.3.2	Model neglecting Gravity	39
4.4	Results and Discussion	41
4.4.1	Model including Gravity	41
4.4.2	Model neglecting Gravity	50

4.4.3	Comparison with ECLIPSE 100	59
4.5	Conclusions	63
5	Modeling Multiphase Compressible Flow	64
5.1	Introduction	64
5.2	The Black Oil Model in Porous Media	65
5.2.1	Black Oil Model Equations	65
5.2.2	Phase Formulation	67
5.3	Model Implementation in COMSOL Multiphysics	68
5.4	Results and Discussion	74
5.4.1	The Black Oil Model in COMSOL	74
5.4.2	Comparison with ECLIPSE 100	82
5.5	Conclusions	87
6	Conclusions of MSc Thesis	88
	Bibliography	90
	List of Figures	92
	List of Tables	95

Chapter 1

Literature Review

1.1 Oil Recovery Techniques

Oil recovery operations traditionally have been subdivided into three stages: primary, secondary, and tertiary. Historically, these stages described the production from a reservoir in a chronological sense but due to the difficulty of chronological oil-production classification, classification based on process description is more useful and the generally accepted approach. Also, the designation of "enhanced oil recovery (EOR)" instead of "tertiary recovery" has become more accepted. ([Green and Willhite, 1998](#))

The recovery of oil by any of the natural drive mechanisms is called **primary recovery**. The term refers to the production of hydrocarbons from a reservoir without the use of any process (such as fluid injection) to supplement the natural energy of the reservoir. The overall performance of oil reservoirs is largely determined by the nature of energy, i.e., driving mechanism, available for moving the oil to the wellbore. There are basically six driving mechanisms; rock and liquid expansion drive, depletion drive (solution gas drive, dissolved gas drive or internal gas drive), gas-cap drive, water drive, gravity drainage drive, and combination drive. ([Ahmed, 2010](#))

When the natural energy of the reservoir is no longer enough to sustain the production of oil at the desired rates, other artificial means of injecting energy into the reservoir are then implemented. **Secondary recovery** results from the augmentation of natural energy through injection of water or gas to displace oil toward producing wells, although the term is now almost synonymous with waterflooding. Gas injection, in

this case, is either into a gas cap for pressure maintenance and gas cap expansion or into oil-column wells to displace oil immiscibly according to relative permeability and volumetric sweepout considerations. (Green and Willhite, 1998)

Gas processes based on other mechanisms, such as oil swelling, oil viscosity reduction, or favorable phase behavior, are classified as **EOR processes**. Hydrocarbon gases, CO₂, nitrogen, and flue gases are among the gases used. Injection of liquid chemicals such as polymers, surfactants and hydrocarbon solvents, and/or use of thermal energy are also included in the EOR processes. Thermal processes typically consist of the use of steam or hot water, or rely on the in-situ generation of thermal energy through oil combustion in the reservoir rock. (Green and Willhite, 1998) EOR is normally applied to recover more of the residual oil remaining in the reservoir after both primary and secondary recoveries have reached their economic limit.

In terms of oil recoverability, each reservoir is unique, but normally the primary production will be around 15-25% of the original oil in place (OOIP), while secondary IOR using conventional techniques will lie between 20-40% of the OOIP. EOR allows another 5% to 15% of the reservoir's oil to be recovered. Moreover, recent advances in reservoir technology have shown values of tertiary oil recovery estimated between 45-50% of OOIP. Values above 60% are very rare, but some mature fields in the Norwegian Sea were predicting recovery of 64% OOIP with a possible 75% using a miscible WAG process.

1.1.1 Waterflooding

Over the years, waterflooding has been the most widely used secondary oil recovery method after the exhaustion of the primary depletion energy of the reservoir. (Ogbeiwi et al., 2017) Waterflooding basically involves pumping water through an injection well into the reservoir. The water then forces itself through the pore spaces and sweeps the oil toward another set of wells known as producers. As a result, there is an increment in the total oil production from the reservoir. However, the percentage of water in the produced fluids steadily increases. On the average, this process can lead to the recovery of about one-third of the OOIP, leaving behind about two-thirds. (Meshioye et al., 2010)

The efficiency of an oil recovery method is to a large extent determined by physical mechanism at the microscopic level, e.g. how the phases oil, water and gas distribute in

the pore space of the geological rock. The front advance theory by Buckley and Leverett (1941) characterizes the macroscopic displacement mechanism in porous media at field scale. (Chen, 2000)

1.2 Tracers Injection for Reservoir Characterization

For the beneficial use of a secondary or EOR method it is of crucial importance that the reservoir geometry is known. The use of tracers in the reservoir studies shows that this is the best method to evaluate the downhole region of the well and interwell space. Traditionally, the reservoir studies have combined the integration of geological, geophysical, and well tests as well as geochemical data and production history to construct geologically realistic models. (Anisimov, 2009) Radioactive or chemical tracers are added to injected fluids in order to trace the flow pattern in a reservoir. It is feasible in many instances to design a tracer application, inject and recover tracer, and perform a complete numerical analysis during the planning stages of an EOR project. (Allison et al., 1991)

There are many processes during which tracers may be applied. Some commonly used applications during well drilling and completion is the measurement of mud water filtration, the study of the "near wellbore" chemical reactions and the measurement of the injectivity profiles. Tracers are also used extensively in reservoir evaluation through well-to-well flow studies for water and gas flooding for the measurement of properties of a reservoir segment. Furthermore, the determination of residual oil saturation from single well push and the study of surfactant and polymer behavior (EOR chemicals) under relevant reservoir conditions are carried out with the help of tracers. (Bjørnstad et al., 1990)

1.3 Hydrodynamic Dispersion

When two immiscible fluids with strong wettability preferences are pumped simultaneously through a porous medium, they tend to flow in separate channels and maintain their physical/flow characteristics, but with two miscible fluids no such separation is possible. Displacement in the case of immiscible fluids is generally not complete, but a fluid can be displaced completely from the pores by another injected fluid when miscible flow conditions are achieved (e.g. by the use of surfactants.) (Dullien,

1992)

In miscible displacement there is no capillarity; instead there is hydrodynamic mixing (so-called "dispersion") of the two fluids. As flow takes place the tracer (a certain mass of solute) gradually spreads and occupies an ever-increasing portion of the flow domain. It is a nonsteady, irreversible process (in the sense that the initial tracer distribution cannot be obtained by reversing the flow) in which the tracer mass mixes with the nonlabeled portion of the liquid. (Bear, 1972)

At the pore-scale there are two basic transport phenomena involved: convection and molecular diffusion. The complicated system of interconnected passages comprising the microstructure of the medium causes a continuous subdivision of the tracer's mass into finer offshoots. Variations in local velocity, both in magnitude and direction, along the tortuous flow paths and between adjacent flow paths as a result of the velocity distribution within each pore, cause any initial tracer mass within the flow domain to spread and occupy an ever-increasing volume of the porous medium. The two basic elements in this kind of mixing are, therefore, flow and the presence of the pore system through which flow takes place. In addition to inhomogeneity on this microscopic scale (presence of pores, grains, etc.) we may also have inhomogeneity on a macroscopic scale due to variations in permeability from one portion of the flow domain to the next. (Bear, 1972)

An additional mass transport phenomenon, which occurs simultaneously with mechanical dispersion, is that caused by molecular diffusion resulting from variations in tracer concentration within the liquid phase. Actually, the separation between the two processes is artificial, as hydrodynamic dispersion includes both processes in an inseparable form. However, molecular diffusion alone does take place also in the absence of motion (both in porous media and in a liquid continuum). Because molecular diffusion depends on time, its effects on the overall dispersion is more significant at low flow velocities. (Bear, 1972)

In a recovery process utilizing a zone of miscible fluid, there is the possibility of losing miscibility by dissipating the miscible fluid or by channeling or "fingering" through the miscible zone. On the other hand, dispersion may tend to damp-out viscous fingers which may be channeling through the miscible slug. Hence, dispersion may be detrimental or beneficial (if it prevents fingering through the miscible zone). (Perkins and Johnston, 1963)

1.4 The Continuum Approach to Porous Media

In all the above cases flow takes place through a porous medium. By introducing the term *porous medium*, and by considering *flow of fluids through a porous medium*, the concept of a continuum must also be introduced.

The necessity for continuum approach emanates from the intrinsic uncertainty in describing in an exact manner the geometry of the internal solid surfaces that bound the flow domain inside a porous medium for the purpose of meaningful and efficient field-scale simulations. The same difficulties are encountered when describing phenomena associated with the flow of fluids contained in the void space, such as motion, mass transport, etc. So, instead of treating the problems at the pore level, a different approach is adopted, statistical in nature, to derive information regarding the motion of a system composed of many pores. The transfer produced within individual pores is averaged and we pass to a higher level—that of a porous continuum (macroscopic level). Hence, the actual or internal pore structure of the medium is overlooked and it is regarded as a continuum. In order to describe the various transfer phenomena at this higher level, appropriate transfer coefficients need to be defined, such as hydrodynamic dispersivity (for mass conservation) and permeability (for momentum conservation). (Bear, 1972)

Now, the continuum approach can be applied to the dynamics of fluids in porous media. The variables and the parameters of the various fictitious continua, averaged over an REV, enable us to describe flow, and other phenomena within a porous medium domain, by means of partial differential equations (PDEs). Such equations describe what happens at every physical point in space and at every physical instant of time. (Bear, 1972)

Chapter 2

The COMSOL Multiphysics Platform

2.1 Introduction

COMSOL Multiphysics is a powerful interactive environment used to model and solve all kinds of scientific and engineering problems. Conventional models for one type of physics can be extended into multiphysics models that solve coupled physics phenomena.

With the built-in *physics interfaces* and the advanced support for material properties, models can be built by defining the relevant physical quantities (such as material properties, loads, constraints, sources, and fluxes) rather than by defining the underlying equations. These variables, expressions, or numbers are applied directly to solid and fluid domains, boundaries, edges, and points independently of the computational mesh. The COMSOL Multiphysics software then internally compiles a set of equations representing the entire model. Using these physics interfaces, various types of studies can be including:

- Stationary and time-dependent (transient) studies
- Linear and nonlinear studies
- Eigenfrequency, modal, and frequency response studies

When solving the models, the COMSOL Multiphysics software assembles and solves the problem using a set of advanced numerical analysis tools. The software runs the analysis together with adaptive meshing and error control using a variety of numerical solvers.

The power of COMSOL Multiphysics as a standalone product is accessed through a flexible graphical user interface (GUI), in applications created using the Application Builder, or by script programming in Java or the MATLAB language. Furthermore, the software creates *sequences* to record all steps that create the geometry, mesh, studies and solver settings, and visualization and results presentation. (Comsol, 2015)

The COMSOL Multiphysics software has been used for the simulation of multiphase fluid flow in porous media in many works. Bjørnarå and Aker (2008) evaluated the numerical performance (numerical stability and solving time) of various formulations for the two-phase incompressible immiscible flow in 2D and 1D simulations. Zhang (2011) also implemented a complete 2D simulation of waterflooding in COMSOL by transforming the problem into a dimensionless form, for the study of the upscaling of two-phase flows in petroleum reservoirs. A simplified version of the black oil model assuming incompressible fluids was implemented in COMSOL by Diaz-Viera et al. (2008) using a finite element approach for the simulation of a water coreflooding experiment through a sandstone core. The model was coupled with a multiphase, multicomponent transport model for the study of EOR processes at laboratory scale.

2.2 Equation Modeling with PDEs

The physics interfaces in COMSOL Multiphysics and add-on modules use PDEs as a mathematical model of physical reality. The PDE interfaces allow to specify all or part of the problem using PDEs. Different PDE interfaces are included for equation-based modeling, distinguished by the equation formulation used for entering the equations: Coefficient Form, General Form, and Weak Form.

The *General Form PDE* interface provides a general interface for specifying and solving PDEs in the general form. The format is closely related to the conservation laws that govern many areas of physics. For a single dependent variable u , the general form reads:

$$\begin{aligned} e_\alpha \frac{\partial^2 u}{\partial t^2} + d_\alpha \frac{\partial u}{\partial t} + \nabla \cdot \underline{\Gamma} &= f & \text{in } \Omega \\ -\underline{n} \cdot \underline{\Gamma} &= g - \mathbf{q}\mathbf{u} + \mathbf{h}^T \boldsymbol{\mu} & \text{on } \partial\Omega \\ 0 &= R & \text{on } \partial\Omega_c \\ u &= r & \text{on } \partial\Omega_d \end{aligned}$$

where

- Ω is the computational domain; the union of all domains
- $\partial\Omega$ is the domain boundary
- \underline{n} is the outward unit normal vector on $\partial\Omega$
- e_a is the mass coefficient
- d_a is a damping coefficient or mass coefficient
- $\underline{\Gamma}$ is the conservative flux term
- g is the boundary source term
- q is the boundary absorption coefficient

The first line (equation) is the PDE, which must be satisfied in Ω . The second, third, and fourth equations are the boundary conditions, which must hold on $\partial\Omega$. The second equation is a generalization of a Neumann boundary condition. The third equation is a general constraint, of which the Dirichlet boundary condition on the fourth line is a special case.

The terms $\underline{\Gamma}$, f , g , q , R , and r are user-defined coefficients. They can be functions of the spatial coordinates, the solution u , and the space derivatives of u , as well as of other predefined and user-defined variables. The coefficients f , g , q , R , and r are scalar, whereas $\underline{\Gamma}$ is the *flux vector*. The normal component of $\underline{\Gamma}$ is continuous across any surface in the interior of the domain, Ω .

Many PDEs originating from physics interfaces and other fields can be cast into a generic form containing derivatives up to second order in both time and space, but no mixed derivatives. In COMSOL Multiphysics, a PDE of this type is defined by specifying coefficients for the derivatives of different orders. This results in a *coefficient form PDE*, which for one dependent variable u reads:

$$\begin{aligned}
 e_\alpha \frac{\partial^2 u}{\partial t^2} + d_\alpha \frac{\partial u}{\partial t} + \nabla \cdot (-c \nabla u - \underline{\alpha} u + \underline{\gamma}) + \underline{\beta} \cdot \nabla u + \alpha u &= f && \text{in } \Omega \\
 -\underline{n} \cdot (c \nabla u + \alpha u - \underline{\gamma}) &= g - qu + h^T \mu && \text{on } \partial\Omega \\
 0 &= R && \text{on } \partial\Omega_c \\
 u &= r && \text{on } \partial\Omega_d
 \end{aligned}$$

where

- $\underline{\alpha}$ is the conservative flux convection coefficient

- $\underline{\beta}$ is the convection coefficient
- $\underline{\gamma}$ is the conservative flux source term
- α is the absorption coefficient

The first line is the PDE, which must be satisfied in Ω . The second and third equations are the boundary conditions, which must hold on $\partial\Omega$. The second equation is a generalization of a Neumann boundary condition. The third equation is a general constraint, with a Dirichlet boundary condition as a special case.

To define a PDE on coefficient form in one of the PDE interfaces, the coefficients $c, \underline{\alpha}, \underline{\gamma}, \underline{\beta}$, and α and the boundary terms f, g, R , and r are specified. They can all be functions of the spatial coordinates as well as of dependent variables and other predefined or user-defined variables and parameters. A PDE is guaranteed to be linear when the coefficients vary only with the spatial coordinates (or are constants). For a single dependent variable u , all the coefficients in the above equation are scalars except $\underline{\alpha}, \underline{\beta}$, and $\underline{\gamma}$, which are vectors with n components. The coefficient c may be given alternatively as a scalar or an n -by- n matrix to model anisotropic materials. ([Comsol, 2015](#))

2.3 The Finite Element Method

For the vast majority of geometries and problems, these PDEs cannot be solved with analytical methods. Instead, an approximation of the equations can be constructed, typically based upon different types of discretizations. These discretization methods approximate the PDEs with numerical model equations, which can be solved using numerical methods. The solution to the numerical model equations are, in turn, an approximation of the real solution to the PDEs. The finite element method (FEM) is used to compute such approximations in COMSOL Multiphysics.

The FEM subdivides an object into very small but finite-size elements. The physics of one element is approximately described by a finite number of degrees of freedom (DOFs). Each element is assigned a set of characteristic equations (describing physical properties, boundary conditions, and imposed forces), which are then solved as a set of simultaneous equations to predict the behavior of the object. ([Comsol, 2015](#)) These elements have the same properties with the original equations, but they are simpler to define and to reduce the number of unknowns.

The general steps of the FEM are described as follows: The first step consists in the division of the body in small elements. The type, size and number of elements are in the field of the engineer judgment but can be supported with research. Next step is to choose interpolation functions. It is defined in the element using the nodal values of the element. The most common functions are linear, quadratic and cubic polynomials, because they are simple to work with. The degree of the polynomial varies according to the number and nature of nodes of the elements and the unknowns at each node. The following step is to set the matrix equations. For this, various methods can be used. In order to obtain the final and global equation for the system, the next step is to collect and assemble the equations for the element properties. Previously to solving the system of equations, the equations have to be changed so that it can regard the boundary conditions. The assemblage results in a group of equation with unknown nodal values, degrees of freedom. The kind of equations to be solved depends on the type of problem and if it is time dependent or not. In the end, other parameters dependent of those calculated can be also obtained. Those parameters are also referred as derived values and can be volume, surface averages or integrations or simply just point evaluation of certain quantities. ([Huebner et al., 2008](#))

Chapter 3

Modeling Hydrodynamic Dispersion

3.1 Introduction

Hydrodynamic dispersion is a phenomenon that emanates at the microscopic (pore-scale) level and it is affected mainly by the actual pore structure. But due to the difficulty of describing the actual geometry of a pore, let alone the velocity regime that prevails and plays a determining role in a miscible displacement, these phenomena are usually approached in upscaled levels by simplifications associated with statistical properties.

In the current chapter, hydrodynamic dispersion is approached through two different scale modeling; the first in the pore-scale level where the process actually emanates and the second in the REV-scale level where the actual microscopic physics are expressed through a lumped parameter, i.e. the dispersivity tensor. The objective of this work is to demonstrate how the process can be modeled within an idealized actual pore structure using COMSOL and then can be adequately described by averaged properties of the upscaled level through the approach of a homogenized porous medium.

In both cases a slug of tracer is injected in the medium for a short time interval and it is carried towards the exit under the existing flow. The tracer is completely dissolved in the flow stream to form a solution and its concentration is spatially variable, but always at the dilute limit. The ideal tracer approximation is assumed sufficient in our case, namely that the tracer is inert with respect to its liquid and solid surroundings and that it does not affect the liquid's properties (density and viscosity). Hence, the flow regime (i.e., velocity distribution) that depends on these properties does not change.

For the microscopic modeling a realistic microstructure geometry is created. The precise pore-scale velocity profile is computed from the *Laminar Flow* interface and the transport of the tracer is modeled with the *Transport of Diluted Species in Porous Media* interface. The hydrodynamic dispersion coefficient is computed by the coupling of the two interfaces.

In the macroscopic modeling the treatment of hydrodynamic dispersion is examined in a capillary tube, which is one of the simplest porous medium models commonly used. The reason is twofold. First, the phenomenological equations describing dispersion are often the same as in the case of a porous medium. Second, dispersion in a capillary tube the mechanism of which is relatively well understood, plays a role in determining dispersion in porous media (Dullien, 1992). Usually the exact velocity profile is neglected at the pore scale and a flat (piston-like) velocity profile is assumed. The dispersion coefficient tensor is evaluated from the rigorous pore-scale modeling and is now entered as an input in the *Transport of Diluted Species in Porous Media* interface, so as to compute the hydrodynamic dispersion coefficient using average properties.

3.2 Transport Equations

3.2.1 Single-Phase Flow

The *Laminar Flow* interface is used to compute the velocity and pressure fields for the flow of a single-phase fluid in the laminar flow regime. A flow remains laminar as long as the Reynolds number is below a certain critical value. At higher Reynolds numbers, disturbances have a tendency to grow and cause transition to turbulence. The equations solved by this physics interface are the Navier-Stokes (NS) equations for conservation of momentum and the continuity equation for conservation of mass.

The NS equations govern the motion of fluids and can be seen as Newton's second law of motion for fluids. In the case of a compressible Newtonian fluid, this yields:

$$\rho \left(\frac{\partial \underline{\mathbf{u}}}{\partial t} + \underline{\mathbf{u}} \cdot \nabla \underline{\mathbf{u}} \right) = -\nabla p + \nabla \cdot \left(\mu (\nabla \underline{\mathbf{u}} + (\nabla \underline{\mathbf{u}})^T) \right) - \frac{2}{3} \mu (\nabla \cdot \underline{\mathbf{u}}) \underline{\mathbf{I}} + \underline{\mathbf{F}} \quad (3.2.1)$$

Eq. (3.2.1) includes these quantities (with the SI unit in parentheses):

- $\underline{\mathbf{u}}$ is the fluid's velocity (m/s)
- p is the fluid's pressure (Pa)

- ρ is the fluid's density (kg/m^3)
- μ is the fluid's dynamic viscosity ($\text{Pa} \cdot \text{s}$)

The different terms correspond to the inertial forces, pressure forces, viscous forces and the external forces applied to the fluid. The NS equations were derived by Navier, Poisson, Saint-Venant and Stokes between 1827 and 1845.

These equations are always solved together with the continuity equation:

$$\frac{\partial \rho}{\partial t} + \nabla \cdot (\rho \underline{\mathbf{u}}) = 0 \quad (3.2.2)$$

When the temperature variations in a flow are small, a single-phase fluid can often be assumed incompressible; that is ρ is constant or nearly constant. In that case, [Eq. \(3.2.2\)](#) reduces to:

$$\nabla \cdot \underline{\mathbf{u}} = 0 \quad (3.2.3)$$

Because the divergence of the velocity is equal to zero, the following term:

$$-\frac{2}{3}\mu(\nabla \cdot \underline{\mathbf{u}})\underline{\mathbf{I}} \quad (3.2.4)$$

is removed from the viscous force term in the NS equations. ([Comsol, 2015](#))

In steady state conditions the transient term in the left part of [Eq. \(3.2.1\)](#) is also removed. The NS equations are, hence, reduced to:

$$\rho(\underline{\mathbf{u}} \cdot \nabla)\underline{\mathbf{u}} = -\nabla p + \nabla \cdot (\mu(\nabla \underline{\mathbf{u}} + (\nabla \underline{\mathbf{u}})^T)) + \underline{\mathbf{F}} \quad (3.2.5)$$

3.2.2 Transport of Diluted Species

The *Transport of Diluted Species in Porous Media* interface provides a predefined modeling environment for studying the evolution of chemical species transported by diffusion and convection. The physics interface assumes that all species present are dilute; that is, that their concentration is small compared to a solvent fluid or solid.

This interface is used to calculate the species concentration and transport in free and porous media. At the pore space, the transport of the diluted species is governed by diffusion and convection as described by the mass balance equation:

$$\frac{\partial c}{\partial t} + \underline{\mathbf{u}} \cdot \nabla c = \nabla \cdot (D \nabla c) + R \quad (3.2.6)$$

Eq. (3.2.6) includes these quantities (with the SI unit in parentheses):

- c is the concentration of the species (mol/m^3)
- D denotes the diffusion coefficient (m^2/s)
- R is the reaction rate expression for the species ($\text{mol}/(\text{m}^3 \cdot \text{s})$)
- \underline{u} is the velocity vector (m/s)

The diffusion process can be anisotropic, in which case D is a tensor.

The first term on the left-hand side corresponds to the accumulation (or indeed consumption) of the species. The second term accounts for the convective transport due to a velocity field \underline{u} . This field can be expressed analytically or obtained from coupling this physics interface to one that describes fluid flow. The mass balance equation is presented with a non-conservative formulation of the convective term in the case of incompressible flow. On the right-hand side of Eq. (3.2.6), the first term describes the diffusion transport, accounting for interaction between the dilute species and the solvent. The second term represents a source or sink term, typically due to a chemical reaction. (Comsol, 2015)

3.2.3 Dispersion in a Single Capillary

The concentration c of the tracer is described by the two-dimensional, unsteady, convective, diffusion equation in cylindrical coordinates:

$$\frac{\partial c}{\partial t} + u(r) \frac{\partial c}{\partial x} = \mathcal{D} \left(\frac{\partial^2 c}{\partial x^2} + \frac{1}{r} \frac{\partial}{\partial r} r \frac{\partial c}{\partial r} \right), \quad (3.2.7)$$

where $u(r)$ is the parabolic laminar velocity profile. It has been assumed that \mathcal{D} , the molecular diffusion coefficient, is constant.

By sufficiently large values of time, Taylor showed that the process could be described by a one-dimensional advection dispersion equation as follows:

$$\frac{\partial \bar{c}}{\partial t} + \bar{u} \frac{\partial \bar{c}}{\partial x} = D_{ct} \frac{\partial^2 \bar{c}}{\partial x^2}, \quad (3.2.8)$$

where \bar{c} is the average tracer concentration at distance x and time t , and the molecular diffusion coefficient has been replaced by an effective axial diffusion coefficient or "coefficient of hydrodynamic dispersion" D_{ct} (ct designates "capillary tube").

Upon defining a coordinate x' that moves with the mean speed of flow as

$$x' = x - \bar{u}t, \quad (3.2.9)$$

Eq. (3.2.8) becomes

$$\frac{\partial \bar{c}}{\partial t} = D_{ct} \frac{\partial^2 \bar{c}}{\partial x'^2} \quad (3.2.10)$$

and, therefore, Eq. (3.2.10) is simply the one-dimensional unsteady diffusion equation.

The solution of this equation, known as Fick's second law of diffusion, is well known for the case under consideration:

$$\frac{\bar{c}}{c_0} = \frac{1}{2(\pi D_{ct} t)^{1/2}} \exp \left[-\frac{(x - \bar{u}t)^2}{4D_{ct} t} \right], \quad (3.2.11)$$

where c_0 is the initial tracer concentration in the slug and $D_{ct} = \sigma_x^2/2t$ with σ_x the standard deviation of the Gaussian distribution of the tracer concentration. (Dullien, 1992)

The spreading of the tracer is due to mechanical mixing and diffusion, so the hydrodynamic dispersion coefficient is actually the summation of the dispersion coefficient D_D and the effective diffusion coefficient D_e .

$$D_{ct} = D_D + D_e \quad (3.2.12)$$

The effective diffusion in porous media depends on the structure of the porous material and the phases involved. For single-phase flow, in the case of free flow the effective diffusivity is simply equal to the molecular diffusivity $D_e = \mathcal{D}$ while in the case of a saturated porous media it is defined as:

$$D_e = \frac{\phi}{\tau} \mathcal{D} \quad (3.2.13)$$

where τ is the tortuosity factor (dimensionless).

The tortuosity factor accounts for the reduced diffusivity due to the fact that the solid grains impede Brownian motion. The *Transport of Diluted Species in Porous Media* interface provides predefined expressions to compute the tortuosity factors to the Millington and Quirk model:

$$\tau = \phi^{-1/3} \quad (3.2.14)$$

and Bruggeman model: (Comsol, 2015)

$$\tau = \phi^{-1/2} \quad (3.2.15)$$

3.3 Pore-scale Modeling

3.3.1 Model Implementation in COMSOL Multiphysics

The dispersion process is examined in model (idealized) porous structure. Fig. 3.1 illustrates the 2D detailed geometry that exhibits infinite periodicity in the x-direction. The porous height is 6.1 mm and the width 0.6 mm. The square - shaped obstacles represent the parts of the porous where no flow occurs. There are twenty obstacles with side of 0.2 mm each, spread at equal distances to mimic the heterogeneity of the system.

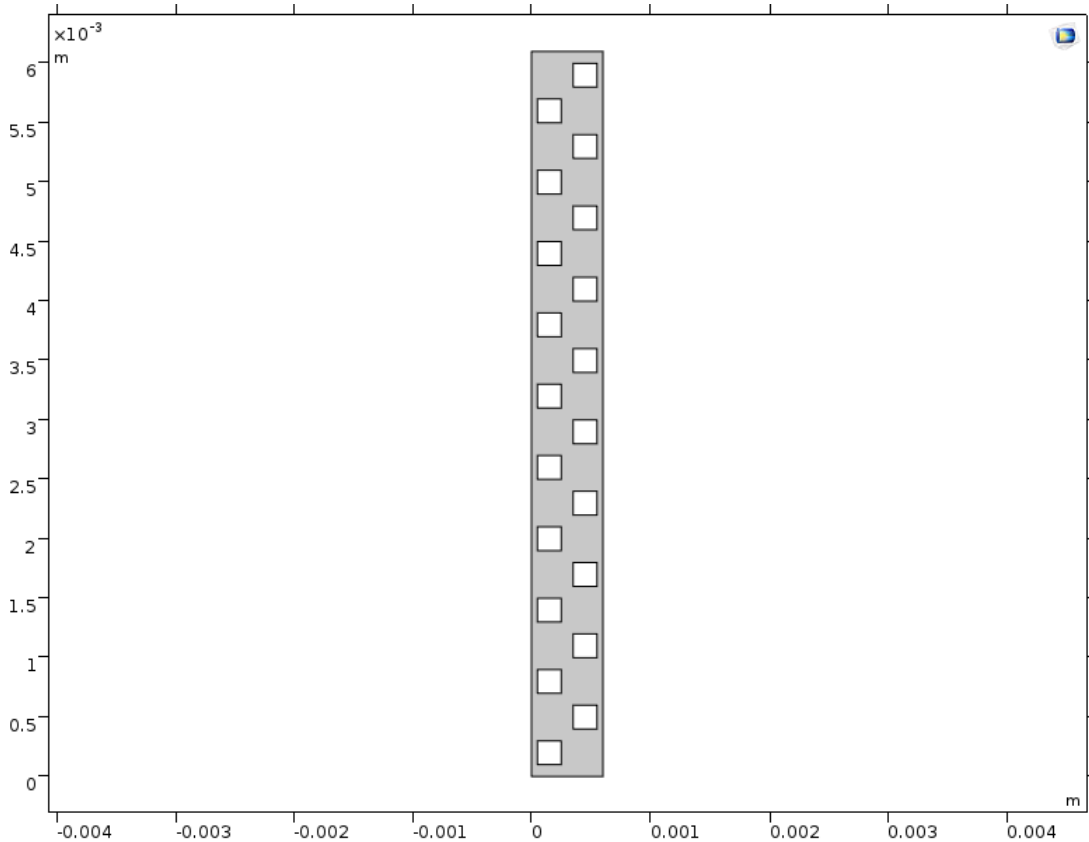


Figure 3.1: Artificial porous structure.

Parameters of the 2D detailed geometry are listed in the following table.

Parameters	Units	Values
Initial pressure, p_0	Pa	10^5
Water density, ρ	kg/m^3	1000
Water dynamic viscosity, μ	$\text{Pa} \cdot \text{s}$	10^{-3}
Inflow velocity, u_{in}	m/s	$4.88 \cdot 10^{-5}$
Initial concentration, c_0	mol/m^3	0
Molecular diffusion coefficient, \mathcal{D}	m^2/s	$8 \cdot 10^{-10}$
Reynolds number, Re	-	0.01
Peclet number, Pe	-	15.61

Table 3.1: Parameters for the pore-scale modeling.

Laminar Flow Interface

The NS equations are solved neglecting the gravity forces as a stationary problem. The initial pressure is specified. The fluid enters the capillary from the down side with a normal inflow velocity and exits the capillary from the up side due to suppressed backflow. Periodic flow conditions are specified at the side walls of the capillary. The periodicity splits each selection into a source group (src) and a destination group (dst). Fluid that leaves the domain through one of the destination boundaries enters the domain through the corresponding source boundary. The geometry is a periodic part of a larger geometry.

Transport of Diluted Species in Porous Medium Interface

The mass balance equation is solved as a time-dependent problem for a range of (0,1,25,125) seconds. The only additional transport mechanism apart from diffusion is convection. The initial concentration is inserted. The concentration in the inflow boundary is approximated by a Dirac delta function $c_{\text{in}} = \text{rect}1(t[1/\text{s}] - 12.5)$ with an interval of 1 second. The velocity field is computed from the *Laminar Flow* interface. The molecular diffusion coefficient is set isotropic as it is assumed to be constant because the solution is very dilute and contain isotope tracers, in which \mathcal{D} is concentration independent. Periodic conditions are applied to the side walls.

Initial Conditions

$$\begin{aligned}\underline{\mathbf{u}}(t_0) &= \underline{\mathbf{u}}_{\text{in}}, \quad p(t_0) = p_0 \\ c(t_0) &= c_0\end{aligned}$$

Boundary Conditions

Inlet conditions

$$\begin{aligned}\underline{\mathbf{u}} &= -\underline{\mathbf{u}}_{\text{in}}\underline{\mathbf{n}} \\ c &= c_{\text{in}}\end{aligned}$$

Outlet conditions

$$\begin{aligned}\left[-p\underline{\mathbf{I}} + (\mu(\nabla\underline{\mathbf{u}} + (\nabla\underline{\mathbf{u}})^T))\right]\underline{\mathbf{n}} &\leq -p_0\underline{\mathbf{n}} \\ -\underline{\mathbf{n}} \cdot \mathcal{D}\nabla c &= 0\end{aligned}$$

Side walls

$$\begin{aligned}\underline{\mathbf{u}}_{\text{src}} &= \underline{\mathbf{u}}_{\text{dst}}, \quad p_{\text{src}} = p_{\text{dst}} \\ c_{\text{src}} &= c_{\text{dst}}\end{aligned}$$

Mesh and Solver

A free triangular mesh with maximum element size $2.7 \cdot 10^{-5}$ m is applied. The fully-coupled stationary and fully-coupled time-dependent solvers are used. The time stepping in the time-dependent solver is selected to be intermediate.

3.3.2 Results and Discussion

[Fig. 3.2](#) illustrates the velocity magnitude in the microscopic level for a Peclet number 15.61.

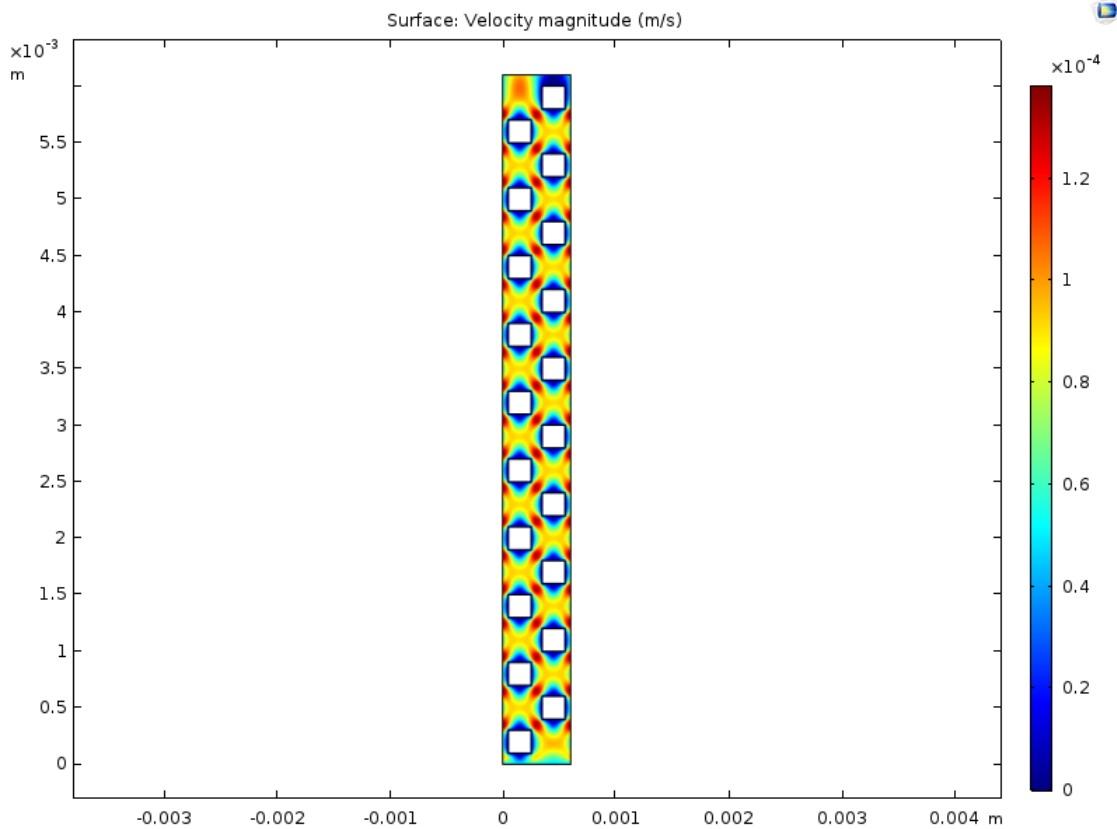


Figure 3.2: Velocity magnitude in the artificial porous structure; surface plot.

The fluid enters the domain with a constant inflow velocity, but the existing solid parts create a broad velocity distribution both in magnitude and direction. It is observed that between the edges of the obstacles the velocity is greater due to greater local pressure drop while around the sides of the obstacles the velocity magnitude is smaller due to the no slip boundary condition. The continuity of the velocity field across the boundaries where periodicity is applied is visually confirmed in the above figure.

The broad distribution is pointed out with the use of arrow surface plots in the zoomed area.

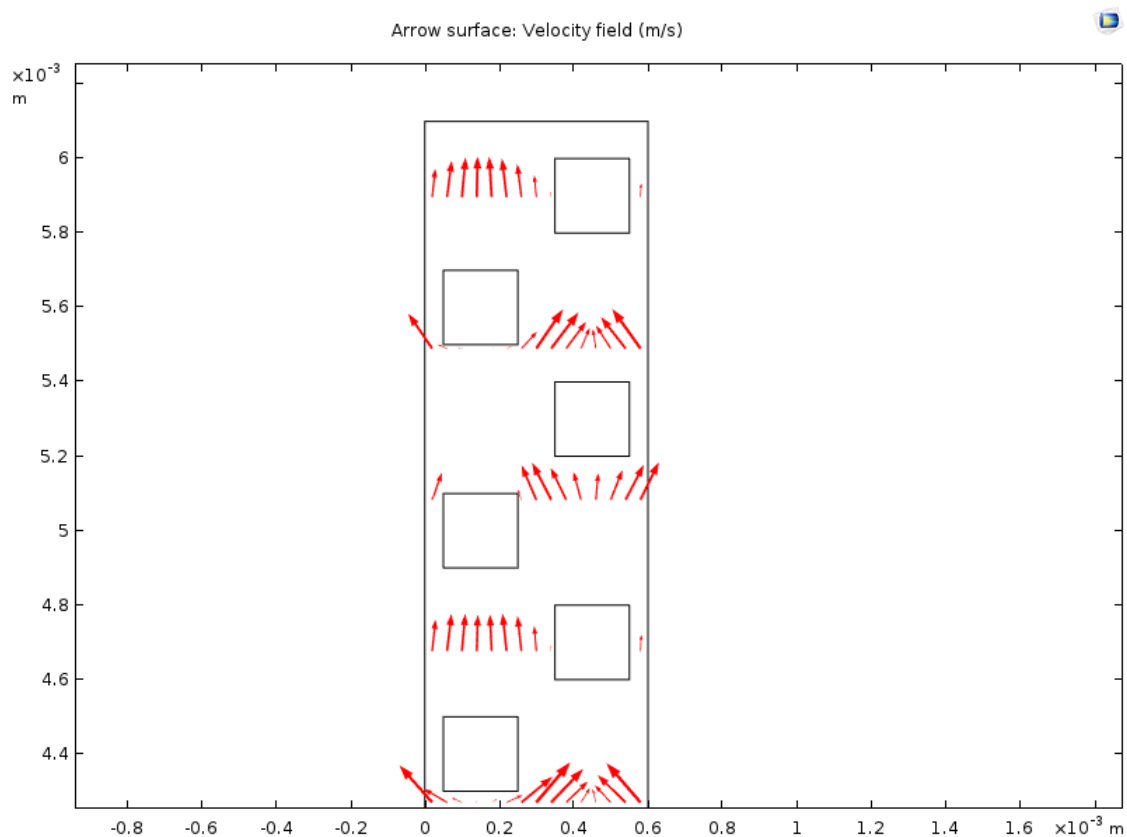


Figure 3.3: Velocity field in a zoomed area of the artificial porous structure; arrow surface plot.

The greater velocity magnitude is visualized with the longer arrows and it is detected near the edges of the obstacles where the space is narrower. The size of the arrows is smaller near the sides of the obstacles due to the no slip boundary. The local variations of the velocity direction can also be distinct with the use of the arrows. The existing solid particles in the main direction force the fluid to flow around them so as to continue traveling towards the outlet. The flow around the two sides of the obstacles exists due to the periodic flow conditions and the continuous velocity vector.

The concentration profile of the tracer for various times after the injection is presented in [Fig. 3.4](#) for the microscopic level modeling.

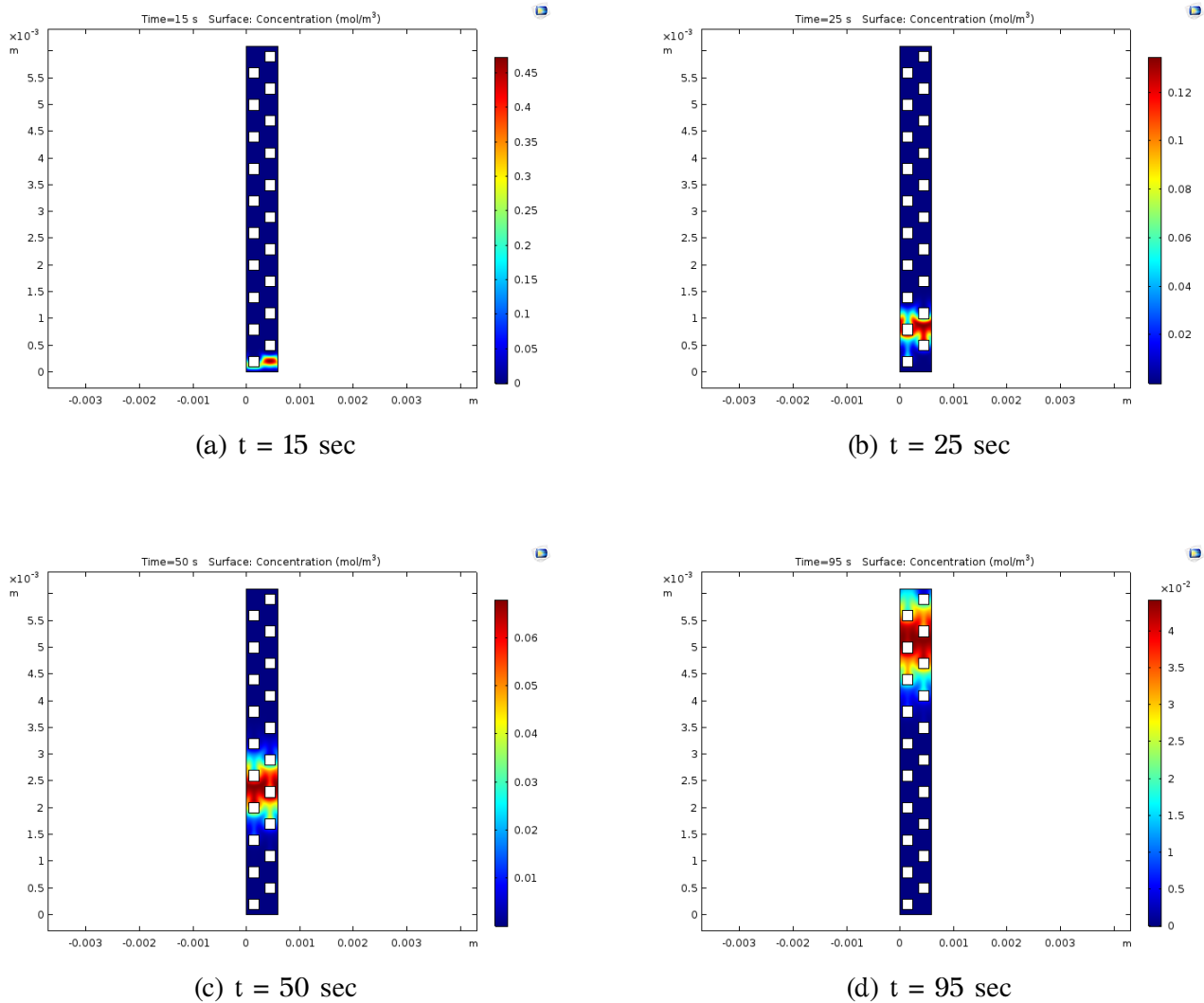


Figure 3.4: Tracer concentration profile at different times in the artificial porous structure.

The slug is injected into the fluid, which is in fully developed laminar flow. The spreading of the tracer follows an unsymmetrical manner towards all the directions due to variations in local velocity, as explained before. Generally a tracer spreads out faster in the direction of flow than in the transverse direction. But due to the mixing by molecular diffusion in the radial direction the tracer concentration over the pore cross section is gradually equalized and its distribution is kept more compact. The periodicity allows the spread of the tracer mass also across the side boundaries.

The next figure illustrates the tracer's average concentration along the principal axis of the flow at different times. The average concentration is computed using a *Linear Projection* operator.

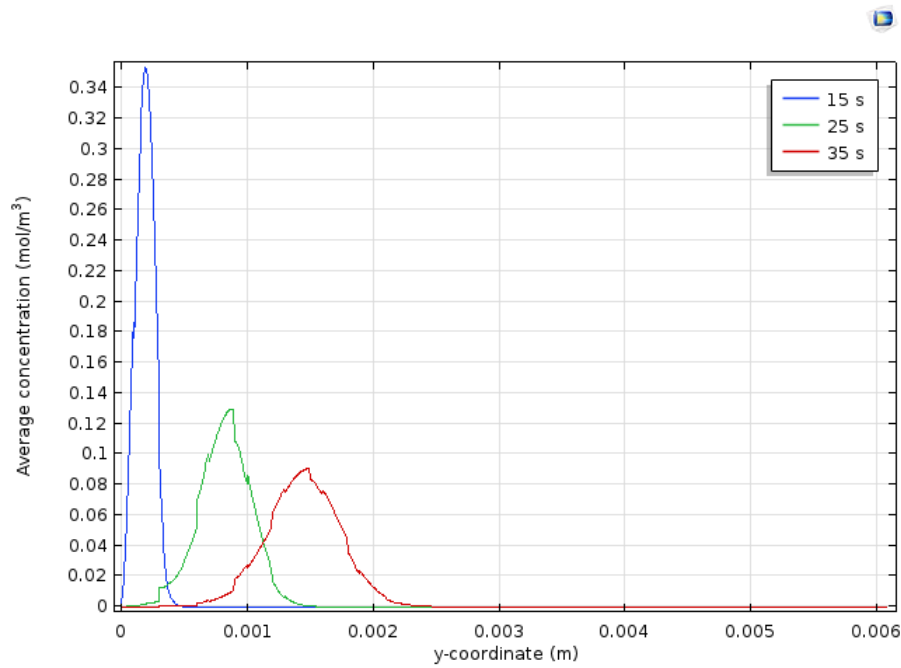


Figure 3.5: Average tracer concentration at different times for the pore-scale modeling.

As it can be observed, the tracer's spreading with time follows practically a normal distribution with increasing variance in the downstream direction, hence the hydrodynamic dispersion coefficient can be approached from the formulation $D_{ct} = \sigma_x^2/2t$, following Taylor's theory for flow in a single capillary described by a parabolic velocity field. The concentration distributions are not so smooth because the existence of a finite number of obstacles in the detailed geometry results in the velocity field shown previously which causes the unsymmetrical spread of the tracer across the primary axis.

In order to identify the standard deviation of each Gaussian profile the curve fitting tool of MATLAB is used. For three time values selected arbitrarily, the data derived from the COMSOL Multiphysics plots are introduced in MATLAB and are fitted to the Gaussian distribution. For the estimated standard deviation in each set of data, the corresponding coefficients of hydrodynamic dispersion are computed and presented below.

Time (s)	D_{ct} (10^{-9} m ² /s)
15	1.16
25	1.58
35	1.75

Table 3.2: Hydrodynamic dispersion coefficient at different times in the pore-scale modeling.

The above values are used for the calculation of the dispersivity tensor that must be inserted as input in the homogenized porous medium modeling for the upscaling in the macroscopic level.

3.4 REV-scale Modeling

3.4.1 Model Implementation in COMSOL Multiphysics

The dispersion process is also studied using the approximation of a homogenized capillary tube of the same dimensions. [Fig. 3.6](#) illustrates the 2D model geometry.

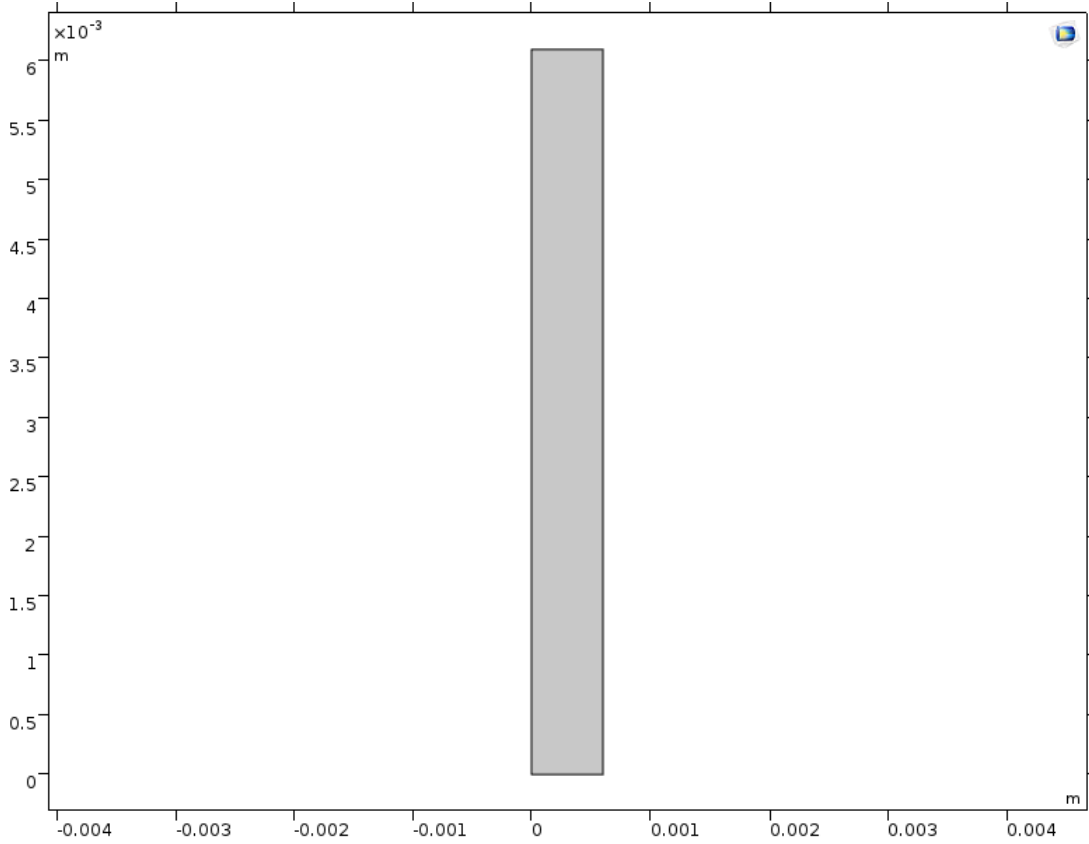


Figure 3.6: Homogeneous porous medium.

This time the actual porous structure is neglected so the average porosity and the effective properties are computed from the pore-scale modeling and introduced as parameters.

The porosity of the detailed model is computed by integrating the value 1 over the structure and then divide this by the length and width of the structure.

$$\phi = \frac{1}{L_0 L_1} \int_0^{L_1} \int_0^{L_0} 1 dx dy = 0.78 \quad (3.4.1)$$

The dispersion coefficient is computed from [Eq. \(3.2.12\)](#) as following:

$$D_D = D_{ct} - D_e$$

The values of the hydrodynamic dispersion coefficient that have been calculated explicitly with rigorous pore-scale modeling are used. The other parameter that needs to be computed is the effective diffusivity, for which the average porosity, the tortuosity factor and the molecular diffusivity must be known. The average porosity has been calculated

as shown above. The tortuosity factor is approximately evaluated using one of the provided tortuosity models, the Millington and Quirk one in this case. The molecular diffusivity is the same.

$$D_e = \frac{\phi}{\tau} \mathcal{D} = \frac{\phi}{\phi^{-1/3}} \mathcal{D} = 5.76 \cdot 10^{-10} \text{ m}^2/\text{s}$$

Now, the dispersion coefficient for various times can be computed.

Time (s)	D_{ct} (10^{-9} m ² /s)	D_D (10^{-10} m ² /s)
15	1.16	5.88
25	1.58	10.0
35	1.75	11.8

Table 3.3: Dispersion coefficient at different times.

The average value of $9.23 \cdot 10^{-10} \text{ m}^2/\text{s}$ is inserted as input in the *Transport of Diluted Species in Porous Medium* interface.

All the parameters for the macroscopic modeling are listed below.

Parameters	Units	Values
Initial pressure, p_0	Pa	10^5
Water density, ρ	kg/m ³	10^3
Water dynamic viscosity, μ	Pa · s	10^{-3}
Inflow velocity, u_{in}	m/s	$4.88 \cdot 10^{-5}$
Initial concentration, c_0	mol/m ³	0
Molecular diffusion coefficient, \mathcal{D}	m ² /s	$8 \cdot 10^{-10}$
Porosity, ϕ	-	0.78
Dispersion coefficient, D_D	m ² /s	$9.23 \cdot 10^{-10}$

Table 3.4: Parameters for the REV-scale modeling.

Transport of Diluted Species in Porous Medium Interface

The mass conservation equation is solved with a set of boundary conditions as a time-dependent problem for the same time range. Convection and mass transfer in porous media (dispersion) are the additional transport mechanisms. The initial tracer

concentration is inserted. The concentration in the inflow boundary is approached by the same Dirac delta function as in the previous case: $c_{in} = \text{rect1}(t[1/s] - 12.5)$ with an interval of 1 second. The velocity field is specified by the inflow velocity. The fluid diffusion coefficient and the dispersion coefficient are also introduced while the Millington and Quirk model for the effective diffusivity is selected. Periodic conditions are applied to the side walls.

Initial Conditions

$$c(t_0) = c_0$$

Boundary Conditions

Inlet conditions

$$c = c_{in}$$

Outlet conditions

$$-\underline{n} \cdot D_{ct} \nabla c = 0$$

Side walls

$$c_{src} = c_{dst}$$

Mesh and Solver

A free triangular mesh with maximum element size $6.1 \cdot 10^{-5}$ m is applied. The fully-coupled time-dependent solver is selected, with an intermediate time stepping.

3.4.2 Results and Discussion

The concentration profile of the tracer in the macroscopic level is presented for various times after the injection in the following set of figures.

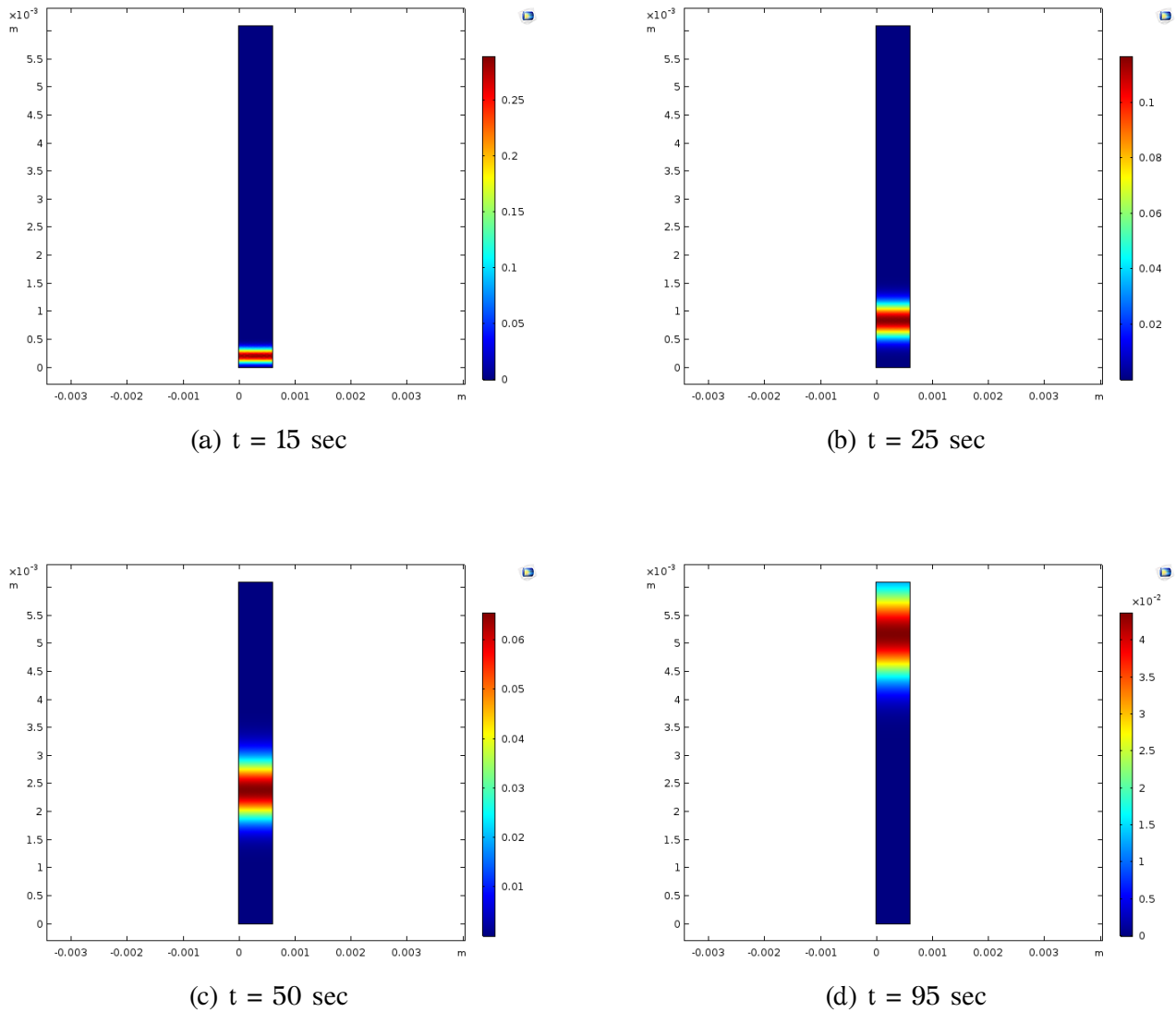


Figure 3.7: Tracer concentration profile at different times in the homogeneous porous medium.

In the homogeneous porous medium approach, the velocity field is specified by the inflow velocity which means that a flat velocity profile prevails. That leads to a symmetrical spreading of the tracer mass in the principal axis. The length of the mixed zone is increasing symmetrically on both sides of the tracer concentration, with the maximum concentration in the middle of the slug. Furthermore, the tracer concentration is steady with respect to the radial axis throughout the whole injection process.

Fig. 3.8 illustrates the tracer's average concentration along the principal axis of the tube at different times.

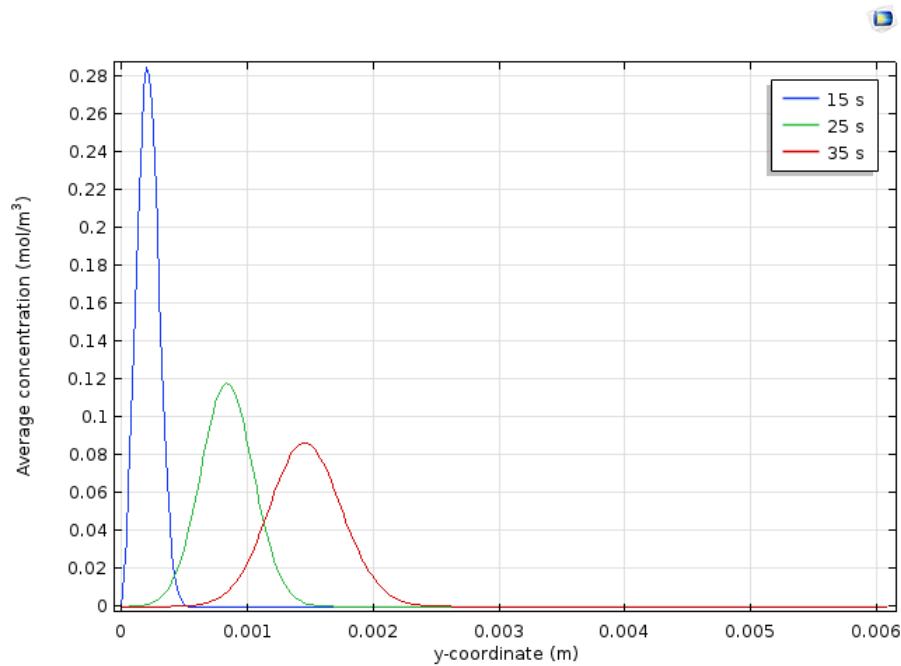


Figure 3.8: Average tracer concentration at different times for the REV-scale modeling.

As expected, the spreading of the species follows a Gaussian distribution and hence the coefficient of hydrodynamic dispersion can be evaluated using the formulation $D_{ct} = \sigma_x^2/2t$ and with the use of MATLAB, as described in the previous modeling. The concentration distribution is clearly smoother compared to the one in the detailed geometry, as in this case the flat velocity profile prevailing causes the spread of the tracer in a symmetrical manner.

The evaluated coefficients in the REV-scale modeling are presented in the next table. Presented are also the coefficients computed from the rigorous pore-scale modeling for comparison reasons.

Time (s)	D_{ct} (10^{-9} m ² /s)	
	Pore-scale modeling	REV-scale modeling
15	1.16	1.57
25	1.58	1.76
35	1.75	1.82

Table 3.5: Hydrodynamic dispersion coefficients at different times for the two models.

The values of the hydrodynamic dispersion coefficient calculated with the approach of the homogeneous porous medium for different times exceed only slightly the ones evaluated with the rigorous pore-scale modeling. The difference between the two calculated values becomes smaller as time passes. As a general picture, the approach seems to describe sufficiently enough the phenomenon taking place in the microscopic level.

3.5 Conclusions

In this chapter two numerical models were implemented in COMSOL Multiphysics so as to evaluate the effectiveness of the upscaling from pore-scale to REV-scale through the calculation of the hydrodynamic dispersion coefficient. For geologic scale computations the microscopic flow pattern within the actual pore geometry can not be used in an efficient manner so the approach of neglecting it in the macroscopic level can be considered valid, according to the results presented above. Statistical properties, as the average porosity and the effective diffusivity conveniently derived at the REV-scale, can successfully be used for the precise calculation of pore-scale transport properties, as the hydrodynamic dispersion coefficient.

Chapter 4

Modeling Two-phase Incompressible Flow

4.1 Introduction

Waterflooding is one of the most commonly used secondary techniques for the production of hydrocarbons from a reservoir. The water is injected in the reservoir through the perforations of a well, the so-called injection well, and causes the hydrocarbons to be immiscibly displaced and finally produced. This process is significantly enhanced due to buoyancy that leads to accumulation of injected water in the bottom part of the reservoir thus pushing the lighter oil towards the surface and production wells. For simplification reasons, the properties of the fluids are considered constant and independent of pressure in many two-phase flow simulation studies, and the flow is characterized as incompressible in that case. The modeling of the two-phase incompressible flow in the porous media when such a process takes place is studied in the current chapter with two different models, one that takes into account the gravitational terms (thus buoyancy induced separation of the phases) and one that neglects them.

The finite element scheme is used as a discretization scheme of the considered model equations. Given that such processes are dominated by flow and convection of the interface of the two phases, the numerical solution can be numerically unstable due to very steep interface gradients and thus the equations are manipulated in different ways in order to obtain accurate results. In the current study, the fractional flow formulation is selected as it has proven to be the fastest and most robust formulation

among others for the simulation of two-phase fluid flow in porous medium, according to Bjørnarå and Aker (2008). The set of equations consists of one pressure equation and one saturation equation. Two different models are then derived and implemented in COMSOL MultiPhysics, one with the presence of gravity and one with the absence of gravity, so as to make distinct the effect that the gravity has on the numerical predictions for the same conceptual model.

The transport mechanisms are usually modeled in an inverted five-spot pattern, namely an injection pattern in which four production wells are located at the corners of a square and the injection well sits in the center. The injection fluid is injected through the injection well to displace the oil toward the four production wells. A schematic of the alternating rows of production and injection wells is presented below. The symmetry of the system means that the flow between any two wells can be modeled by placing the wells at opposite corners of a Cartesian grid. This reservoir pattern is referred to as a quarter five-spot calculation and is the one used for the modeling of the waterflooding.

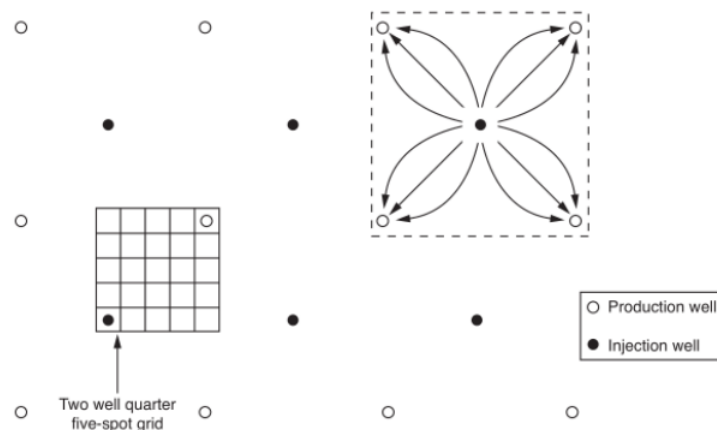


Figure 4.1: The inverted five-spot network (Institute of Petroleum Engineering Heriot-Watt, 2010)

Finally, the efficiency of the two COMSOL models on predicting the hydrocarbons production during oil recovery in a stratified reservoir is evaluated through the comparison with the ECLIPSE 100 simulator.

4.2 Two-phase Fluid Flow in Porous Media

4.2.1 Two-phase Flow Equations

The system of equations consists of mass balances; PDEs that describe the accumulation, transport and injection/production of the phases in the model. In addition, several auxiliary equations apply to the system, coupling different phases in the system together. (Bjørnarå and Aker, 2008)

The mass balance equation of each phase $\alpha = w, o$ is

$$\frac{\partial}{\partial t}(\phi \rho_\alpha S_\alpha) - \nabla \cdot (\rho_\alpha \lambda_\alpha \underline{k}(\nabla p_\alpha + \gamma_\alpha \nabla z)) = \rho_\alpha q_\alpha \quad (4.2.1)$$

where λ_α is the phase mobility expressed as $\lambda_\alpha = \frac{k_{r\alpha}}{\mu_\alpha}$ (1/Pa · s).

The Darcy velocity can be defined by

$$\underline{u}_\alpha = -\lambda_\alpha \underline{k}(\nabla p_\alpha - \gamma \nabla z) \quad (4.2.2)$$

The auxiliary relations that apply to complete the two-phase flow formulation are the continuity of fluid saturation:

$$S_w + S_o = 1, \quad (4.2.3)$$

and the capillary pressure defined as

$$p_c = p_o - p_w. \quad (4.2.4)$$

The assumptions taken into consideration are the following:

- The temperature is constant in the system.
- There are two phases: water (w) and oil (o).
- There are two components: water (W), only in the water phase, and oil (O), only in the oil phase.
- The rock (porous matrix) and the fluids are incompressible.
- The solid matrix is not poroelastic; meaning that the available pore space (porosity) is constant.

- The fluid properties (e.g. density, dynamic viscosity) of the two phases are considered constant and pressure independent.
- Immiscible displacement of the two fluids takes place.

This set of equations, PDEs and auxiliary equations, allows for equation manipulation such that the main differences between the formulations are the dependent variables that are solved for. In this study the fractional flow formulation is applied, which is a so-called saturation based formulation.

4.2.2 Fractional Flow Formulation

This approach employs the saturation of the one of the phases and a global/total pressure as the dependent variables. The fractional flow approach treats the multiphase flow problem as a total fluid flow of a single mixed fluid, and then describes the individual phases as fractions of the total flow. The fractional flow of each phase α is expressed as $f_\alpha = \lambda_\alpha/\lambda$ and λ is the total mobility equal to $\lambda_w + \lambda_o$. (Bjørnarå and Aker, 2008)

This approach leads to two equations; the global pressure equation and the saturation equation. The equations can be found by adding the mass balances and do some numerical manipulation; the pressure equation:

$$\nabla \cdot \underline{\mathbf{u}} = q_w + q_o \quad (4.2.5)$$

and by subtracting the mass balances and do some numerical manipulation; saturation equation:

$$\phi \frac{\partial(S_a)}{\partial t} + \nabla \cdot \underline{\mathbf{u}}_a = q_a \quad (4.2.6)$$

The phase velocities are given by these expressions:

$$\underline{\mathbf{u}}_w = f_w \underline{\mathbf{u}} + \lambda_o f_w \underline{\mathbf{k}} (\nabla p_c + (\rho_w - \rho_o) \underline{\mathbf{g}}) \quad (4.2.7)$$

$$\underline{\mathbf{u}}_o = f_o \underline{\mathbf{u}} + \lambda_w f_o \underline{\mathbf{k}} (\nabla p_c + (\rho_w + \rho_o) \underline{\mathbf{g}}) \quad (4.2.8)$$

while the total velocity is given by

$$\underline{\mathbf{u}} = -\underline{\mathbf{k}} (\lambda \nabla p - (\lambda_w \rho_w + \lambda_o \rho_o) \underline{\mathbf{g}}) \quad (4.2.9)$$

In the current study, negligible capillary forces are assumed.

4.3 Model Implementation in COMSOL Multiphysics

The performance of the two-phase incompressible fluid flow is simulated in a three dimensional horizontal orthogonal reservoir of size 2500'x2500'x50', as shown in Fig. 4.2. The depth of the reservoir top is at 8000 ft and it consists of one layer. Two cylindrical wells of radius 10 ft and height 50 ft are introduced; an injection well and a production well. The injector is placed in one corner, from which 3500 stb/day of water are injected, and the producer is installed near the opposite corner (as shown by the red arrows). Both the wells are perforated.

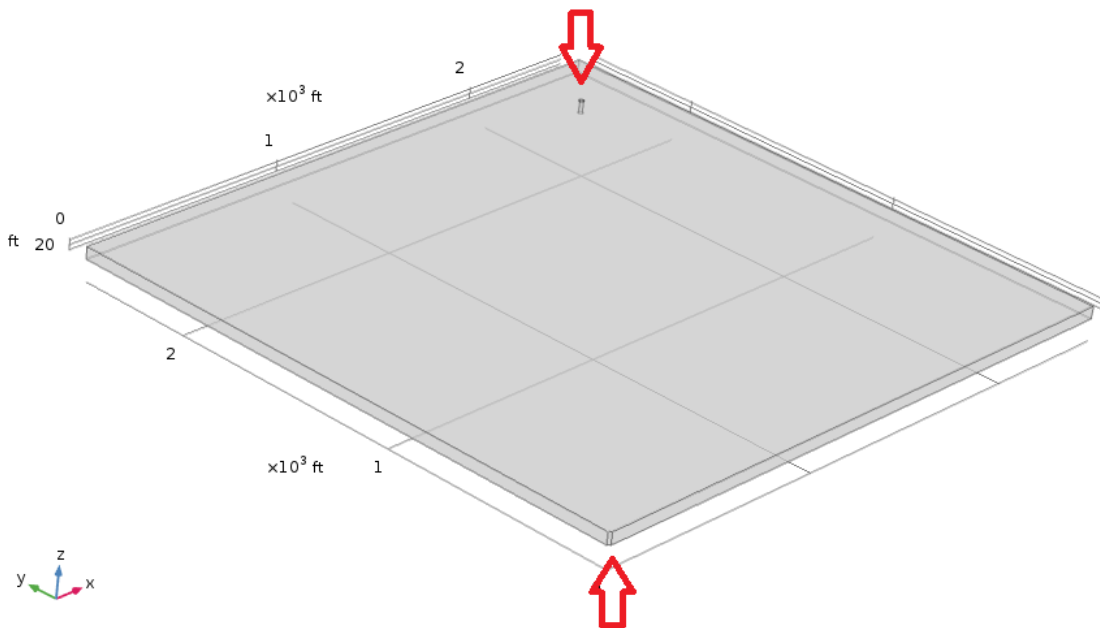


Figure 4.2: Reservoir geometry.

The absolute permeability in the three directions is shown in the following table. These values are inserted as parameters in the COMSOL software.

Permeability (mD)		
Horizontal		Vertical
X direction (k_x)	Y direction (k_y)	Z direction (k_z)
250	200	25

Table 4.1: Intrinsic permeability in x,y,z directions for the two-phase incompressible flow models.

The relative permeability of each phase is given as a function of the saturation of the water phase, as shown below. They are inserted into COMSOL as interpolation functions with a piecewise cubic relationship. The constant relationship is applied for the extrapolated values.

S_w	kr_w	kr_o
0.25	0.00	0.90
0.50	0.20	0.30
0.70	0.40	0.10
0.80	0.55	0.00

Table 4.2: Water and oil relative permeability for the two-phase incompressible flow models.

From the above data, the two irreducible phase saturations are extracted; the connate water saturation and the residual oil saturation. The connate water saturation is the one below which the water phase can not move, thus the water relative permeability is zero at that value. That is for water saturation equal to 0.25. The residual oil saturation is the one below which the oil relative permeability becomes zero, which is evaluated equal to 0.20 from [Table 4.2](#) according to [Eq. \(4.2.3\)](#). The connate water saturation is inserted as input in the model so as to obtain the initial values of the two phases in the reservoir.

The parameters that are common in the two models are listed in the following table.

Parameters	Units	Values
Porosity, ϕ	-	0.2
Connate water saturation, S_{wc}	-	0.25
Water density, ρ_w	kg/m ³	1000
Oil density, ρ_o	kg/m ³	800
Water dynamic viscosity, μ_w	cP	3.92
Oil dynamic viscosity, μ_o	cP	1
Inflow velocity, u_{in}	m/s	$8.83 \cdot 10^{-5}$
Numerical diffusivity, c	m ² /s	10^{-4}

Table 4.3: Parameters for the two-phase incompressible flow models.

Also, the phase mobility and the phase fractional flow are inserted as variables in both models.

Variables	Units	Expression
Saturation of non-wetting phase, S_o	-	$1 - S_w$
Water phase mobility, λ_w	1/(Pa·s)	$\frac{k_{rw}}{\mu_w}$
Oil phase mobility, λ_o	1/(Pa·s)	$\frac{k_{ro}}{\mu_o}$
Total mobility, λ	1/(Pa·s)	$\lambda_w + \lambda_o$
Water phase fractional flow, f_w	-	$\frac{\lambda_w}{\lambda}$
Oil phase fractional flow, f_o	-	$\frac{\lambda_o}{\lambda}$

Table 4.4: Variables for the two-phase incompressible flow models.

The above parameters and variable are the same for the models with and without the gravity. The difference is detected in the velocity components, which are input variables of the problem.

4.3.1 Model including Gravity

Firstly, the case when the gravity is taken into account is studied. The total and the phase velocity components are expressed as shown in the next table. Here the vector g points in the same direction as the unit vector of the z-axis.

Variables	Units	Expression
Total velocity, x component, u_x	m/s	$-k_x \lambda \frac{\partial p}{\partial x}$
Total velocity, y component, u_y	m/s	$-k_y \lambda \frac{\partial p}{\partial y}$
Total velocity, z component, u_z	m/s	$-k_z (\lambda \frac{\partial p}{\partial z} - (\lambda_w \rho_w + \lambda_o \rho_o) g)$
Water phase velocity, x component, u_{wx}	m/s	$f_w u_x$
Water phase velocity, y component, u_{wy}	m/s	$f_w u_y$
Water phase velocity, z component, u_{wz}	m/s	$f_w u_z + \lambda_o f_w k_z (\rho_w - \rho_o) g$
Oil phase velocity, x component, u_{ox}	m/s	$f_o u_x$
Oil phase velocity, y component, u_{oy}	m/s	$f_o u_y$
Oil phase velocity, z component, u_{oz}	m/s	$f_o u_z + \lambda_w f_o k_z (\rho_w + \rho_o) g$

Table 4.5: Velocity components for the model including gravity.

Also, the initial value of pressure and the bottomhole pressure at the production well are inserted as variables in the COMSOL model builder.

Variables	Units	Expression
Initial pressure, p_{in}	Pa	$10^5 + \rho_w g (2453.64[m] - z)$
BHP at producer, p_{out}	Pa	$10^5 + (S_{wc} \rho_w + (1 - S_{wc}) \rho_o) g (2453.64[m] - z)$

Table 4.6: Pressure for the model including gravity.

General Form PDE

The COMSOL multiphysics PDE mode for time dependent analysis in the general form is used for Eq. (4.2.5) with p as the dependent variable. The components of the conservative flux vector are the components of the total velocity, as expressed in Table 4.5. There is no source term.

Coefficient Form PDE

The PDE mode for time dependent analysis in the coefficient form is used for the Eq. (4.2.6) with S_w as the dependent variable. The conservative flux source is described by the components of the phase velocity (u_{wx} , u_{wy} , u_{wz}) as expressed in Table 4.5. There is no source term. The numerical diffusivity c is set isotropic and equal to the prescribed

value in Table 4.3, so as to stabilize the numerical solution.

Initial Conditions

$$p(t_0) = p_{in}, \frac{\partial p}{\partial t} = 0$$

$$S_w(t_0) = S_{wc}, \frac{\partial S_w}{\partial t} = 0$$

Boundary Conditions

Inlet conditions (constant rate)

$$-\underline{n} \cdot \underline{u} = u_{in}$$

$$S_w = 1$$

Outlet conditions (constant pressure)

$$p = p_{out}$$

$$-\underline{n} \cdot (-c\nabla S_w + \underline{u}_w) = -\underline{u}_w$$

Top, bottom and side walls (no flux)

$$-\underline{n} \cdot \underline{u} = 0$$

$$-\underline{n} \cdot (-c\nabla S_w + \underline{u}_w) = 0$$

Mesh and Solver

A free tetrahedral mesh with maximum element size 87.5 ft is applied. A scale geometry of 5 is used in the z direction, where gravity prevails.

The segregated time-dependent solver with free time stepping is used. At the first segregated step the dependent variable p is computed and following is the dependent variable S_w at the second step.

The PDEs with the specified initial and boundary conditions are solved in the above computational domain for a range of (0,1,2400) days.

4.3.2 Model neglecting Gravity

The variables of the 3D reservoir model, as modified for negligible gravity, are listed in the following table.

Variables	(units)	Expression
Total velocity, x component, u_x	m/s	$-k_x \lambda \frac{\partial p}{\partial x}$
Total velocity, y component, u_y	m/s	$-k_y \lambda \frac{\partial p}{\partial y}$
Total velocity, z component, u_z	m/s	$-k_z \lambda \frac{\partial p}{\partial z}$
Water phase velocity, x component, u_{wx}	m/s	$f_w u_x$
Water phase velocity, y component, u_{wy}	m/s	$f_w u_y$
Water phase velocity, z component, u_{wz}	m/s	$f_w u_z$
Oil phase velocity, x component, u_{ox}	m/s	$f_o u_x$
Oil phase velocity, y component, u_{oy}	m/s	$f_o u_y$
Oil phase velocity, z component, u_{oz}	m/s	$f_o u_z$

Table 4.7: Velocity components for the model neglecting gravity.

Since no gravitational forces are considered in the current case, the initial pressure prevailing in the reservoir is set constant, and so is the bottomhole pressure at the production well.

Parameters	Units	Values
Initial pressure, p_{in}	Pa	20489150.2
BHP at producer, p_{out}	Pa	20489150.2

Table 4.8: Pressure for the model neglecting gravity.

General Form PDE

The COMSOL multiphysics PDE mode for time dependent analysis in the general form is used for Eq. (4.2.5) with p as the dependent variable. The components of the conservative flux vector are the components of the total velocity, as expressed in Table 4.7. There is no source term.

Coefficient Form PDE

The PDE mode for time dependent analysis in the coefficient form is used for the Eq. (4.2.6) with S_w as the dependent variable. The conservative flux source is described by the components of the phase velocity as expressed in Table 4.7. There is no source term. The numerical diffusivity c is set equal to the prescribed value in Table 4.3.

Initial Conditions

$$p(t_0) = p_{in}, \frac{\partial p}{\partial t} = 0$$
$$S_w(t_0) = S_{wc}, \frac{\partial S_w}{\partial t} = 0$$

Boundary Conditions

Inlet conditions (constant rate)

$$-\underline{n} \cdot \underline{u} = u_{in}$$
$$S_w = 1$$

Outlet conditions (constant pressure)

$$p = p_{out} = p_{in}$$
$$-\underline{n} \cdot (-c\nabla S_w + \underline{u}_w) = -\underline{u}_w$$

Top, bottom and side walls (no flux)

$$-\underline{n} \cdot \underline{u} = 0$$
$$-\underline{n} \cdot (-c\nabla S_w + \underline{u}_w) = 0$$

Mesh and Solver

A free tetrahedral mesh with maximum element size 87.5 ft is applied.

The segregated time-dependent solver with free time stepping is used.

The PDEs with the specified initial and boundary conditions are solved for a range of (0,1,2400) days.

4.4 Results and Discussion

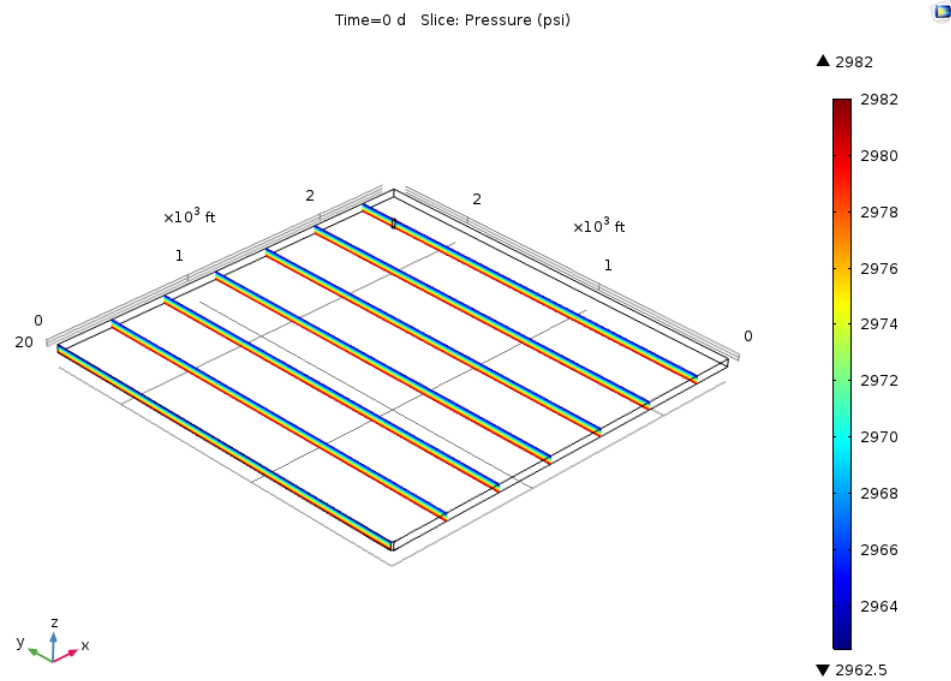
The pressure and the saturation of the wetting phase are calculated at each time step from the above numerical analysis as dependent variables. 3D figures demonstrating these quantities are presented for the two models implemented in COMSOL. The velocity field is also presented through 3D plots. The average field pressure, the bottomhole pressure of the two wells and the production rate of the fluids are also obtained as derived values of the solution of the problem.

The results from the COMSOL model that includes the gravity are presented in the next subsection and following are the results of the numerical model without the gravitational terms. Finally the two COMSOL models are compared with the results obtained by the ECLIPSE 100 simulator, as far as the oil production rate, the production well watercut and the cumulative productions are concerned.

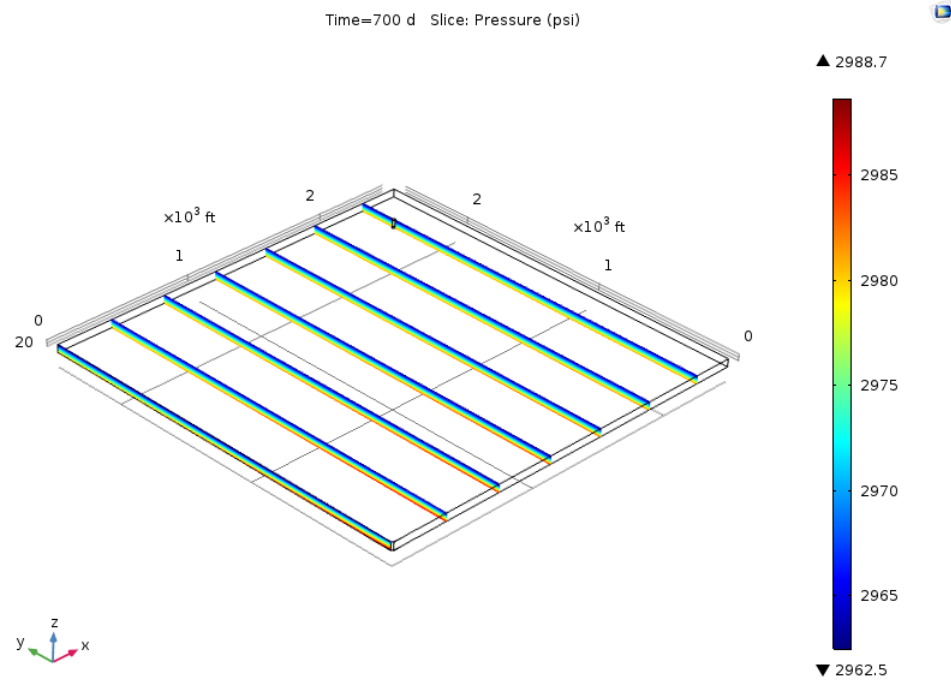
4.4.1 Model including Gravity

Firstly the dependent variable pressure is calculated from the numerical analysis. Following are three 3D figures illustrating the pressure regime at three different times. The figures are slice plots so as to make distinct the effect of gravity in the pressure distribution in the z axis.

4.4. RESULTS AND DISCUSSION



(a) $t = 0$ days



(b) $t = 700$ days

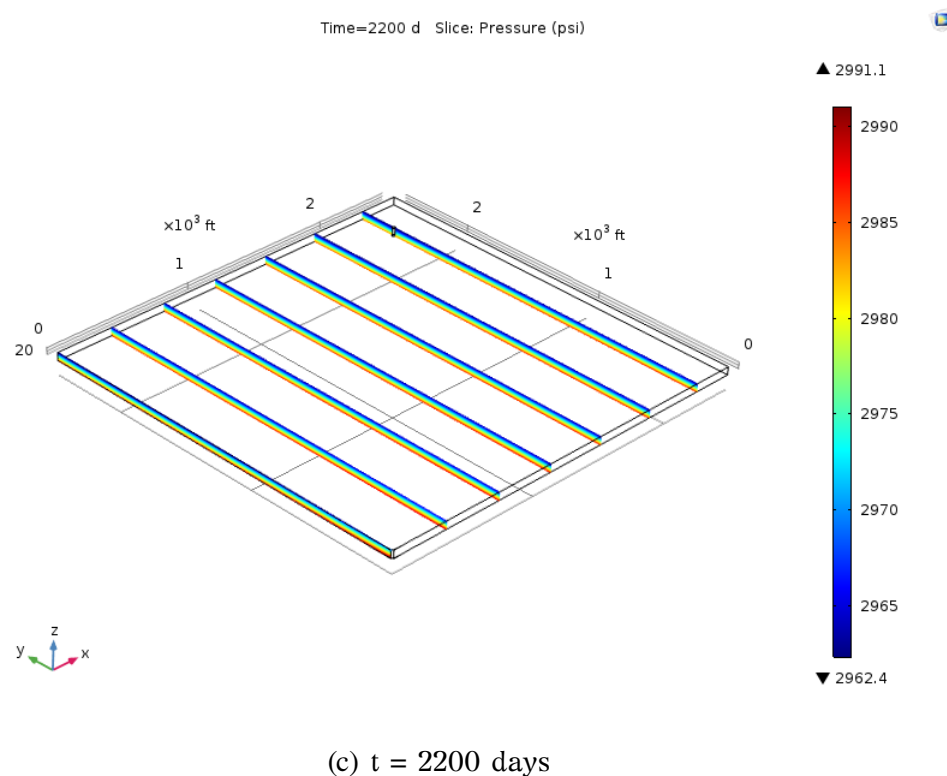


Figure 4.3: Pressure field; slice plots (Model including gravity).

Before the initiation of the secondary recovery process, the pressure regime in the reservoir is the one shown in Fig. 4.3a. The pressure is increasing with the depth, exhibiting the maximum value at the bottom of the reservoir, that of 2982 psi. No pressure variances exist in x and y directions. The injection of the water floods causes a pressure distribution in all three directions, as it can be visually verified by the rest plots of Fig. 4.3. Throughout the whole process the pressure regime does not change significantly. In general, the areas near the two wells exhibit bigger pressure values with time.

The botommhole pressure of each well as well as the average field pressure are evaluated with time and illustrated in the following graphs. While the shape of these pressure plots should be considered as an accurate representation of the actual pressure variances, the exact values however depend strongly on the size of the injection well, given the constant flow rate boundary condition imposed for these simulations.

4.4. RESULTS AND DISCUSSION

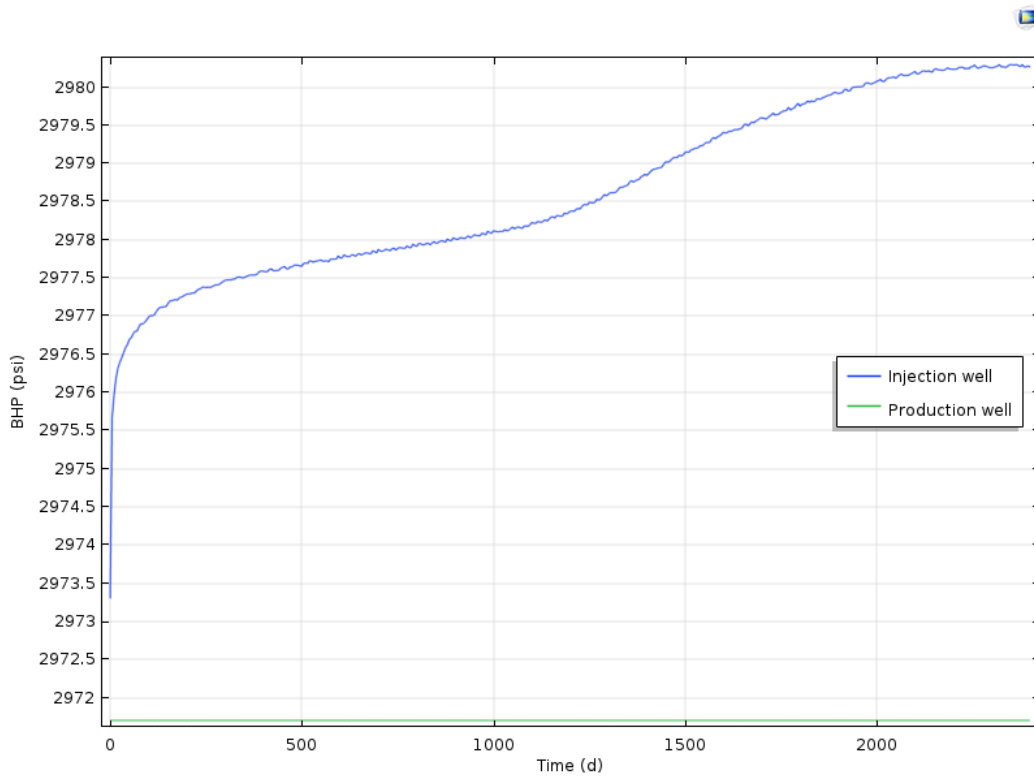


Figure 4.4: Bottomhole pressure of the two wells (Model including gravity).

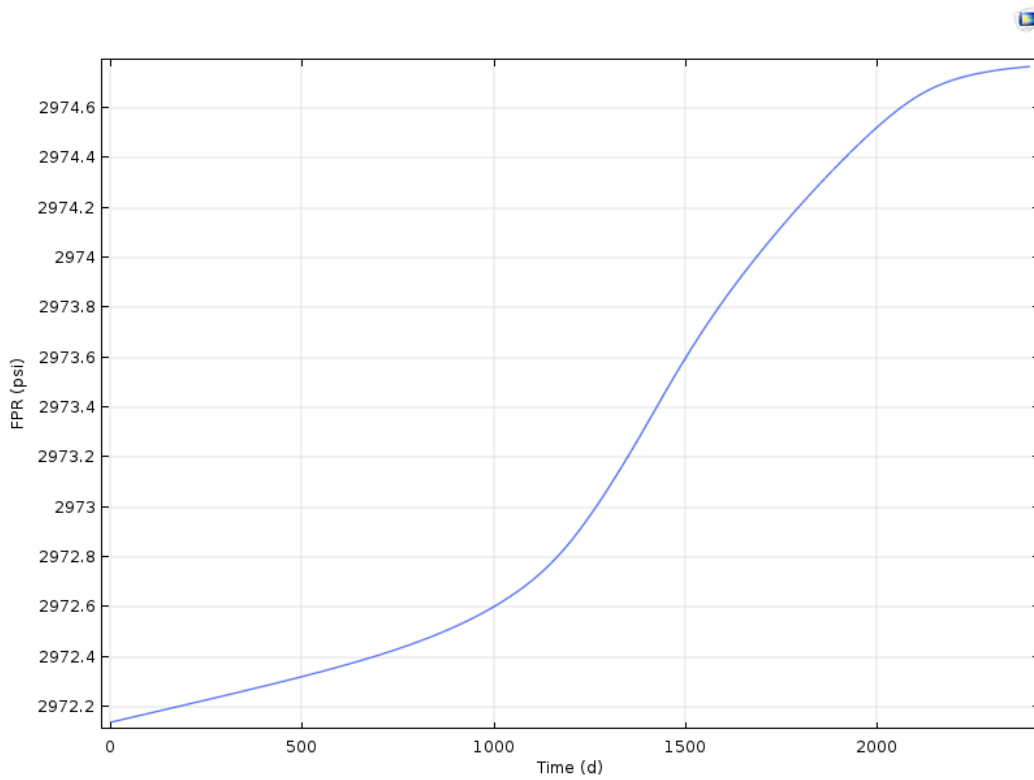


Figure 4.5: Average reservoir pressure (Model including gravity).

Throughout the injection process the BHP in the production well remains constant at 2971.7 psi, while the BHP of the injector exhibits an increasing rate. At the beginning of the waterflooding an abrupt increase is observed, due to the energy that enters the reservoir. The BHP keeps increasing but with a smoother rate during the whole procedure up to the maximum value of 2980.3 psi at the last days of the waterflooding. The average field pressure vs time profile presents a similar behavior but with a small difference. The increasing rate is smoother during the oil production and becomes more abrupt after the water phase reaches the producer. Throughout the secondary process, the average pressure stays at higher values than that of the producer, confirming that the model is physically correct; the flow is from areas with higher pressure towards the area with the smallest pressure. In general, the average reservoir pressure is maintained high till the end of the secondary recovery technique.

The velocity field is also computed from the solution of the time-dependent problem. It is represented through arrow volume plots in the following figures.

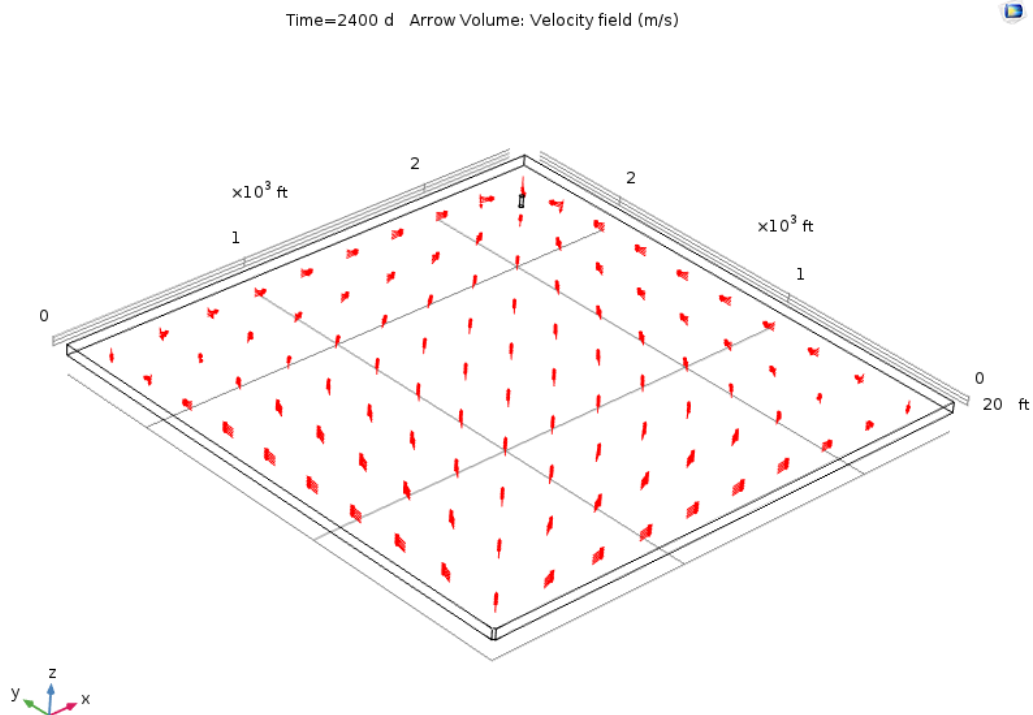


Figure 4.6: Velocity field at the 2400th day; arrow volume plot (Model including gravity).

4.4. RESULTS AND DISCUSSION

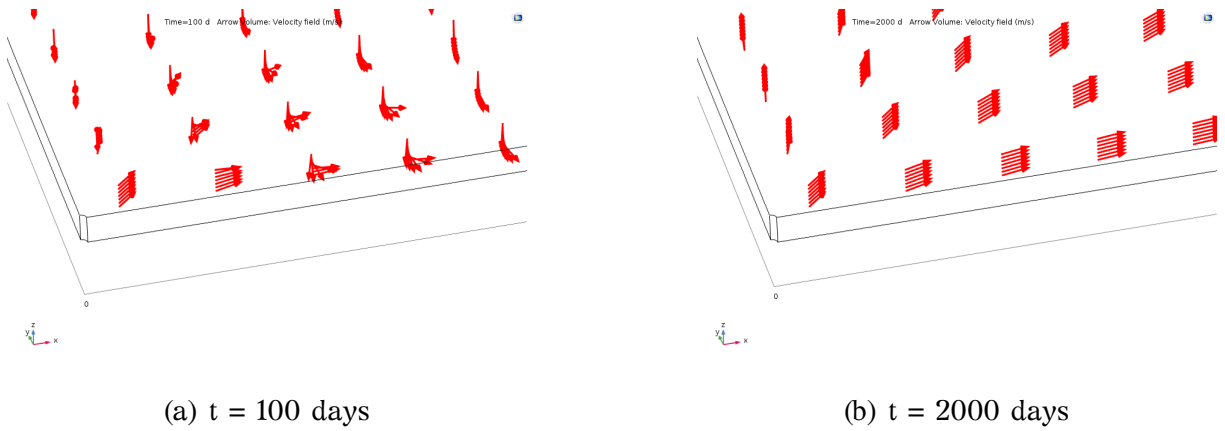


Figure 4.7: Velocity field; arrow volume plot. Zoom in injection well at two different times (Model including gravity).

The velocity field at the last day of the injection process is presented in the [Fig. 4.6](#). The head of the arrows show the direction of the velocity, that is towards the area where the production well is located. [Fig. 4.7](#) illustrates the velocity field in the area around the injection well with the use of normalized arrows volume plot. The two different days are selected in order to underline the change of the velocity field with the change of the wetting phase saturation and the effect of gravity. At the early stages of the injection process ([Fig. 4.7a](#)) the arrows point downwards due to gravitational forces, indicating the direction of the velocity of the wetting phase. Although equal quantity of water enters the reservoir via the perforations, the gravity causes the movement of the water downward to the bottom of the reservoir. The extent of this phenomenon depends strongly on the properties, e.g. viscosity and density, of both the wetting and non-wetting phases. After a big period of time the pores in the area around the injection well are filled with the wetting phase (and the residual oil) so the incoming water floods move towards the main direction and displace the aqueous phase, as the arrows point out in [Fig. 4.7b](#).

The evolution of the wetting phase saturation at different times after the initiation of the water injection is demonstrated through isosurfaces in the following set of figures.

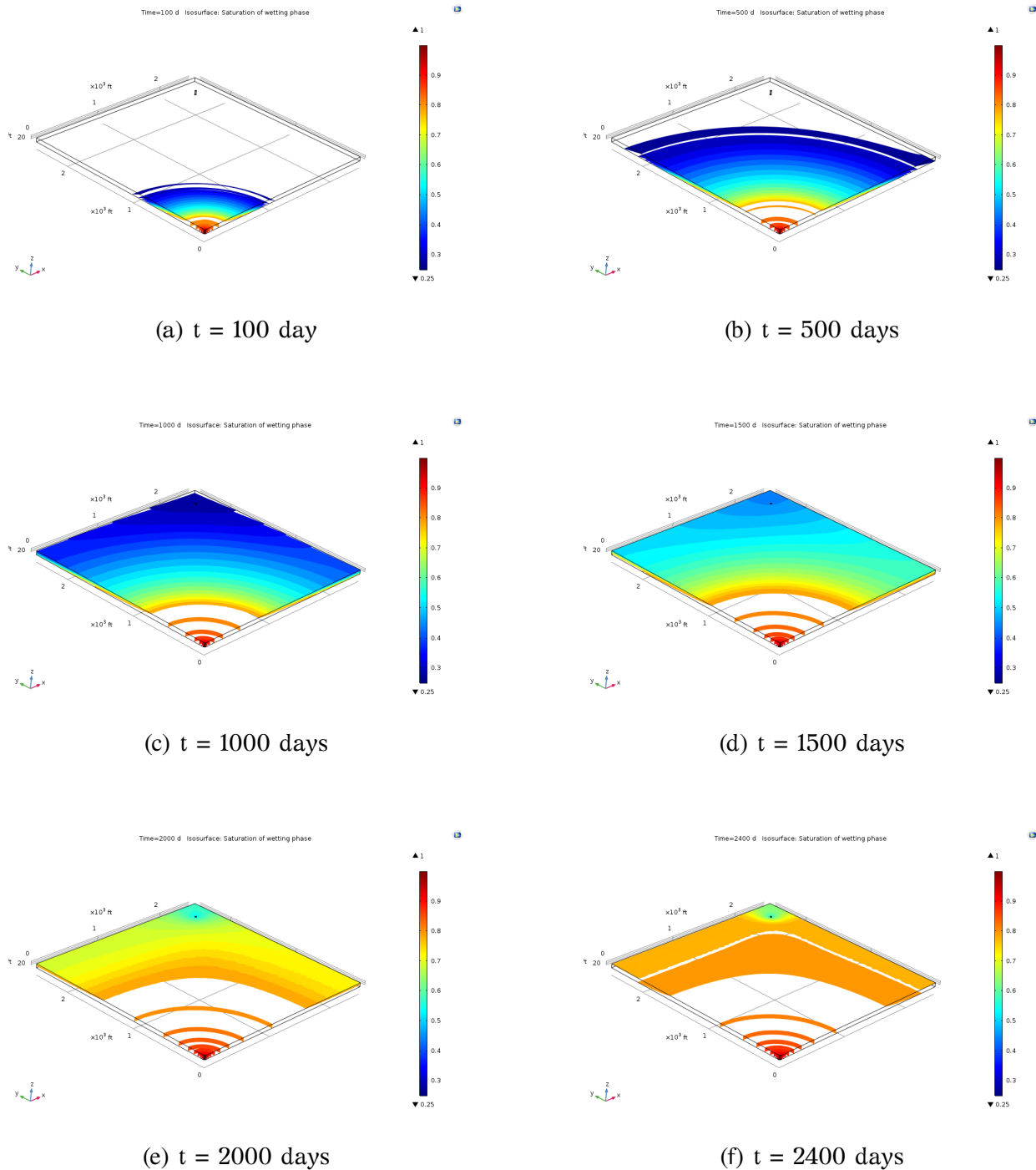


Figure 4.8: Isosurfaces for the saturation evolution of the wetting phase (Model including gravity).

The water is injected from the well in the corner with direction to the production well lying in the opposite corner. As water floods enter the reservoir, the saturation of the wetting phase gradually increases in the area near the injector leading to a larger swept

zone with time, which however is not uniform due to the buoyancy. The movement of the water saturation fronts in the vertical direction results in that bigger volumes of the reservoir oil in the areas near the bottom are contacted by the injected fluid comparing to the ones in the areas near the top of the reservoir. Hence, for the same period of time the wetting phase occupies bigger pore space at the areas near the reservoir bottom. This can be observed with a closer look at any of the plots Fig. 4.8a - Fig. 4.8d. As the water flooding proceeds more and more hydrocarbons are displaced in the swept areas, causing the hydrocarbons in the area around the production well to move towards it and be produced. The saturation of the wetting phase is constantly increasing in all over the reservoir and at the 2400th day, when the recovery process is terminated, most of the reservoir volume is filled with water. The average water saturation is around 0.8 and only a small area contains still some quantity of hydrocarbons. The efficient sweeping on both the horizontal and vertical directions can be visually verified by Fig. 4.8f.

The next figure illustrates the average phase saturation in the reservoir during the waterflooding.

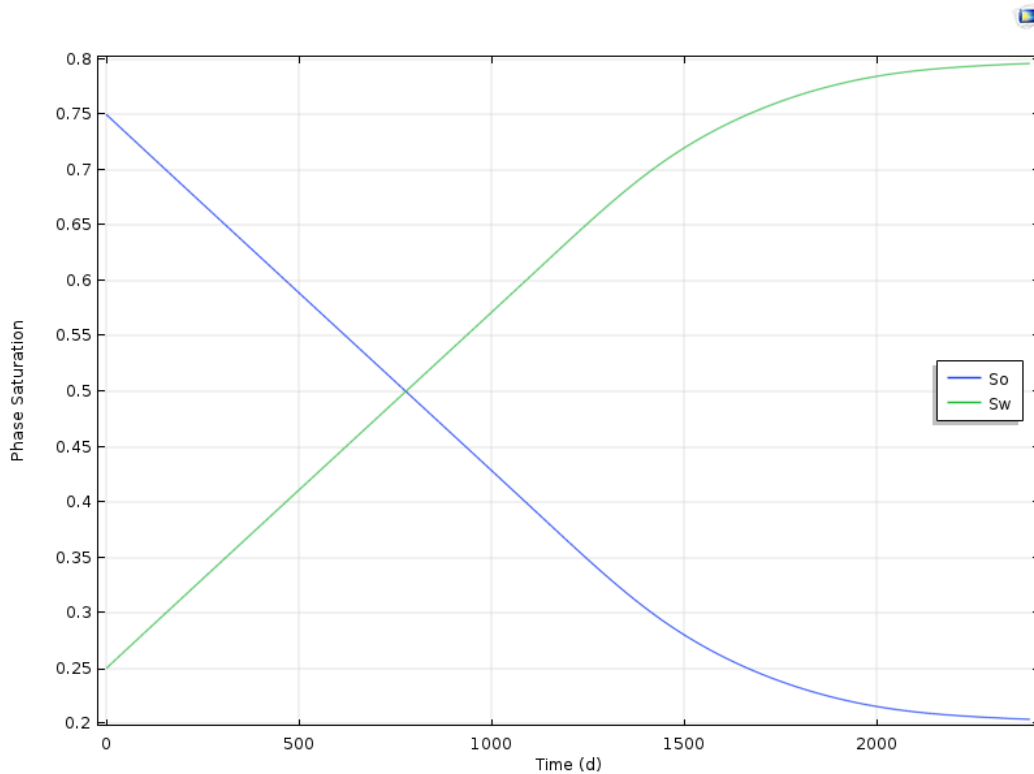


Figure 4.9: Average phase saturations (Model including gravity).

The initial saturation values of each phase are the ones inserted in the PDE interfaces.

During the waterflooding process the two phase saturations are inversely proportional as expected, since the injection of the wetting phase causes the non-wetting phase to be displaced and finally be produced. At the end of the simulation, the reservoir volume is filled with almost 80% water and 20% hydrocarbons, which agrees with the results obtained from the previous 3D plot.

Finally the daily amount of the produced liquids in stock tank barrels is calculated by applying a surface integration in the walls of the production well of each phase velocity.

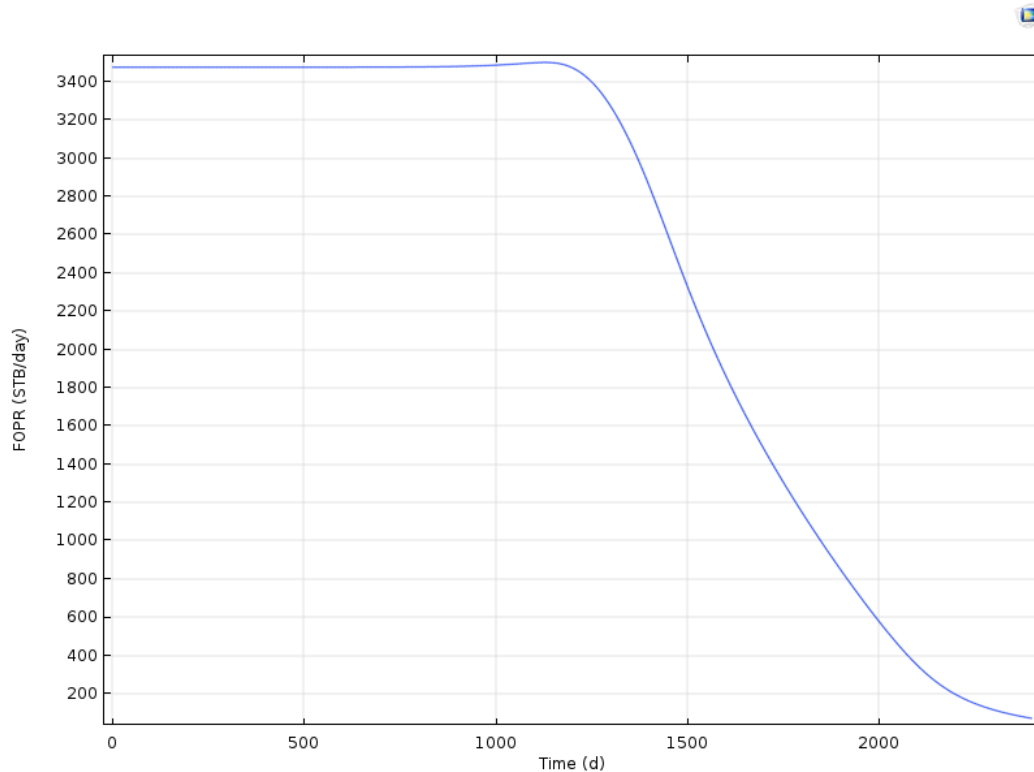


Figure 4.10: Oil production rate (Model including gravity).

Upon the beginning of the waterflooding, 3500 stb of hydrocarbons are produced daily. The production rate remains constant almost up to the 1200th day of the injection and it is followed by a smooth decrease till the end of the simulation. The observed change in the oil production rate is indicative of the water breakthrough. At the end of the simulation study, almost 100 stb/day of oil are produced.

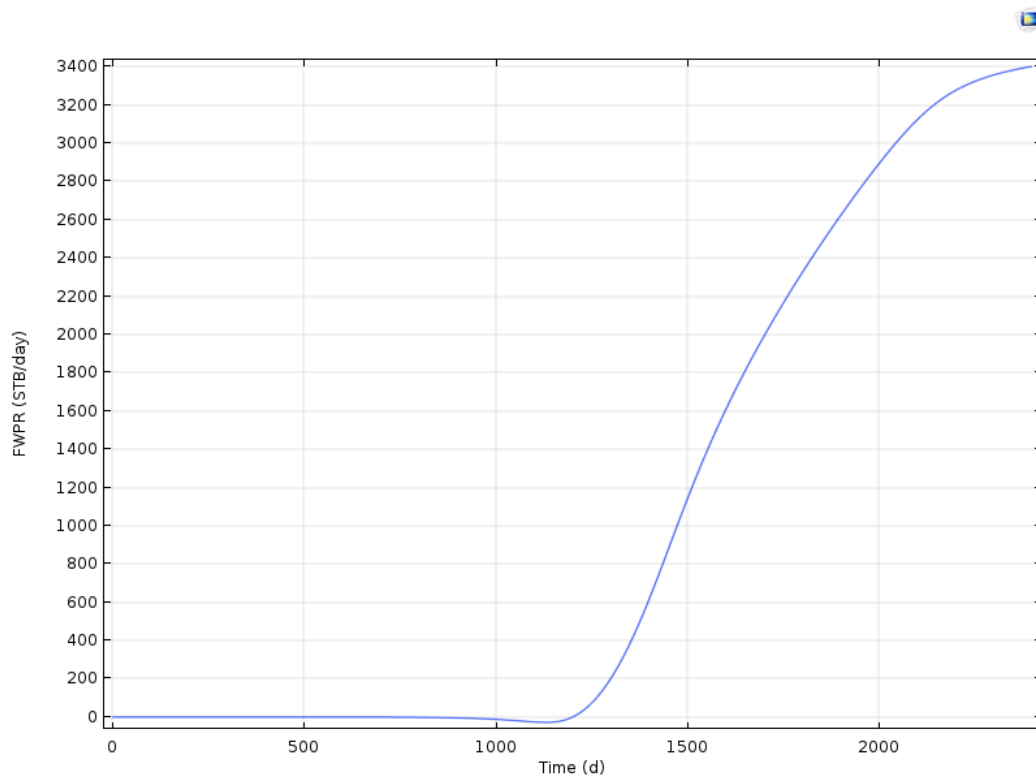
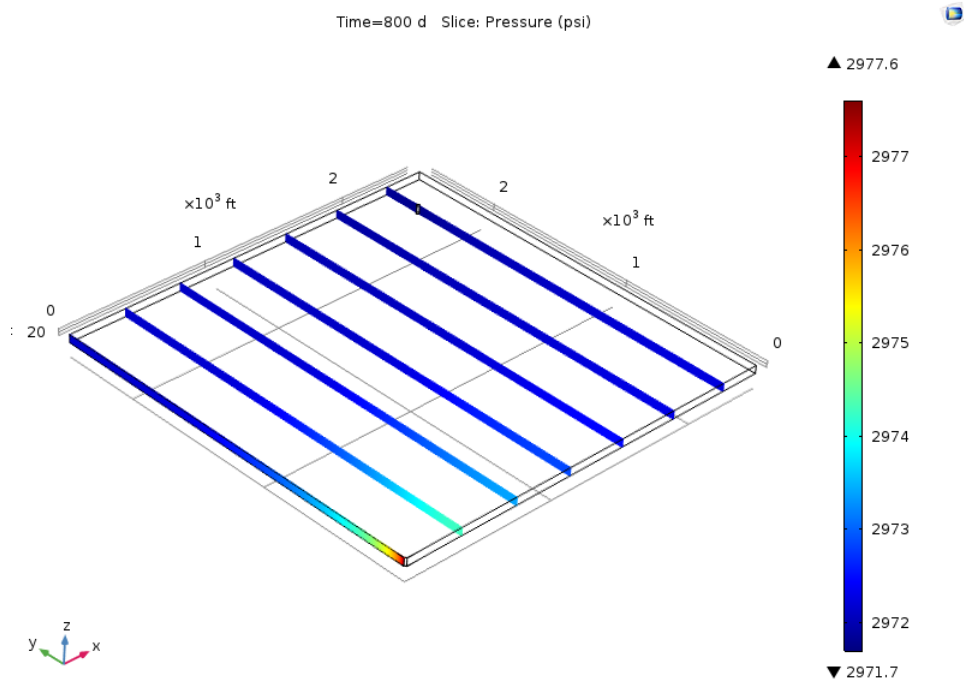


Figure 4.11: Water production rate (Model including gravity).

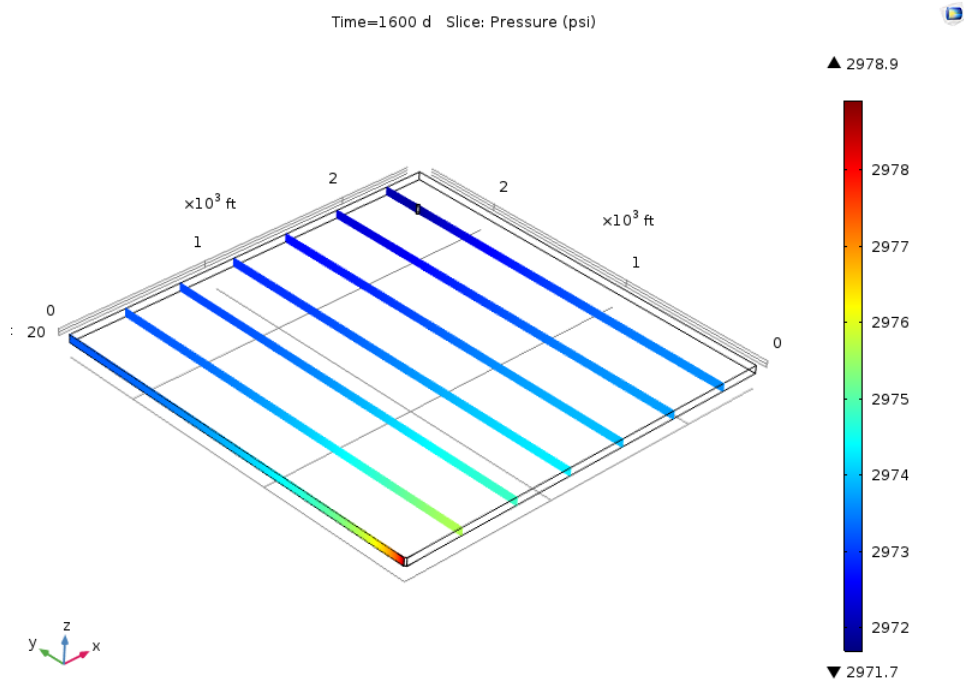
The water breakthrough takes place around the 1200th day, when the water starts being produced, as was also indicated by Fig. 4.10. From that day and on the production rate of the wetting phase follows an increasing rate till the end of the simulation study. At the end of the production almost 3400 stb/day of water are produced.

4.4.2 Model neglecting Gravity

The pressure regime at different times throughout the secondary recovery is demonstrated in the following 3D plots.

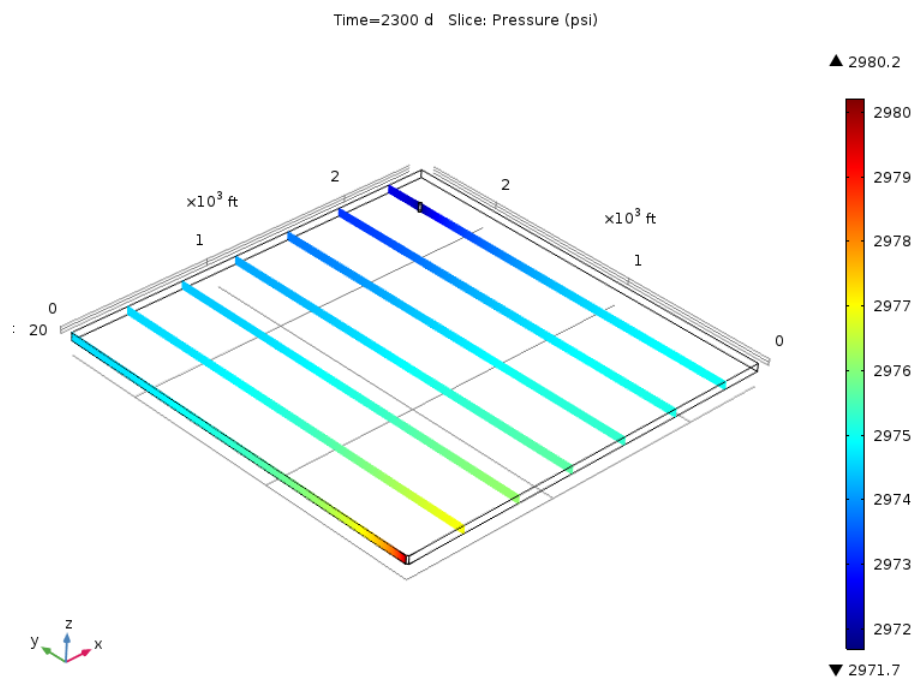


(a) $t = 800$ days



(b) $t = 1600$ days

4.4. RESULTS AND DISCUSSION



(c) $t = 2300$ days

Figure 4.12: Pressure field; slice plots (Model neglecting gravity).

The initial pressure prevailing in the whole reservoir is 2971.7 psi (20.49 MPa). The controlling mechanism of the production in the current model is the constant BHP, which has been attributed with the value of 2971.7 psi as a boundary condition. The incoming water floods cause a pressure increase in the area around the injection well, which keeps increasing as the injection process proceeds. As the water propagates toward the production well, the field pressure exhibits gradually bigger values. The pressure regime in the vertical direction is uniform in the current case, as expected. The above pressure regime is clearly different, when comparing it with Fig. 4.3 which is obtained from the model with the gravity.

The bottomhole pressure of each well and the average field pressure during the secondary recovery process are derived and presented in the following graphs.

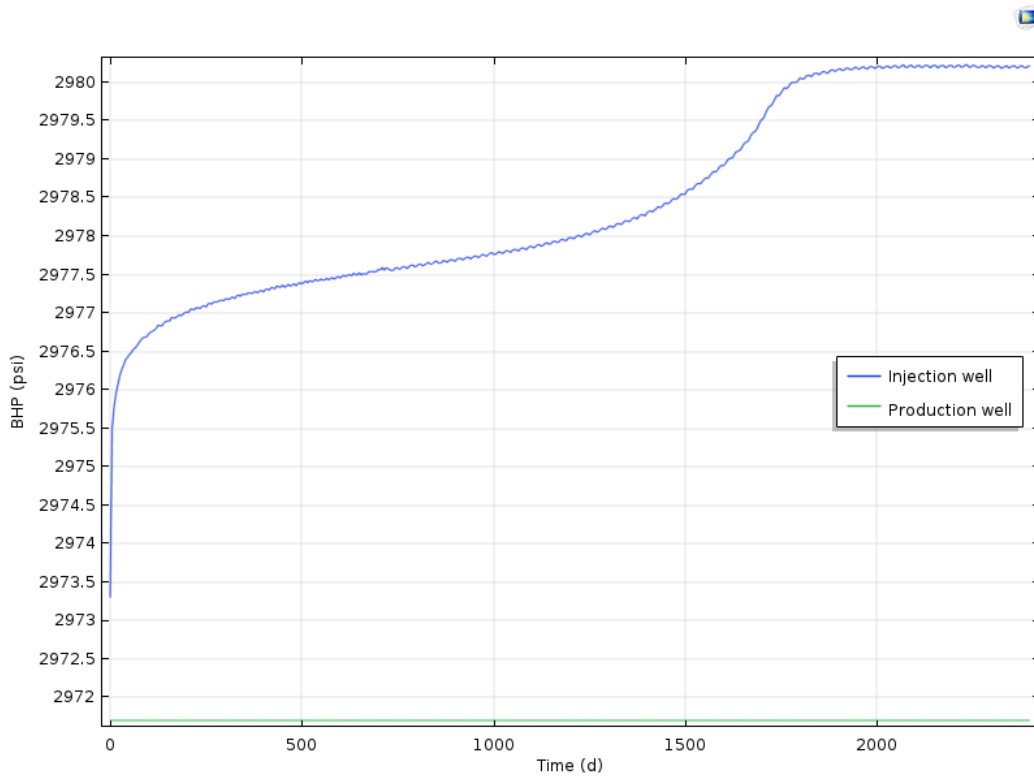


Figure 4.13: Bottomhole pressure of the two wells (Model neglecting gravity).

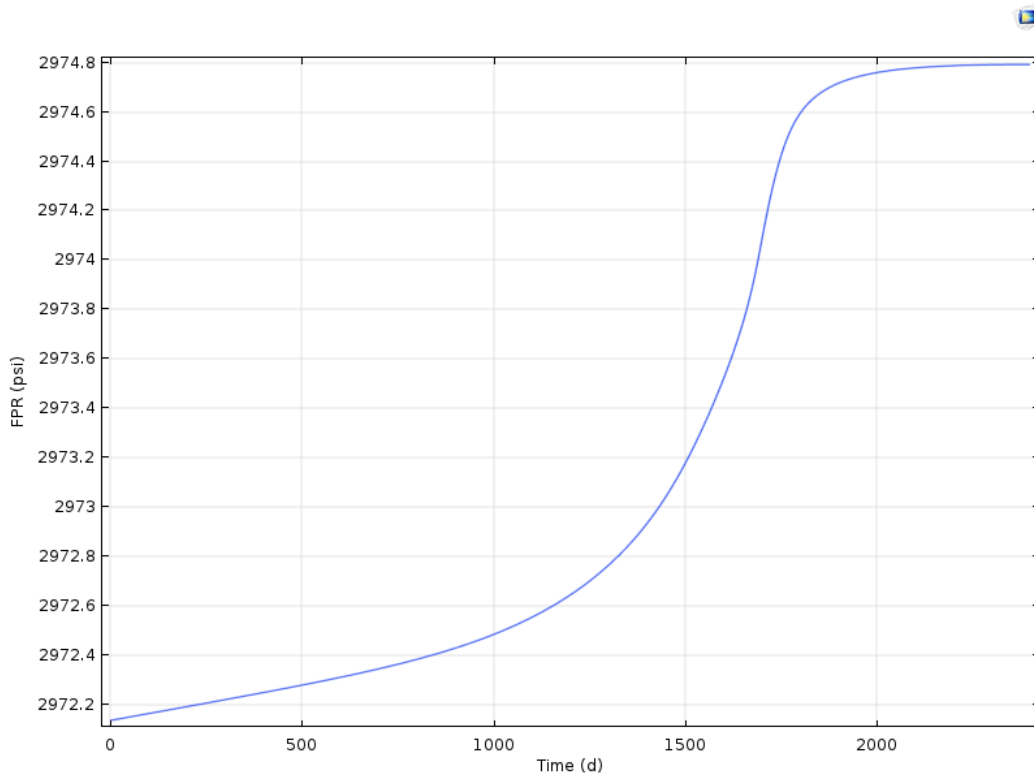


Figure 4.14: Average reservoir pressure (Model neglecting gravity).

4.4. RESULTS AND DISCUSSION

Both the BHP of the injector and the average field pressure follow a rising rate, almost till the end of the water flooding process. The BHP of the injector stabilizes at the last 400 days of the process, which indicates that the steady state is achieved since the produced fluid consists mainly from water. In the case of the model with the gravity, the BHP at producer followed an increasing rate till the last day of the simulation. The BHP of the producer is steady at 2971.7 psi.

The velocity field is represented through the arrow volume plots in the following figures.

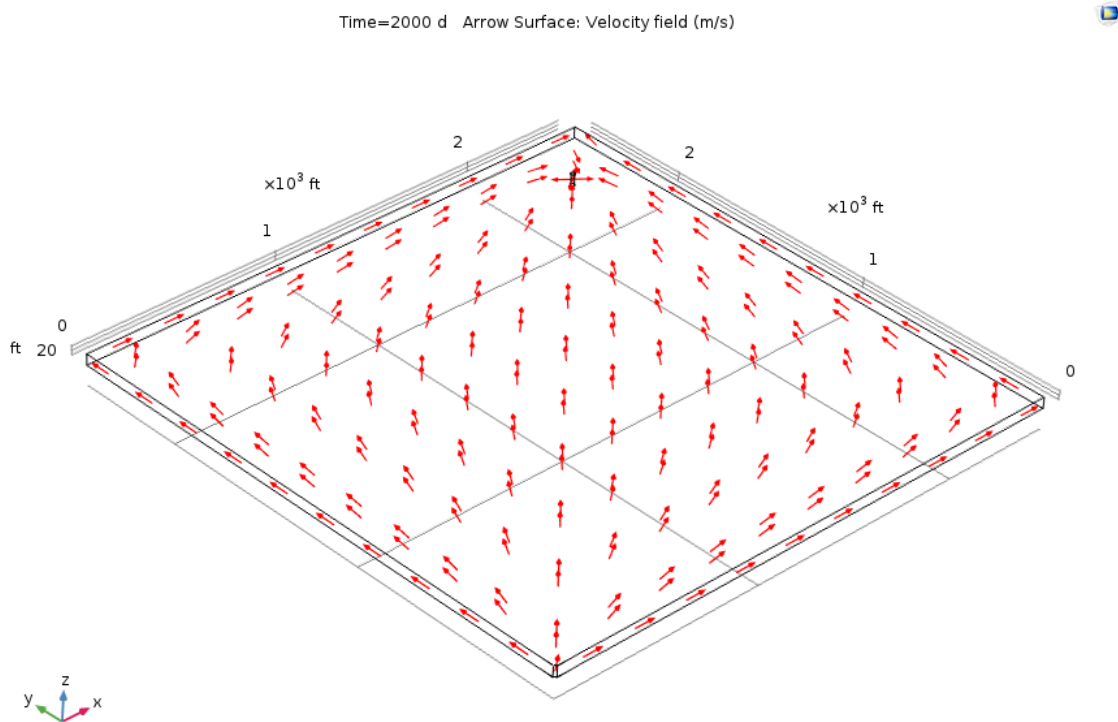
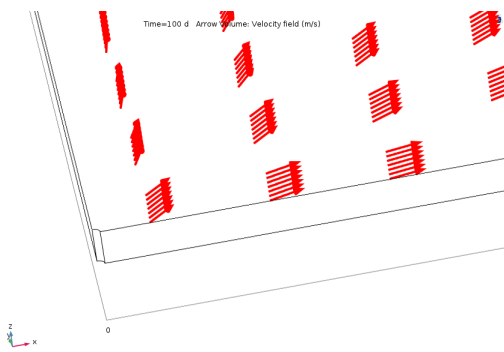
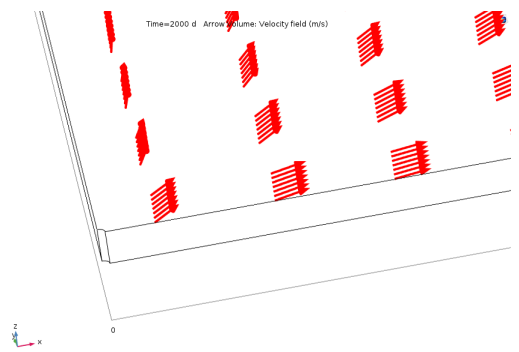


Figure 4.15: Velocity field; arrow volume plot (Model neglecting gravity).

The flow is from the injection well to the production well, as the surface arrows indicate. Since the gravitational terms are omitted it is expected that the direction of all volume arrows is uniform at all times and independent from the saturation of the wetting phase. This is verified by the next figures, that show the velocity field in the area around the injection well at two different times.



(a) $t = 100$ days

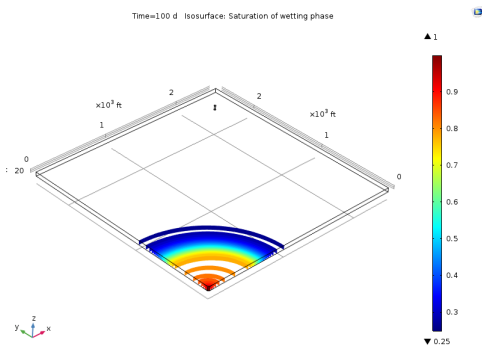


(b) $t = 2000$ days

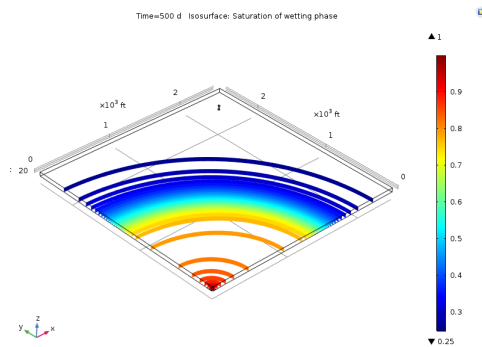
Figure 4.16: Velocity field; arrow volume plot. Zoom in injection well at two different times (Model neglecting gravity).

As expected, the absence of gravity creates no distribution in the direction of the velocity of the wetting phase. All arrows at all time selections point out to the same direction, namely the flow is parallel to the horizontal direction. The absence of gravity, hence, has a different effect on the velocity dynamics compared to its presence.

This is also visually verified by the next set of 3D plots which demonstrate the evolution of the saturation of the wetting phase at different times.



(a) $t = 100$ day



(b) $t = 500$ days

4.4. RESULTS AND DISCUSSION

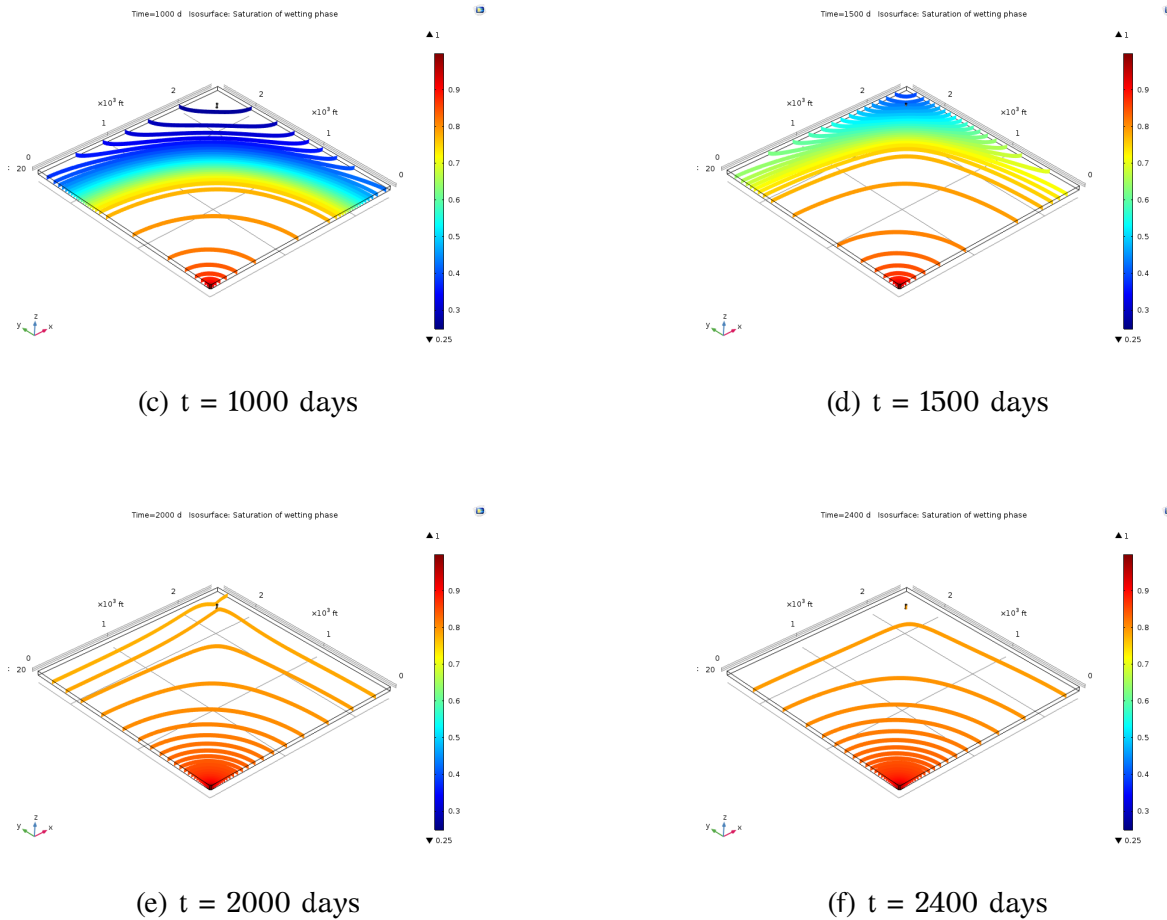


Figure 4.17: Isosurfaces for the saturation evolution of the wetting phase (Model neglecting gravity).

All water saturation fronts propagate toward the horizontal direction and create uniform swept areas in the vertical direction. At the 1500th day of the displacement process the water floods have reached the production well. The largest area of the reservoir has efficiently been swept by the injected fluid and after a time period of 500 days almost all the mobile hydrocarbons have been recovered, as shown in Fig. 4.17e. The saturation profile of the wetting phase remains almost the same till the end of the secondary recovery process.

Differences are detected when comparing the above set of plots with the ones from Fig. 4.8. Apart from the different way that the field is swept by the injected fluid in the vertical direction and has already been discussed, the amount of hydrocarbons that have remained topically in the reservoir volume at the end of the process is also different.

According to the current model, no mobile hydrocarbons have remained at the end of the process while the model with the gravity predicts that for the same injection duration not all the mobile oil has been displaced.

The average phase saturations are then presented.

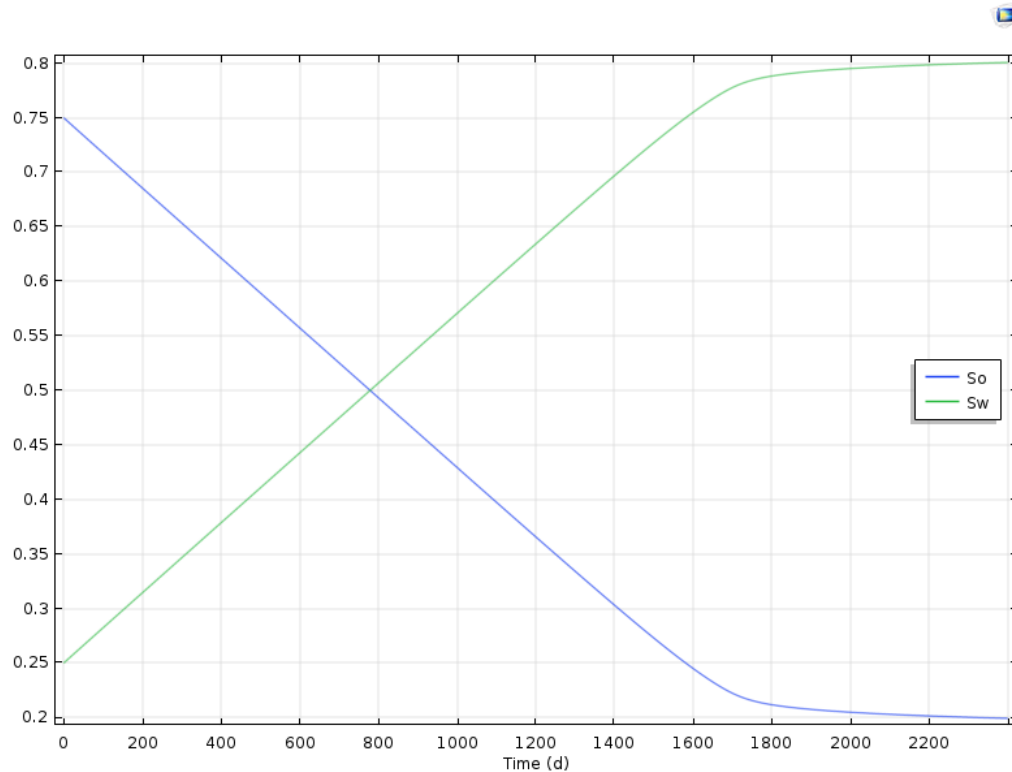


Figure 4.18: Average phase saturations (Model neglecting gravity).

The average saturation of the oil phase decreases strongly till the 1800th day and then approaches smoothly the minimum value of 0.2 till the last days of the recovery. The saturation of the aqueous phase has the exact inverse behavior, which confirms that the model is physically correct. The average endpoint saturations are close to the ones obtained from the first COMSOL model.

In the following graphs the production rate of the two fluids in stock tank barrels/day are presented.

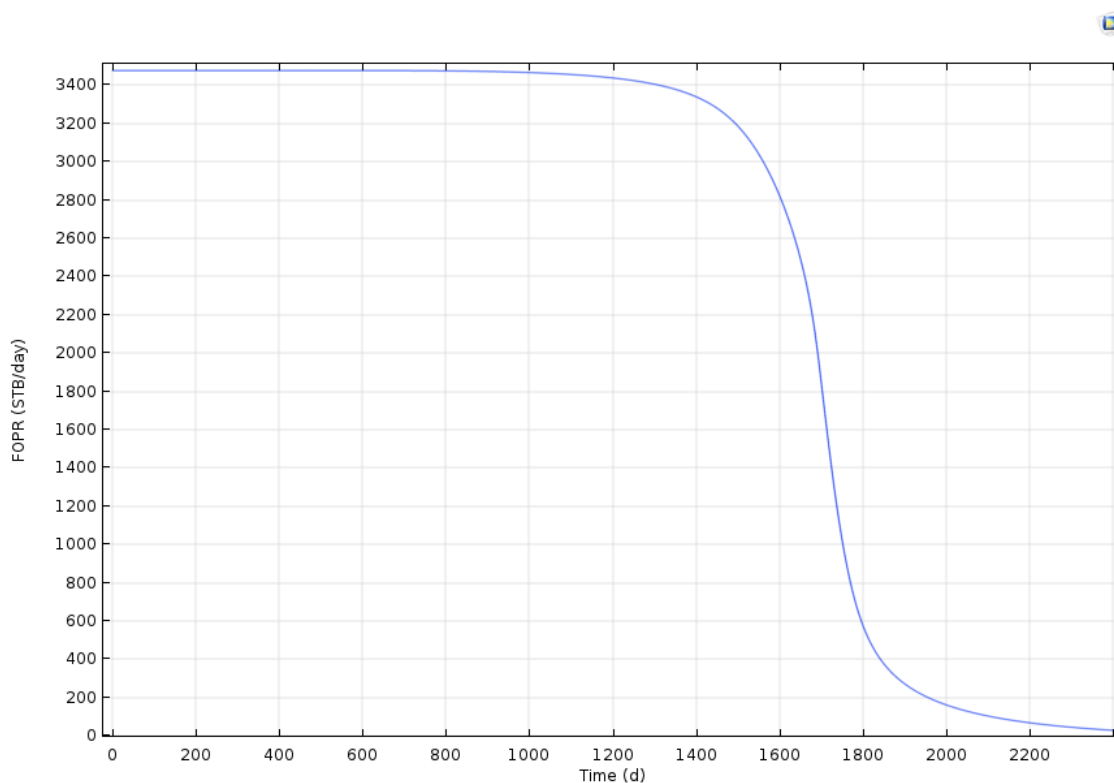


Figure 4.19: Oil production rate (Model neglecting gravity).

The hydrocarbons are produced with a constant rate of 3500 stb/day for the first 1000 days, when the water breakthrough occurs. A smooth decrease of the rate is observed for a period of almost 500 days, followed by an abrupt decrease till the 2000th day of the oil recovery process. The production rate is decaying till the last day of the simulation study, when all the amount of mobile hydrocarbons has been produced.

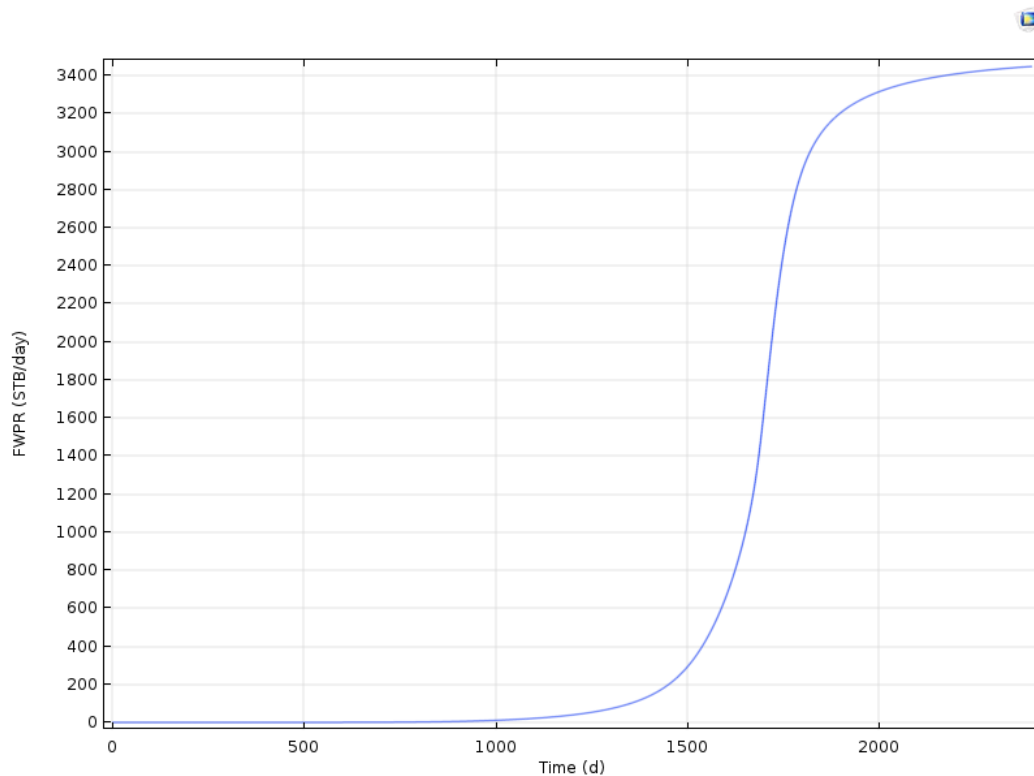


Figure 4.20: Water production rate (Model neglecting gravity).

Referring to Fig. 4.20, the water production rate is zero till the 1000th day. The first water floods that reach the producer are produced slowly with an increasing, however, rate. As more water arrives in the drainage area of the producer the mobility of the wetting phase becomes bigger and the water is being produced with a higher rate, as indicated by the graph. The production rate keeps increasing till the end of the simulation, when the maximum water production rate of almost 3500 stb/day is reached.

4.4.3 Comparison with ECLIPSE 100

The difference of the two models in the estimation of the fluids production rates became obvious from the results of the above simulation studies. The physical model was also numerically solved in the ECLIPSE 100 simulator, which is considered as a trustworthy tool on the simulation of reservoir problems and it is used widely in the oil industry. The hydrocarbons production rate, the watercut at the production well and the cumulative phase productions are compared so as to evaluate the results of the two different models implemented in COMSOL Multiphysics.

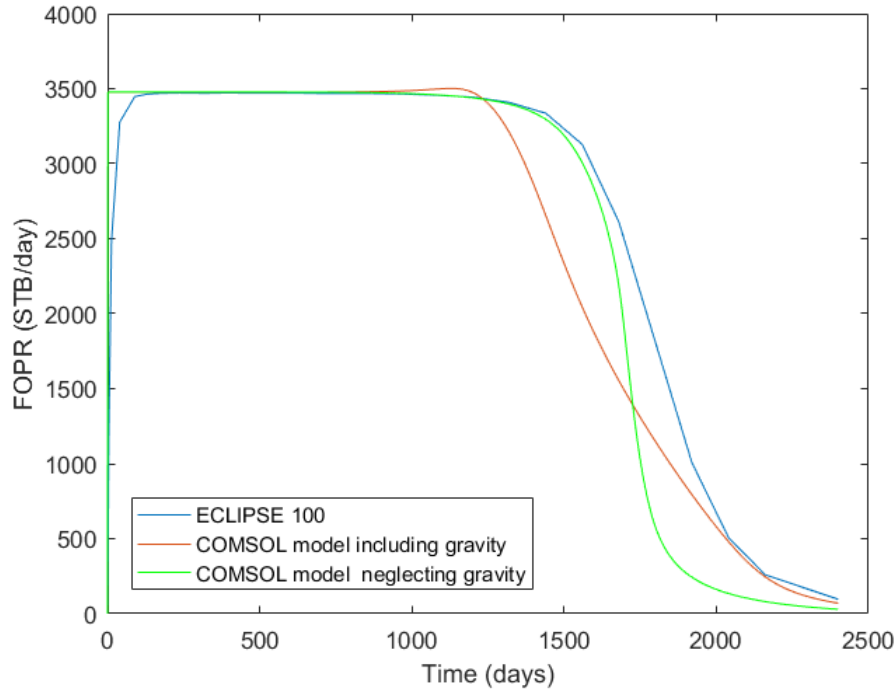


Figure 4.21: Comparison of oil production rate with the two COMSOL models and ECLIPSE 100.

The production rate of the hydrocarbons for the three cases is illustrated in [Fig. 4.21](#). Both the COMSOL and the ECLIPSE 100 simulators predict a maximum production rate of 3500 stb/day. The model in COMSOL that takes into account the gravity overpredicts by almost 200 days the duration of the maximum production rate compared to the other two models, and consequently the time of the water breakthrough. The model in COMSOL that neglects the gravity estimates the same production rate with ECLIPSE till the 1400th day. Distinct differences are then obtained when the oil production follows a decaying rate. Both COMSOL models underestimate the rate compared to ECLIPSE. But the more abrupt change of rate from the maximum to the lower that is estimated by the model with the absence of gravity points out that it encounters less numerical instabilities than the one with the gravity, as this sigmoidal profile usually holds true in simulation studies of waterflooding.

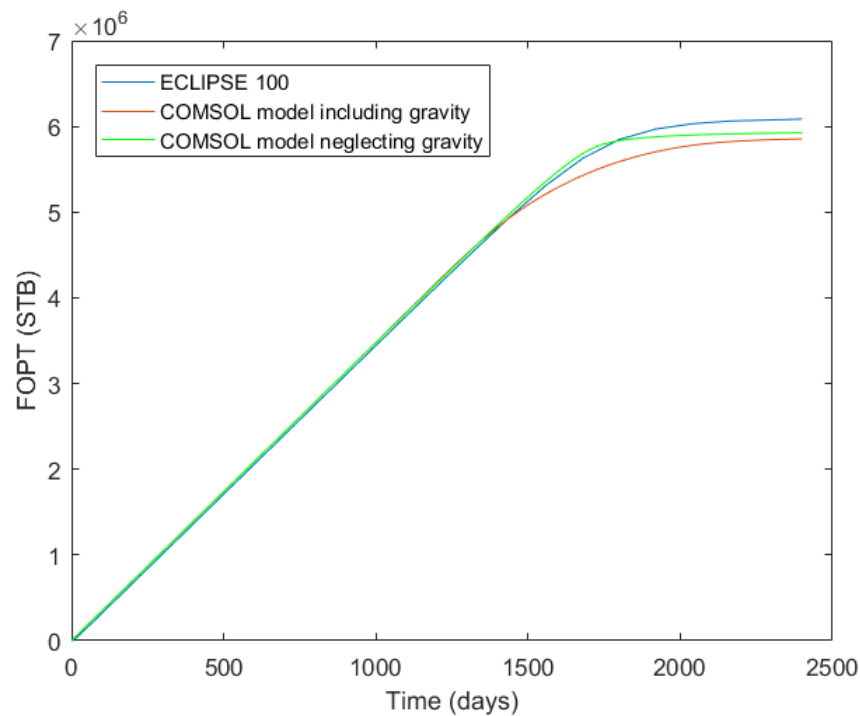


Figure 4.22: Comparison of cumulative oil production with the two COMSOL models and ECLIPSE 100.

For the first 1000 days the two COMSOL models are in agreement with the results from ECLIPSE 100. But the underprediction of the oil production rate of the two COMSOL models from that point and on leads to a smaller cumulative and total oil production compared to ECLIPSE 100. The difference that appears between the two models is very small, but according to Fig. 4.22, a more adequate matching with the ECLIPSE simulator is achieved by the COMSOL model that does not take into account the gravitational terms.

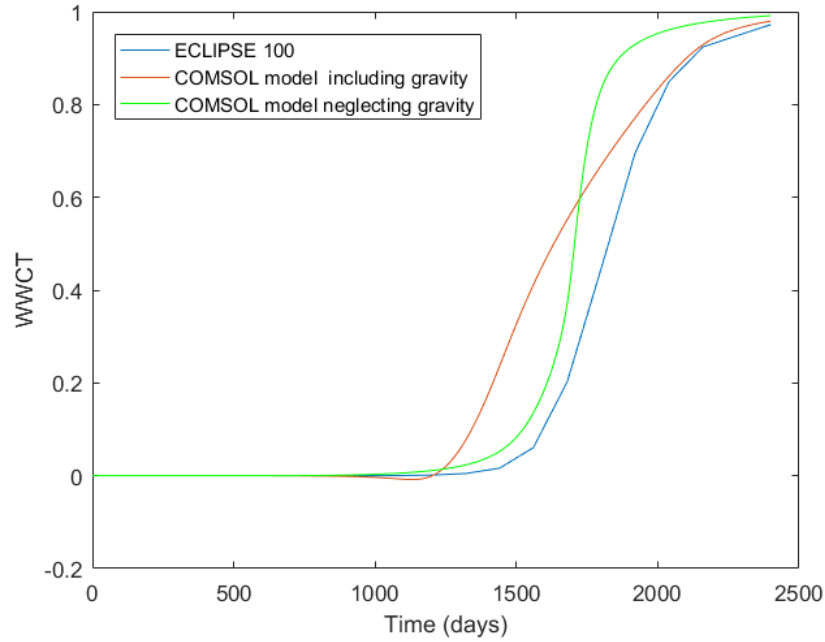


Figure 4.23: Comparison of watercut at production well with the COMSOL models and ECLIPSE 100.

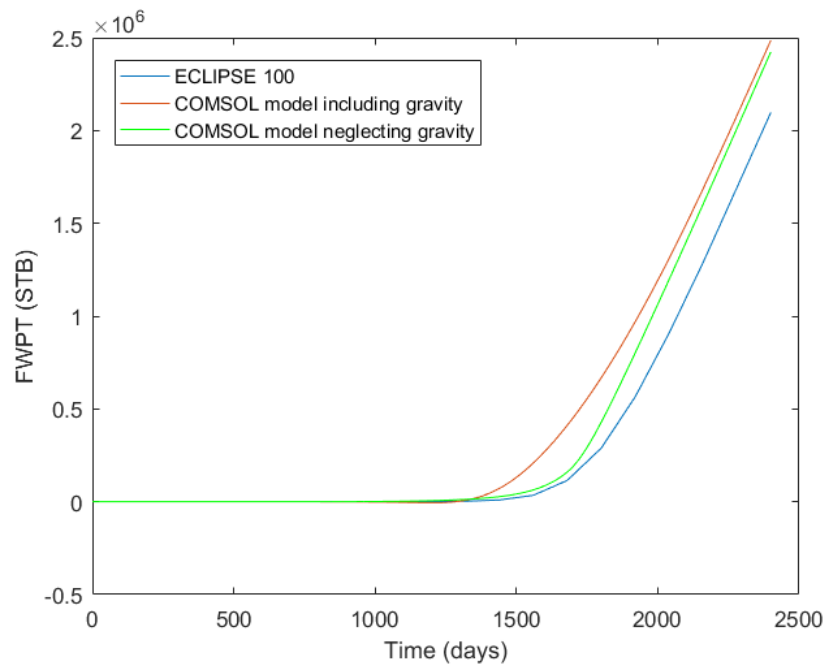


Figure 4.24: Comparison of cumulative water production with the two COMSOL models and ECLIPSE 100.

The fraction of the water phase in the production well is illustrated in [Fig. 4.23](#). Both COMSOL models overpredict the watercut. In the case of the model with the gravity the water is produced for the first time at the 1200th day and increases smoothly till the end of the simulation. For the model without the gravity, the water reaches the production well around the 1000th day, which comes into agreement with the ECLIPSE results. That, in combination with the sigmoidal profile of the watercut derived by the second model, reveals a better matching with ECLIPSE 100. Furthermore, according to [Fig. 4.24](#), both COMSOL models overpredict only slightly the cumulative quantity of the produced water but still the results of the model that neglects the gravity are closer to the ones predicted by the ECLIPSE 100 simulator.

4.5 Conclusions

In the current chapter the two-phase incompressible flow during a waterflooding process in a homogeneous anisotropic petroleum reservoir was handled with two approaches. The first model that was implemented into COMSOL Multiphysics takes into account the gravitational terms, while the second one neglects them. The pressure regime, the velocity field, the evolution of the saturation of the wetting phase were presented via 3D visualized plots, while derived values, such as the average field pressure, the BHP of the wells and the production rates of the fluids were presented. The physical problem seems to be adequately described by both models but differences were obtained between them, with the most important ones in the pressure dynamics, the velocity field and the production rates. For that reason, the same reservoir problem was simulated in ECLIPSE 100 and the numerical predictions regarding overall production were compared against the two newly-developed COMSOL PDE modules. The corresponding figures revealed that both COMSOL models were generally in good agreement with the results obtained from ECLIPSE, but numerical instabilities attributed mainly to the different discretization scheme appeared in both cases. Still, the newly-developed PDE mode with negligible gravitational terms achieved a closer matching with ECLIPSE in all cases in the specific reservoir simulation problem.

Chapter 5

Modeling Multiphase Compressible Flow

5.1 Introduction

The multiphase flow that takes place in porous media during secondary and EOR processes can not be assumed incompressible in all cases. In realistic reservoir conditions the density of the fluids is a function of the local pressure. A common approach that implements such effects is the so-called black oil model, where reservoir components are assumed to partition in three distinct fluid phases; a liquid, a gaseous and an aqueous one. The partition of the components depends on local pressure-temperature conditions. The black oil model utilizes pressure-volume-temperature (PVT) tables that describe the phase behavior of gas, oil, and water at reservoir and surface conditions. These PVT properties are functions of pressure. To account for volume changes due to different pressures at the reservoir and the surface, formation volume factors are introduced for each phase (B_g, B_o, B_w). Also, the dissolved volume of gas measured in cubic feet at surface conditions per barrel of stock tank oil is given as the ratio R_{so} .

In the current chapter the governing equations that describe the black oil model are derived and manipulated in a more convenient way, so as their implementation to be more suitable for numerical analysis with the FEM scheme. The formulation of the total velocity is applied and two equations are implemented into COMSOL's PDEs modules; one pressure equation and one saturation equation. While quite straightforward to

implement in our model, the gravitational and the capillarity terms are omitted for better numerical stability in coarser meshes. The derived equations are used for the simulation of a waterflooding recovery process in an undersaturated reservoir. From the numerical solution of the flow equations important quantities such as the oil production rate and the solution gas production rate are derived and compared with the results from ECLIPSE 100 simulator so as to evaluate the implementation of the black oil model under the current numerical scheme. It should be noted that this work constitutes the first attempt (in the literature) to formulate the actual black oil scheme in the framework of the COMSOL PDE platform.

5.2 The Black Oil Model in Porous Media

5.2.1 Black Oil Model Equations

No changes in composition of the hydrocarbons during the production are considered in a black oil simulator, beyond the solution or evolution of dissolved gas in oil, or vaporisation or dropout of condensate from gas.

The basic differential equations for the black oil model in a porous medium Ω are noted below. (Salehfar, 2006) These equations do not represent mass balances but rather balances on standard volumes.

$$\phi \frac{\partial}{\partial t} \left(\frac{S_w}{B_w} \right) + \nabla \cdot \left(\frac{1}{B_w} \underline{u}_w \right) = q_w \quad (5.2.1)$$

$$\phi \frac{\partial}{\partial t} \left(\frac{S_o}{B_o} \right) + \nabla \cdot \left(\frac{1}{B_o} \underline{u}_o \right) = q_o \quad (5.2.2)$$

$$\phi \frac{\partial}{\partial t} \left(\frac{S_g}{B_g} + \frac{R_{so} S_o}{B_o} \right) + \nabla \cdot \left(\frac{1}{B_g} \underline{u}_g + \frac{R_{so}}{B_o} \underline{u}_o \right) = q_g \quad (5.2.3)$$

Here, \underline{u}_α represents the volumetric phase velocity, which can be expressed by the Darcy law as follows

$$\underline{u}_\alpha = -\underline{k} \frac{k_{r\alpha}}{\mu_\alpha} (\nabla p_\alpha - \rho_\alpha \underline{g}), \quad \alpha = g, o, w \quad (5.2.4)$$

Where ϕ and \underline{k} denote the porosity and absolute permeability tensor of the porous system, while $S_\alpha, \mu_\alpha, \rho_\alpha, p_\alpha, \underline{u}_\alpha, B_\alpha, k_{r\alpha}$ and q_α are the saturation, viscosity, density, pressure, Darcy velocity, formation volume factor, relative permeability, and external source term, for each phase $\alpha = g, o, w$, respectively. While R_{so} is the gas solubility and \underline{g} is the gravitational, downward-pointing, constant vector.

The hydrocarbon components are lumped together to a light "gas" and heavier "oil" pseudocomponent at surface conditions. The density of the fluids at reservoir conditions are expressed as follows:

$$\begin{aligned}\rho_o &= \frac{\rho_{Os} + R_{so}\rho_{Gs}}{B_o} \\ \rho_g &= \frac{\rho_{Gs}}{B_g} \\ \rho_w &= \frac{\rho_{Ws}}{B_w}\end{aligned}\tag{5.2.5}$$

where the under script "s" designates the standard conditions.

Three-phase relative permeability can be generated from the two-phase relative permeability curves of the oil-water system and the relative permeability curves of the gas-oil system. Empirical probability models, such as the Stone I, Stone II and Baker, are widely used in oil simulation.

The equation system [Eq. \(5.2.1\)](#) - [Eq. \(5.2.3\)](#) consists of only three equations and it contains six unknowns ($p_o, p_g, p_w, S_o, S_g, S_w$), therefore the following three additional equations are required for the system to be determined:

$$\begin{aligned}S_g + S_o + S_w &= 1 \\ p_{cgo}(S_g) &= p_g - p_o \\ p_{cow}(S_w) &= p_o - p_w\end{aligned}\tag{5.2.6}$$

where p_{cgo} and p_{cow} are gas-oil and oil-water capillary pressures, respectively.

The main assumptions considered for the black oil model are: ([Diaz-Viera et al., 2008](#))

- There are three phases: water (w), oil (o) and gas (g).
- Porous matrix and fluids are slightly compressible.

- The oil phase consists of two components: non volatile oil and dissolved gas, while the water and gas phases are pure, i.e., they are compound for only one component respectively.
- Diffusion is neglected for all phases.
- It is considered that the porous media is fully saturated, but the phases are separated in the pore space.
- The whole system is in local thermodynamic equilibrium.

The black oil model is usually solved numerically by finite difference or finite volume methods, as in the case of the ECLIPSE 100 simulator. In order to implement the model with the FEM that COMSOL utilizes, the black oil model has to be reformulated in a more convenient manner. (Chen, 2000)

5.2.2 Phase Formulation

The phase formulation with the total velocity, as proposed by Chen (2000), is implemented. For expositional convenience, the phase mobility functions are introduced:

$$\lambda_\alpha = k_{r\alpha}/\mu_\alpha, \quad \alpha = g, o, w \quad (5.2.7)$$

and the total mobility

$$\lambda = \sum_{\beta} \lambda_{\beta} \quad (5.2.8)$$

Also, we define the fractional flow functions

$$f_\alpha = \lambda_\alpha/\lambda, \quad \alpha = g, o, w \quad (5.2.9)$$

so that $\sum_{\beta} f_{\beta} = 1$.

Oil being a continuous phase implies that p_o is well behaved, so we use the oil phase pressure as the pressure variable:

$$p = p_o \quad (5.2.10)$$

We now define the total velocity:

$$\underline{u} = \sum_{\beta} \underline{u}_{\beta} \quad (5.2.11)$$

Then we use Eq. (5.2.10) and Eq. (5.2.11), carry out the differentiation indicated in Eq. (5.2.1) - Eq. (5.2.3) and apply Eq. (5.2.4) and Eq. (5.2.7) to obtain the differential equations:

$$\underline{\mathbf{u}} = -\underline{\mathbf{k}}\lambda \left(\nabla p - G_\lambda + \sum_{\beta} f_{\beta} \nabla p_{c\beta o} \right),$$

$$\nabla \cdot \underline{\mathbf{u}} = \sum_{\beta} B_{\beta} \left(q_{\beta} - \phi S_{\beta} \frac{\partial}{\partial t} \left(\frac{1}{B_{\beta}} \right) - \underline{\mathbf{u}}_{\beta} \cdot \nabla \left(\frac{1}{B_{\beta}} \right) \right) - B_g \left(R_{so} q_o + \frac{\phi S_o}{B_o} \frac{\partial R_{so}}{\partial t} + \frac{1}{B_o} \underline{\mathbf{u}}_o \cdot \nabla R_{so} \right) \quad (5.2.12)$$

and

$$\phi \frac{\partial S_{\alpha}}{\partial t} + \nabla \cdot \underline{\mathbf{u}}_{\alpha} = B_{\alpha} \left(q_{\alpha} - \phi S_{\alpha} \frac{\partial}{\partial t} \left(\frac{1}{B_{\alpha}} \right) - \underline{\mathbf{u}}_{\alpha} \cdot \nabla \left(\frac{1}{B_{\alpha}} \right) \right), \quad (5.2.13)$$

$$\underline{\mathbf{u}}_{\alpha} = f_{\alpha} \underline{\mathbf{u}} + \underline{\mathbf{k}} f_{\alpha} \sum_{\beta} \lambda_{\beta} (\nabla (p_{c\beta o} - p_{c\alpha o} - (\rho_{\beta} - \rho_{\alpha}) \underline{\mathbf{g}}))$$

for $\alpha = o, w$, where

$$G_{\lambda} = \underline{\mathbf{g}} \sum_{\beta} f_{\beta} \rho_{\beta} \quad (5.2.14)$$

The equations are, respectively, the pressure and saturation equations.

5.3 Model Implementation in COMSOL Multiphysics

For the implementation of the black oil model in COMSOL Multiphysics, the gravity and the capillary forces are neglected. Also, it is assumed that the reservoir is in the undersaturated state and the average pressure remains above the bubble point (26.3 MPa), namely all the gas is dissolved into the oil phase (constant R_{so} value). The

numerical implementation of the model is, hence, reduced to the biphasic case for simplicity and without loss of generality however.

The performance of the two-phase compressible flow is simulated in the reservoir with the dimensions and properties presented in the previous chapter. The two wells are placed in the exact same locations and with the same dimensions, as shown in [Fig. 4.2](#).

Since the average pressure of the reservoir is maintained above the bubble point pressure, no gas phase exists and the relative permeabilities of the oil and the water phase can hence be given as functions of the water phase saturation.

S_w	kr_w	kr_o
0.10	0.000	1.000
0.16	0.0005	0.854
0.22	0.004	0.716
0.28	0.0135	0.586
0.34	0.032	0.465
0.40	0.0625	0.354
0.46	0.108	0.253
0.52	0.172	0.164
0.58	0.256	0.089
0.64	0.365	0.032
0.70	0.500	0.000
0.80	0.667	0.000
0.90	0.833	0.000
1.00	1.000	0.000

Table 5.1: Phase relative permeability fractions vs water saturation for the black oil model.

The PVT properties of the reservoir fluids are listed in the following tables.

Pressure MPa	Oil formation volume factor, B_o vol/svol	Oil viscosity, μ_o cP
26.3	1.447	0.691
29.1	1.441	0.694
31.8	1.434	0.697

Table 5.2: Oil phase properties.

Reference pressure MPa	Water formation volume factor, B_w vol/svol	Water viscosity, μ_w cP
27.52	1.0231	0.940

Table 5.3: Water phase properties.

The set of values are inserted into COMSOL as interpolation functions. For the FVF piecewise cubic relationship is selected while for the viscosity the cubic spline relationship is applied. The extrapolation is made out of the nearest function.

The water FVF and viscosity are considered practically stable so they are inserted as parameters into COMSOL.

Parameters and variables for the implementation of the black oil model are listed in the following tables.

Parameters	Units	Values
Porosity, ϕ	-	0.2
Absolute permeability, x direction, k_x	mD	250
Absolute permeability, y direction, k_y	mD	200
Absolute permeability, z direction, k_z	mD	25
Connate water saturation, S_{wc}	-	0.1
Oil density at standard conditions, ρ_{Os}	kg/m ³	800
Gas density at standard conditions, ρ_{Gs}	kg/m ³	0.40
Water density at standard conditions, ρ_{Ws}	kg/m ³	1000
Solution gas-oil ratio, R_{so}	-	137.1
Water formation volume factor, B_w	-	1.0231
Water viscosity, μ_w	cP	0.94
Pressure, p_{in}	MPa	27.52
Injection rate, u_{in}	m/s	$9.03 \cdot 10^{-5}$
Numerical diffusivity, c	m ² /s	$8 \cdot 10^{-5}$

Table 5.4: Parameters for the black oil model.

Variables	Units	Expression
Oil phase saturation, S_o	-	$1 - S_w$
Water phase mobility, λ_w	1/(Pa·s)	$\frac{k_{rw}}{\mu_w}$
Oil phase mobility, λ_o	1/(Pa·s)	$\frac{k_{ro}}{\mu_o}$
Total mobility, λ	1/(Pa·s)	$\lambda_w + \lambda_o$
Water phase fractional flow, f_w	-	$\frac{\lambda_w}{\lambda}$
Oil phase fractional flow, f_o	-	$\frac{\lambda_o}{\lambda}$
Total velocity, x component, u_x	m/s	$-k_x \lambda \frac{\partial p}{\partial x}$
Total velocity, y component, u_y	m/s	$-k_y \lambda \frac{\partial p}{\partial y}$
Total velocity, z component, u_z	m/s	$-k_z \lambda \frac{\partial p}{\partial z}$
Water phase velocity, x component, u_{wx}	m/s	$f_w u_x$
Water phase velocity, y component, u_{wy}	m/s	$f_w u_y$
Water phase velocity, z component, u_{wz}	m/s	$f_w u_z$
Oil phase velocity, x component, u_{ox}	m/s	$f_o u_x$
Oil phase velocity, y component, u_{oy}	m/s	$f_o u_y$
Oil phase velocity, z component, u_{oz}	m/s	$f_o u_z$

Table 5.5: Variables for the black oil model.

General Form PDE

The COMSOL Multiphysics PDE mode for time dependent analysis in the general form is used for Eq. (5.2.13) with p as the dependent variable. The velocity components in each direction (u_x, u_y, u_z), as expressed in Table 5.5, are inserted in the conservative flux vector section. The right part of the equation is inserted as a source term in the PDE interface, with $q_w = 0$.

Coefficient Form PDE

The coefficient form PDE is selected with S_w as the dependent variable. The conservative flux source is described by the components of the water phase velocity (u_{wx}, u_{wy}, u_{wz}), as shown in Table 5.5. The source term is described by the right part of the equation, for $q_w = 0$. The numerical diffusivity c is set isotropic and equal to the prescribed value in Table 5.4.

Initial Conditions

$$p(t_0) = p_{in}, \frac{\partial p}{\partial t} = 0$$

$$S_w(t_0) = S_{wc}, \frac{\partial S_w}{\partial t} = 0$$

Boundary Conditions

Inlet conditions (constant rate)

$$-\underline{n} \cdot \underline{u} = u_{in}$$

$$S_w = 1$$

Outlet conditions (constant pressure)

$$p = p_{out} = p_{in}$$

$$-\underline{n} \cdot (-c\nabla S_w + \underline{u}_w) = -\underline{u}_w$$

Top, bottom and side walls (no flux)

$$-\underline{n} \cdot \underline{u} = 0$$

$$-\underline{n} \cdot (-c\nabla S_w + \underline{u}_w) = 0$$

Mesh and Solver

A free tetrahedral mesh with maximum element size 137 ft is applied. The areas around the injection well and the production well are refined three times.

The segregated time-dependent solver with free time stepping is used. At the first segregated step the dependent variable p is computed and following is the dependent variable S_w at the second step.

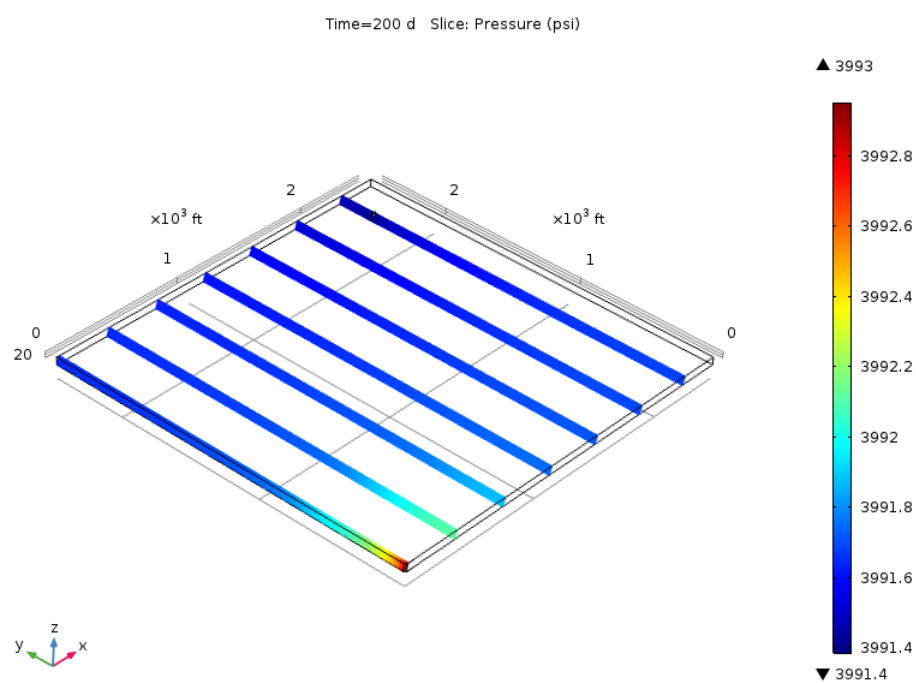
The PDEs with the imposed initial and boundary conditions are solved for a range of (0,1,2600) days.

5.4 Results and Discussion

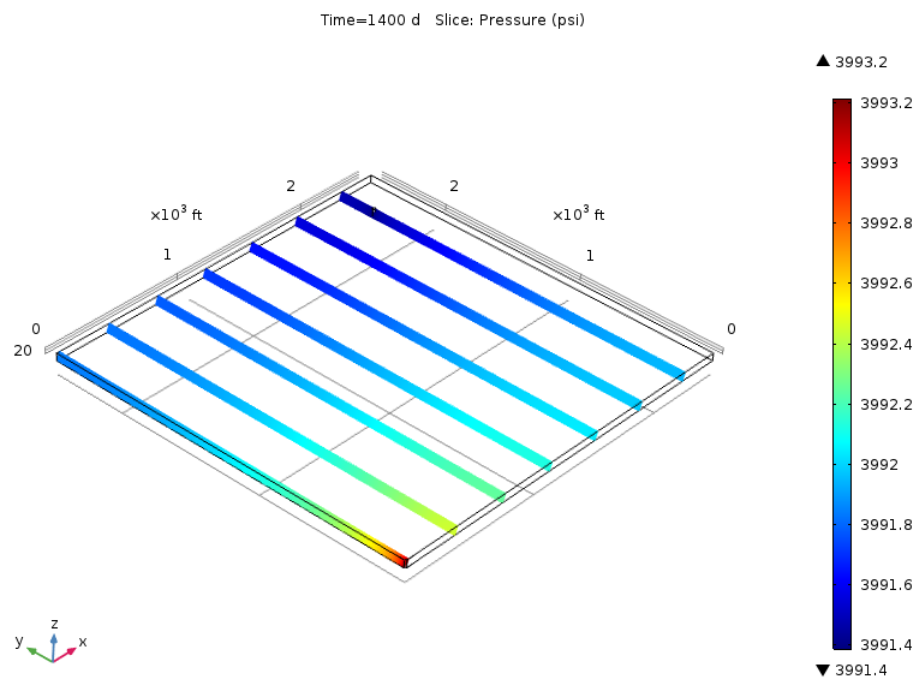
5.4.1 The Black Oil Model in COMSOL

The above system of PDEs is solved for the pressure and the water phase saturation. The oil phase saturation is calculated at each time step from the water phase saturation.

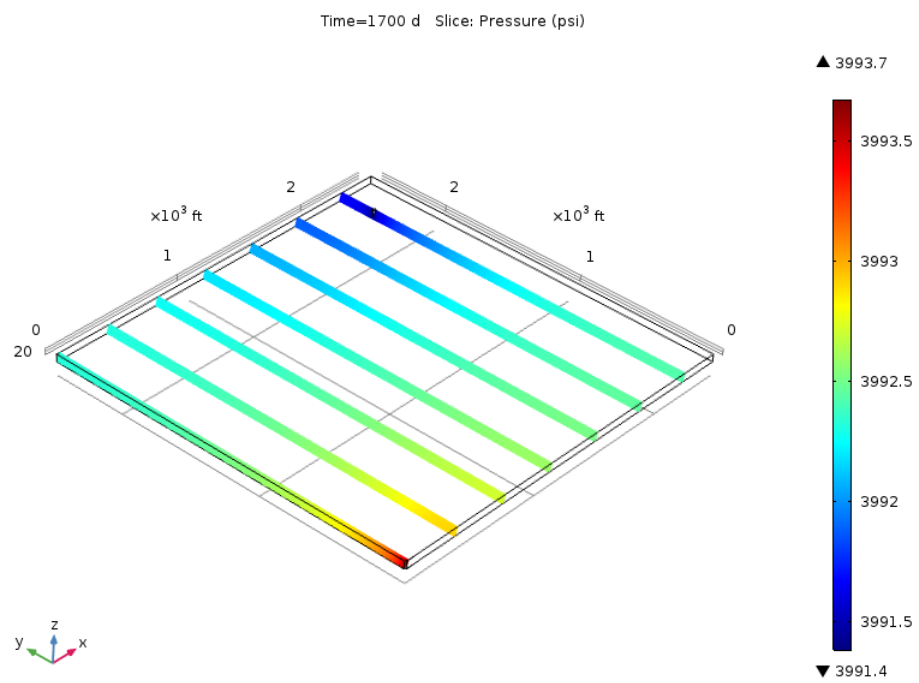
Firstly, the pressure regime that prevails in the reservoir during different times throughout the oil recovery process is presented in the next 3D surface plots.



(a) $t = 200$ day



(b) $t = 1400$ days



(c) $t = 1700$ days

5.4. RESULTS AND DISCUSSION

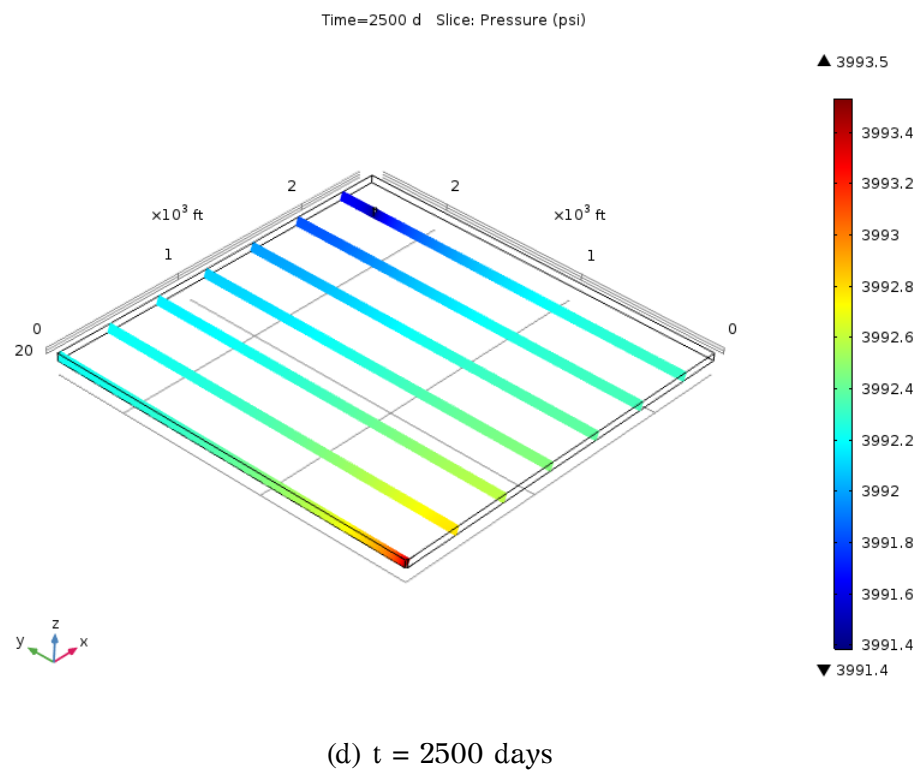


Figure 5.1: Field pressure regime; slice plots.

The injection well is controlled by constant rate, thus a varying pressure regime in the area around it prevails during the waterflooding process. At the early days of the recovery (200 days) the pressure is greater in the area around the injector. As the water saturation fronts propagate towards the production well, a small pressure increase is observed in the rest region of the reservoir, as shown in Fig. 5.1b. The waterbreakthrough occurs around the 1520th day of the injection, which creates a bigger pressure increase almost in the whole reservoir, as shown in Fig. 5.1c. At that time the BHP in the injection well meets the higher pressure value, that of 3993.7 psi. No variation in the pressure regime is observed after the breakthrough and till the end of the process, when the BHP in the injector is 3993.5 psi. The pressure prevailing in the area around the production well stays at 3991.4 psi throughout the recovery process, which is the minimum pressure value in the reservoir at all time selections. That is physically correct, as the production is controlled by constant BHP, which has been set equal to 3991.4 psi (27.52 MPa).

The average field pressure as well as the bottomhole pressure of each well are computed and presented in the next figures for the whole duration of the waterflooding process.

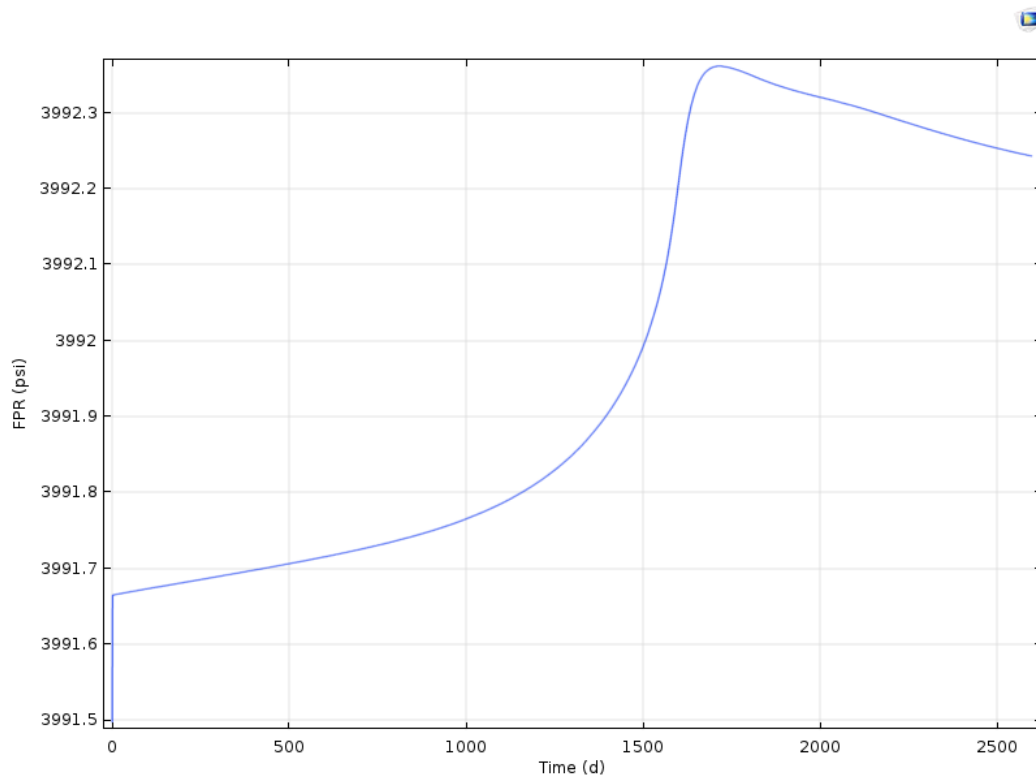


Figure 5.2: Field average pressure.

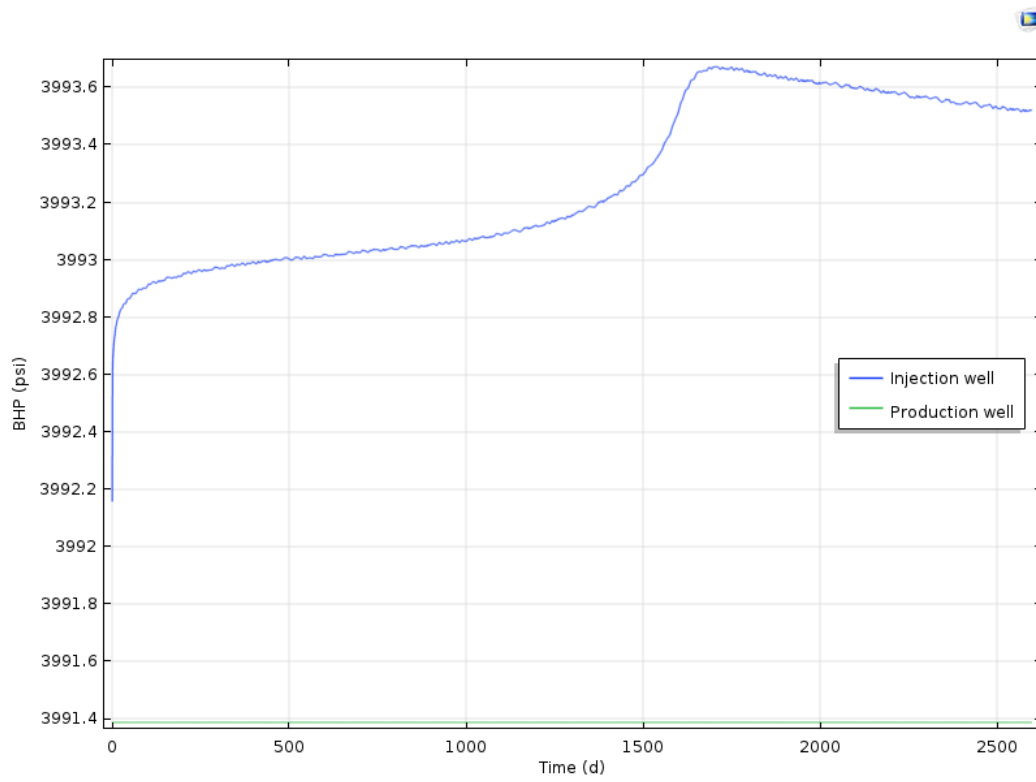


Figure 5.3: Bottomhole pressure of the two wells.

5.4. RESULTS AND DISCUSSION

The field average pressure follows an increasing rate till the 1600th day of the recovery process, when the water breakthrough occurs. The BHP at the injection well follows the same behavior. The change of the mobility of the fluids in the production well causes a pressure drop in the BHP at the injection well and consequently in the average reservoir pressure, so as the condition of the constant BHP at production well to be fulfilled.

The velocity field is also computed from the solution of the PDEs of the black oil model. Arrow surface plot is used for its representation in the following figure. The flow from the injection to the production well is visually verified.

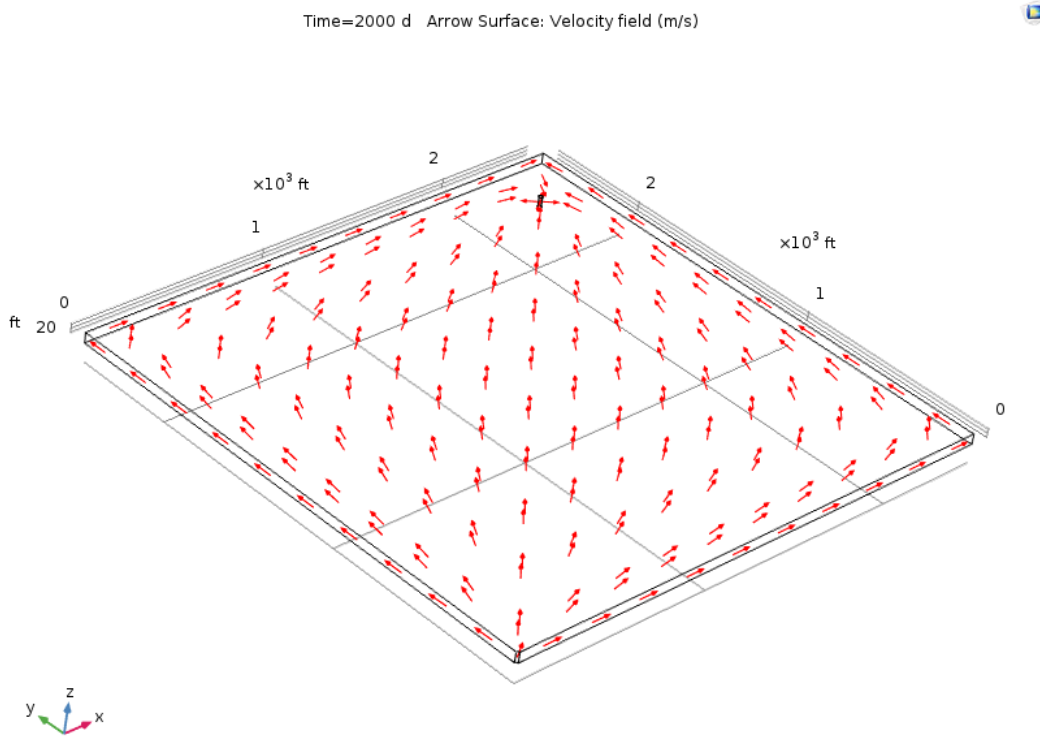


Figure 5.4: Velocity field; arrow surface plot.

The evolution of the water saturation at different times after the start of the injection is depicted through isosurfaces in the following set of figures.

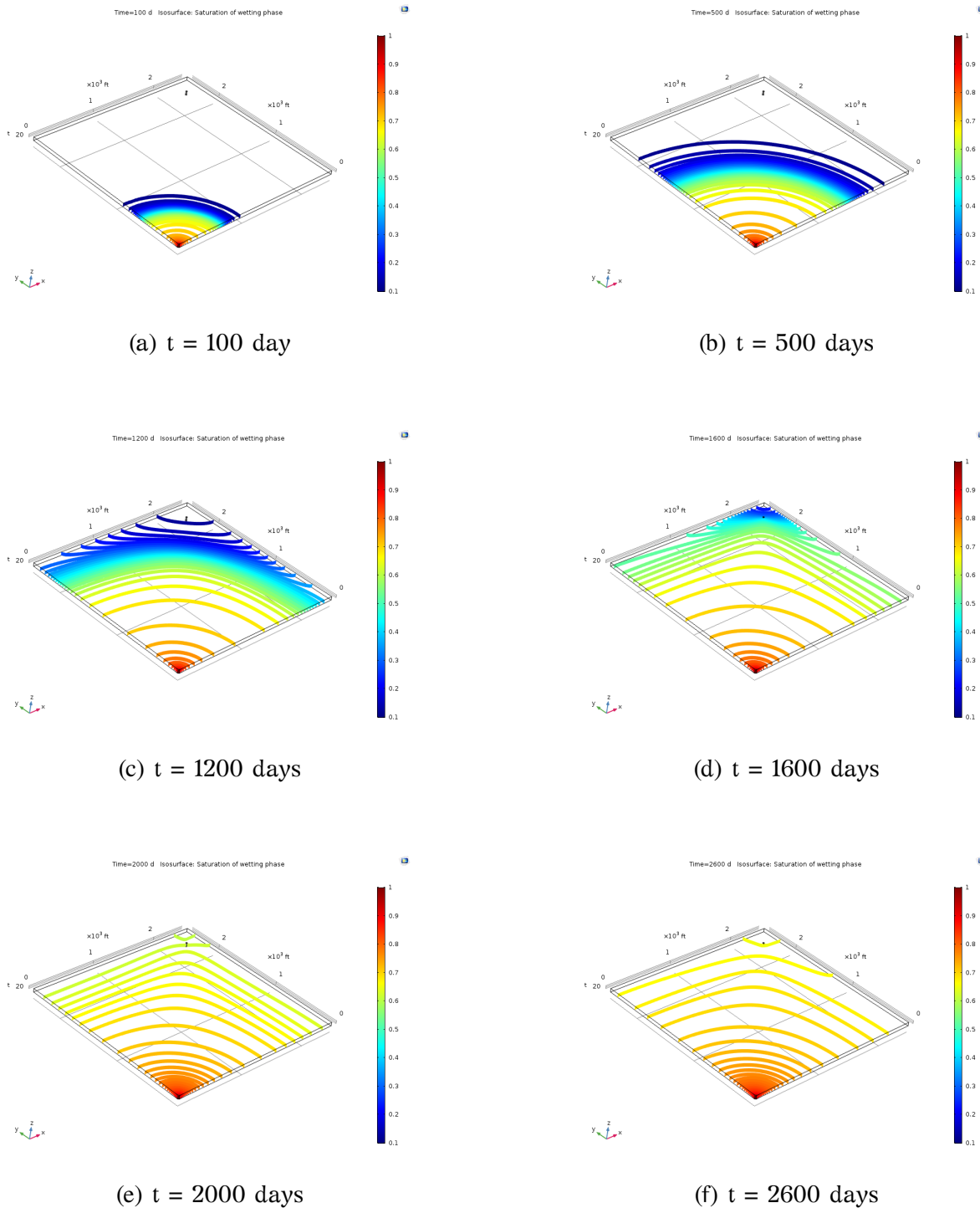


Figure 5.5: Saturation evolution of the water phase at different times; isosurface plots.

The initial water saturation per % of pore space is 0.1 in the whole reservoir while the oil saturation is 0.9. With the start of the recovery process, the water floods enter the reservoir from the injector and move toward the production well, displacing the

hydrocarbons and forces them to be produced. At the end of the simulation study, the greater amount of the hydrocarbons has been efficiently recovered, as shown by Fig. 5.5f.

Following is the production rate of the hydrocarbons at standard conditions. The initial oil in reservoir conditions is considered to be live, which means that it contains gas dissolved in it. As the oil is produced and travels to the surface through the wellbore, the pressure of the phase decreases and so the dissolved gas is released and produced as free gas. Thus, two production rates at surface conditions can be considered; the oil production rate and the solution gas production rate. The production rates can be calculated by simply performing an integration of the phase velocity in the production walls and using the oil formation volume factor and the gas-oil-ratio values from the given PVT tables.

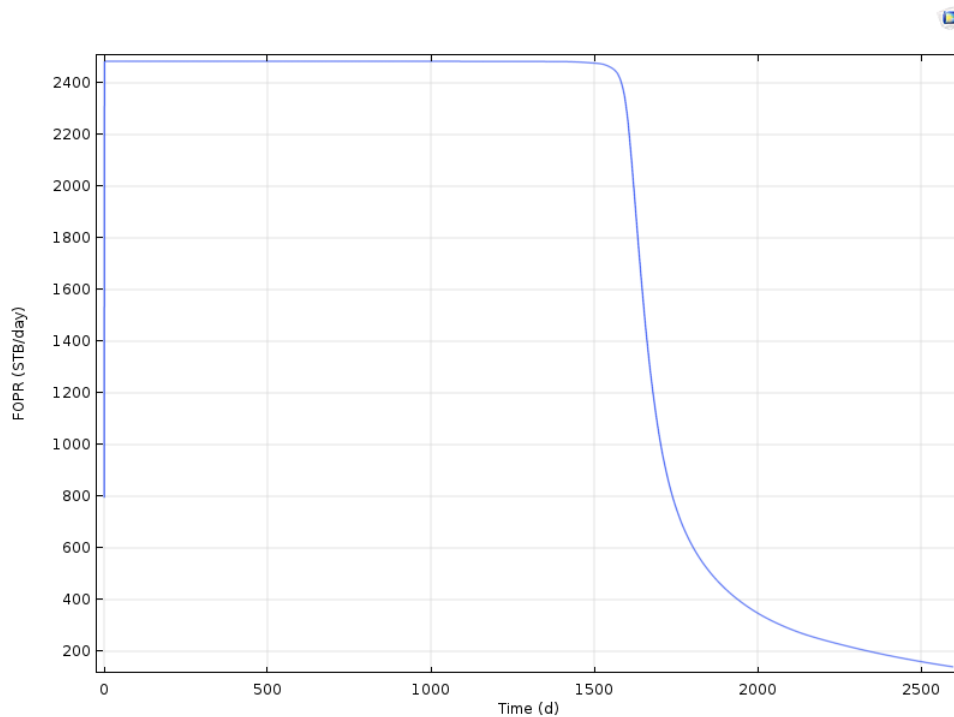


Figure 5.6: Oil production rate.

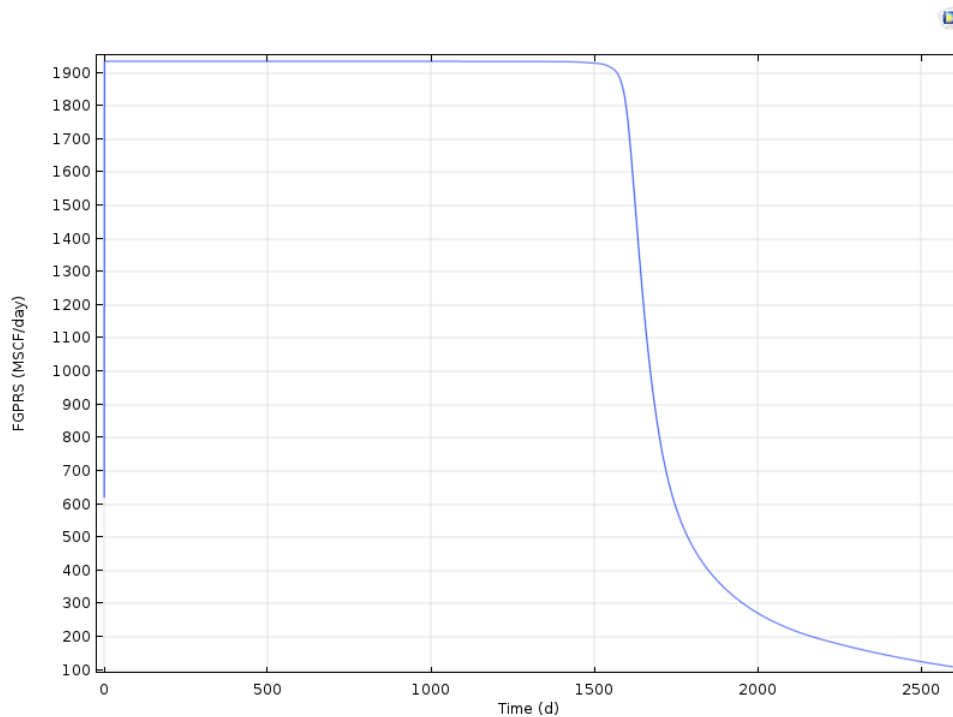


Figure 5.7: Solution gas production rate.

With the beginning of the waterflooding process almost 2500 stb of oil are produced daily. The production rate is constant till the 1520th day, when it starts decaying with an abrupt manner, indicating that the existing pressure is not sufficient to maintain the hydrocarbon production due to the waterbreakthrough. During this time period, almost 1950 Mscf of dissolved gas are simultaneously produced, followed also by an abrupt decrease of the production rate till the 100 Mscf/day at the 2600th day, when the process is terminated. The corresponding oil production rate at the last day is less than 200 stb/day. The two production rate profiles are exactly the same, as expected, since the solution gas production rate is calculated according to the velocity of the oil phase in reservoir conditions.

Following is the production rate of the water phase at standard conditions.

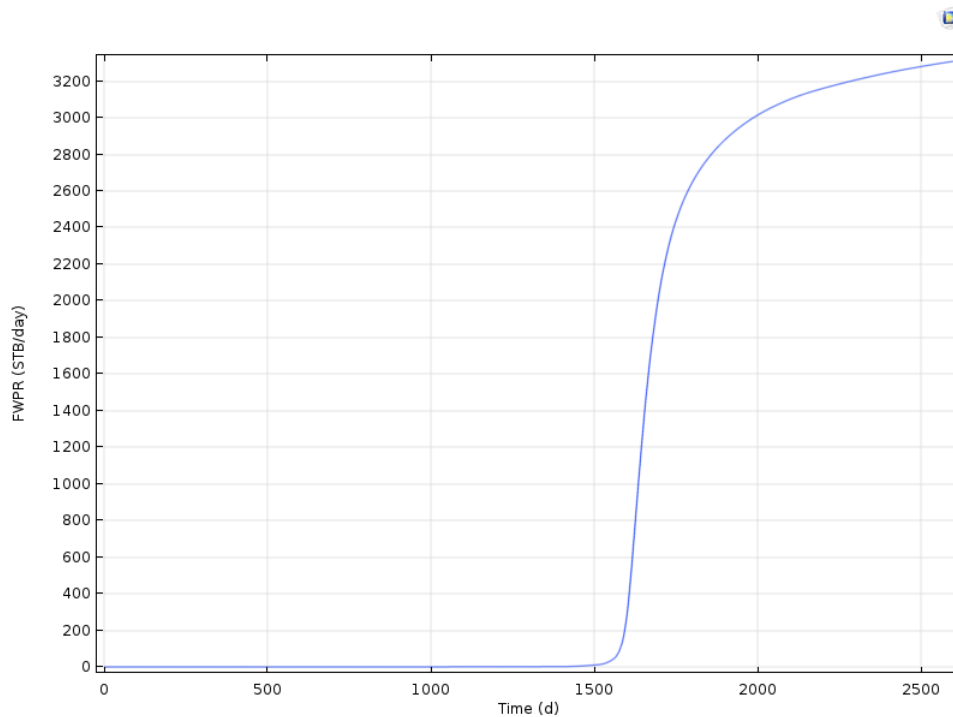


Figure 5.8: Water production rate.

According to the above figure, no water is produced during the first 1520 days of the recovery process. The breakthrough occurs at the 1520th day, when an abrupt increase in the production rate is observed for almost 250 days, followed by a smoother one till the end of the water injection. At that time, the water production exhibits its maximum rate, that of almost 3400 stb/day.

5.4.2 Comparison with ECLIPSE 100

In order to evaluate the numerical analysis of the waterflooding process using the black oil model equations in the COMSOL Multiphysics, the physical model is also simulated in the ECLIPSE 100 software. The controlling mechanism of injection is the constant rate of water at 3500 stb/day, while the production is controlled by the bottomhole pressure target, set equal to 3991.4 psi. The production rates, the cumulative and total production of the hydrocarbons as well as the watercut at the production well are presented for the comparison of the two simulators.

Firstly, the stock tank barrels of oil produced daily and the cumulative stock tank barrels

produced from the secondary recovery process are presented for the two simulators.

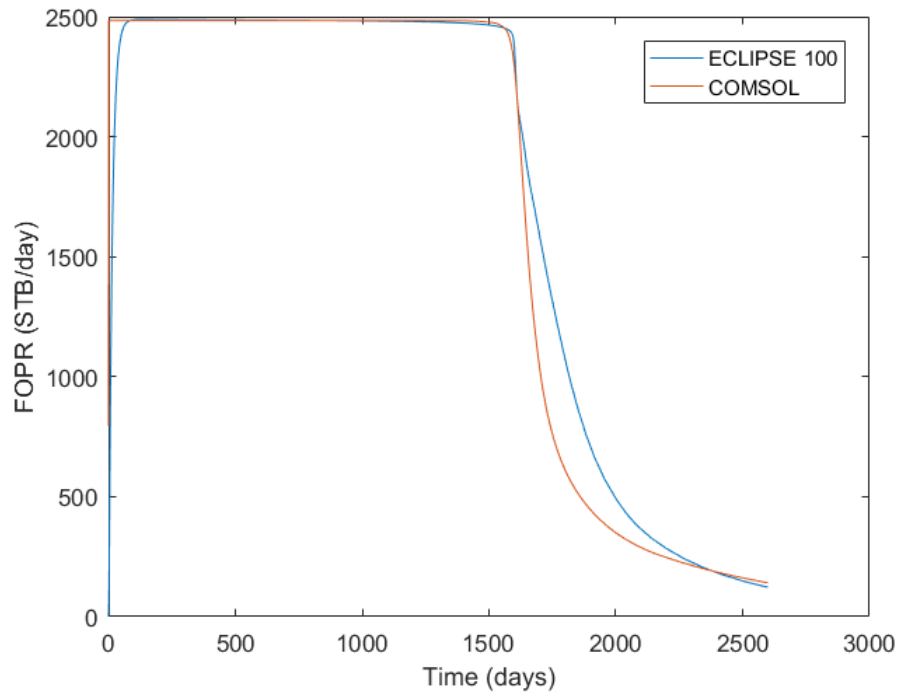


Figure 5.9: Comparison of oil production rate with the two simulators.

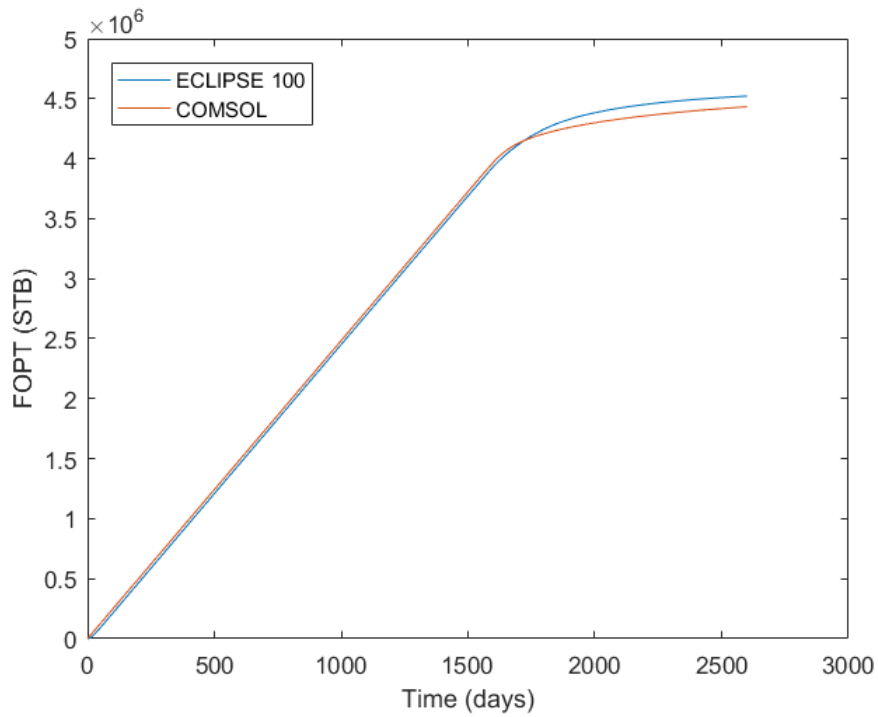


Figure 5.10: Comparison of cumulative oil production with the two simulators.

Fig. 5.9 illustrates the profile of the oil production rate for the two simulators. Both COMSOL and ECLIPSE 100 predict a maximum production rate of 2500 stb per day for almost the same time period, that of approximately 1520 days. Differences in the production rate between the two simulators become distinct after that day, when the production rate starts decreasing. In specific, the decaying rate is more abrupt when computed with COMSOL Multiphysics and smoother when computed with ECLIPSE 100. That means that for the same time selection, COMSOL underestimates the rate of the produced oil compared to ECLIPSE simulator. As a result, the cumulative oil production that is estimated from the two models meets also some differences.

The cumulative oil production is presented in Fig. 5.10. The cumulative oil produced is the same for the two simulators till the day that the waterbreakthrough occurs, approximately the 1520th. After that, the ECLIPSE simulator predicts a cumulative oil production that is slightly greater than the one that COMSOL estimates. The total quantity of oil that is produced from the recovery process according to COMSOL is almost $4.4 \cdot 10^6$ stb, which is 1% less than ECLIPSE 100.

Following are the daily production rate and the cumulative metric cubic feet of dissolved gas for the two simulators.

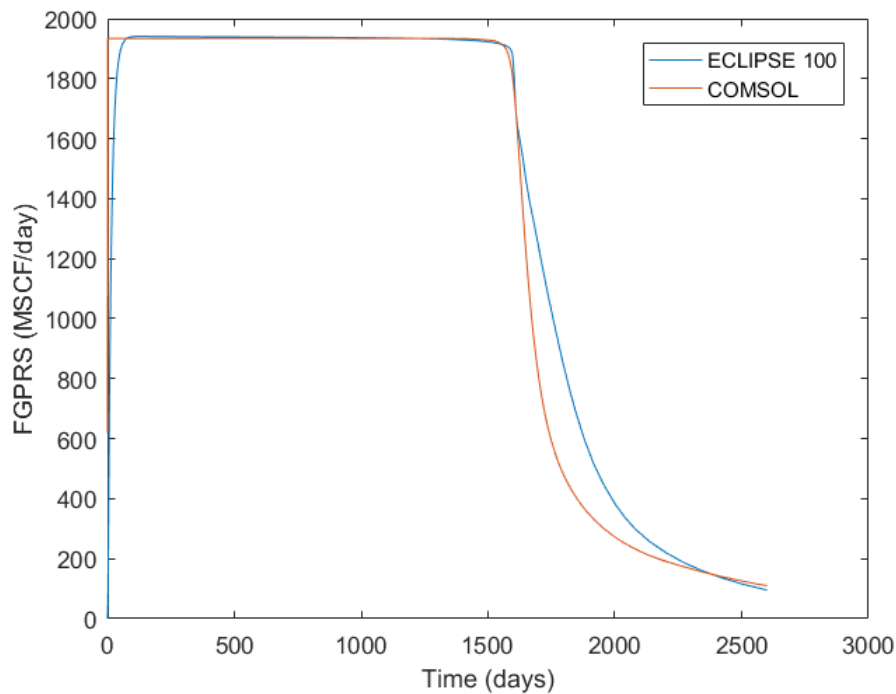


Figure 5.11: Comparison of solution gas production rate with the two simulators.

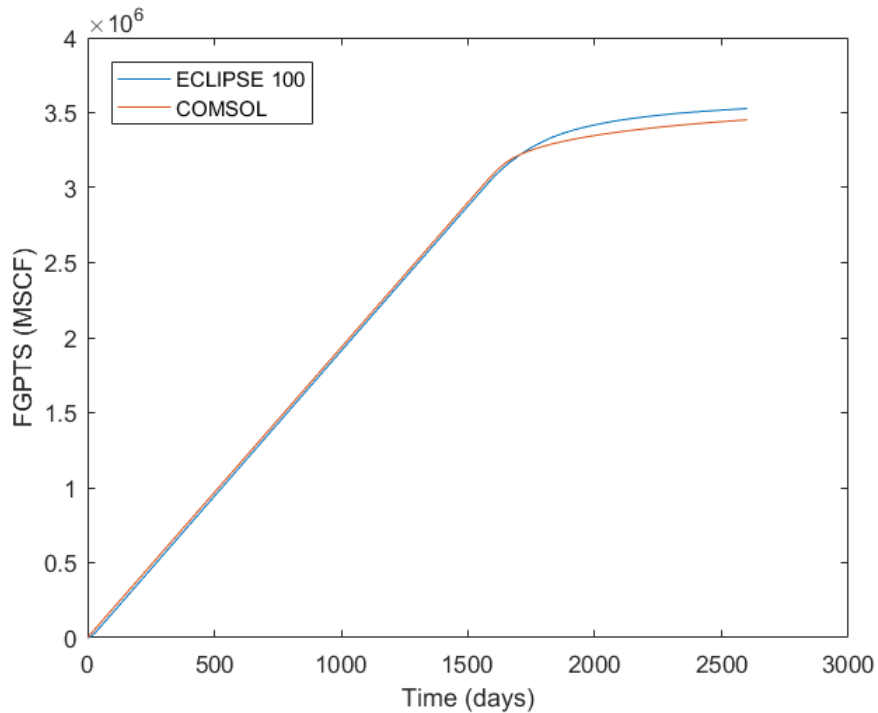


Figure 5.12: Comparison of cumulative solution gas production with the two simulators.

The gas that exists as a solution in the oil at reservoir conditions is produced at the surface with the same constant rate, that of 1935 Mscf/day, for almost 1520 days according to both the simulators. The decaying production profile differs slightly in the two simulators, with COMSOL estimating a more abrupt decaying rate than that of ECLIPSE 100. That leads to a smaller estimated cumulative solution gas production with COMSOL, around $3.45 \cdot 10^6$ Mscf, while ECLIPSE estimates $3.53 \cdot 10^6$ Mscf. The difference is only 2%.

The fraction of the water phase at the production well, commonly referred to as watercut, estimated with the two simulators is illustrated in the next graph. Presented is also the cumulative amount of produced water at each time step.

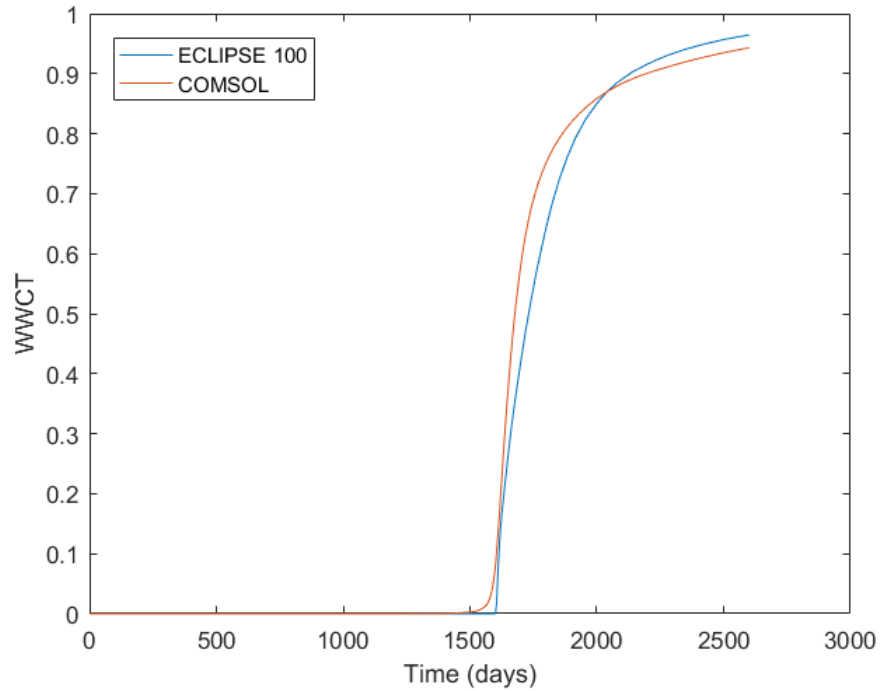


Figure 5.13: Comparison of watercut at production well with the two simulators.

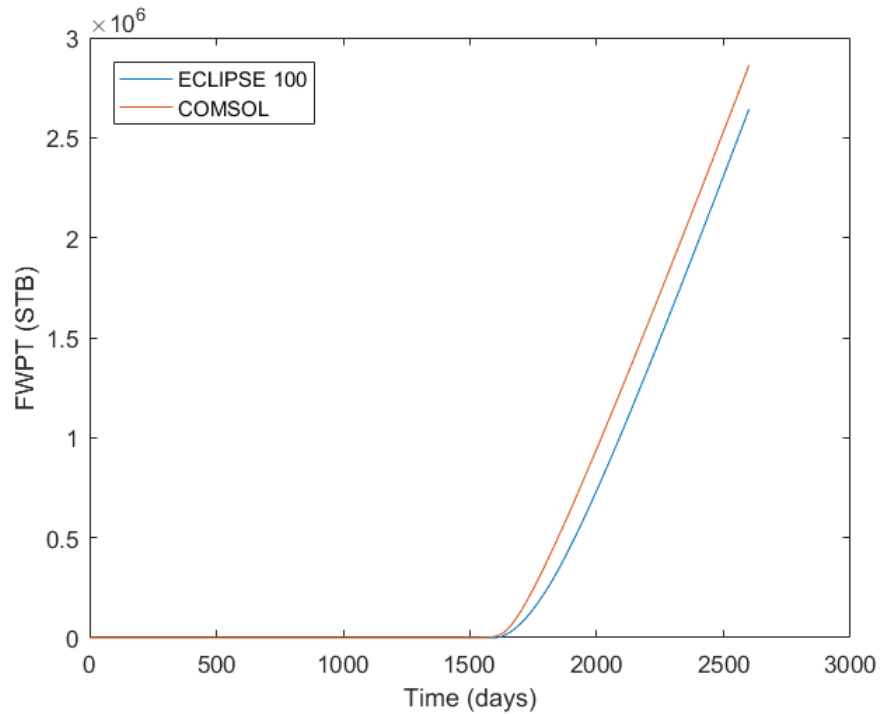


Figure 5.14: Comparison of water total production with the two simulators.

Referring to [Fig. 5.13](#), the watercut is zero at the production well till the 1520th day of the waterflooding, when the water phase reaches the drainage area of the producer, as estimated by COMSOL simulator. According to ECLIPSE 100, the breakthrough happens around 10 days later. From that point and on, the watercut follows an increasing rate in both cases, but an abrupter one according to COMSOL. Difference is also obtained during the last days of the secondary recovery, with ECLIPSE 100 predicting bigger fraction of the water phase at the production well. COMSOL estimates however a total water production 8% higher than that of ECLIPSE 100, as indicated by [Fig. 5.14](#).

5.5 Conclusions

In the current chapter the two-phase compressible flow that takes place in the porous media during a waterflooding recovery process in a homogeneous anisotropic reservoir was simulated in COMSOL Multiphysics using the black oil model equations. The interpretation of the physical phenomenon is described successfully enough by the implemented model, as shown by the 3D visualized plots of the pressure regime, the velocity field and the saturation evolution of the water phase. The numerical implementation of the fluid flow equations was evaluated by comparing against the ECLIPSE 100 simulator. In the estimation of the production and cumulative rates of both the hydrocarbons and the water at surface conditions COMSOL exhibits a very good matching and, hence, its use as a black oil simulator can be considered as a trustworthy one.

Chapter 6

Conclusions of MSc Thesis

The commercially-available COMSOL Multiphysics numerical platform was used in the current thesis for the simulation of single and two-phase flows in porous media, either by using the provided physics interfaces or setting up the numerical model with the PDEs module. Initially, two numerical models were implemented for the study of the hydrodynamic dispersion coefficient from pore- to REV-scale during a tracer injection. The values of the hydrodynamic dispersion coefficient that were obtained from the rigorous pore-scale modeling and the modeling that approaches the porous medium as a homogeneous one, indicated that effective transport properties can be efficiently used for the description of the phenomena that take place at the macroscopic (REV-scale) level. Then the two-phase incompressible flow that takes place during the displacement process of waterflooding was numerically solved with and without the gravitational terms, using the general and coefficient forms of the PDE mode. The effect of gravity became distinct not only on the interpretation of the phenomenon but also on its quantification, as different oil and water production rates were observed for the two models. Contrary to what was intuitively expected, a direct comparison with ECLIPSE 100 simulator indicated that the model without the gravity comes into a closer agreement with the results from ECLIPSE 100, thus it can be successfully used for the prediction of hydrocarbons recovery. At the last part, the black oil model equations were implemented in COMSOL Multiphysics and used for the simulation of a waterflooding process, taking into account the compressibility of the reservoir fluids. The matching with the results from ECLIPSE 100 was even closer, indicating that COMSOL Multiphysics can also be used as a trustworthy tool for the simulation of more complex problems in EOR recovery

processes by implementing also the appropriate PDEs that describe tracer (mass) transfer, thermal stimulation and surfactant processes.

One last point that should be outlined concerning the numerical resolution of the flow models with the finite element method is the effect of the stabilization technique and the scale of discretization in the solution. The multiphase flow in porous media is strongly convection-dominated, as opposed to diffusive-dominated processes. The saturation profile is discontinuous and the injected phase creates a very sharp front that needs to be numerically resolved for numerical stability which is very difficult to do with FEM, so artificial diffusion was used as a stabilization technique. Extra care must be taken to the range of values of the artificial coefficient to be set in accordance with other parameters as they should not constitute the main transport mechanism in the system, which is the pure convection for the water saturation. Apart from that, the models must be properly resolved by the mesh, namely a very dense meshing of the computational domain was required for the solution of the fluid flow equations. While improving the expected accuracy of the numerical solution, the above effects significantly increase the required computational cost compared to a finite-difference solver such as ECLIPSE 100, a drawback of the COMSOL software. But the finer spatial resolution and time stepping that the fine element analysis utilizes provide a more detailed description of the solution, increasing the robustness of the method. Hence, in view of the scale and resolution requirements for the flow models, the standard finite element approach that COMSOL Multiphysics utilizes as a discretization scheme was found adequate enough in all cases.

A study regarding the optimization between the solver and the mesh that the COMSOL platform utilizes for multiphase fluid flow simulations in porous media is recommended as a future work.

Bibliography

- T. Ahmed. Chapter 11 - Oil Recovery Mechanisms and the Material Balance Equation BT - Reservoir Engineering Handbook (Fourth Edition). pages 733–809. Gulf Professional Publishing, Boston, 2010. ISBN 978-1-85617-803-7. doi: <https://doi.org/10.1016/B978-1-85617-803-7.50019-5>.
- S. B. Allison, G. A. Pope, and K. Sepehrnoori. Analysis of field tracers for reservoir description. *Journal of Petroleum Science and Engineering*, 5(2):173–186, 1991. ISSN 0920-4105. doi: [https://doi.org/10.1016/0920-4105\(91\)90066-V](https://doi.org/10.1016/0920-4105(91)90066-V).
- L. Anisimov. The Use of Tracers for Reservoir Characterization, 2009.
- J. Bear. *Dynamics of Fluids in Porous Media*. Dover Civil and Mechanical Engineering Series. Dover, 1972. ISBN 9780486656755.
- T. I. Bjørnarå and E. Aker. Comparing Equations for Two-Phase Fluid Flow in Porous Media. *COMSOL Conference*, (2):7, 2008.
- T. Bjørnstad, K. Garder, I. Hundere, and O. B. Michelsen. Tracer Tests in Oil Appraisal and Reservoir Evaluation: State of the Art BT. pages 261–270. Springer Netherlands, Dordrecht, 1990. ISBN 978-94-009-0791-1. doi: [10.1007/978-94-009-0791-1_22](https://doi.org/10.1007/978-94-009-0791-1_22).
- Z. Chen. Formulations and Numerical Methods of the Black Oil Model in Porous Media. *Society*, 38(2):489–514, 2000.
- Comsol. Subsurface Flow Module. *Subsurface Flow Module*, pages 1–12, 2015.
- M. A. Diaz-Viera, D. A. Lopez-Falcon, A. Moctezuma-Berthier, and A. Ortiz-Tapia. COMSOL implementation of a multiphase fluid flow model in porous media. *Proceedings of the COMSOL Conference*, 2008.

- F. A. L. Dullien. 6 - Miscible Displacement and Dispersion BT - Porous Media (Second Edition). pages 487–566. Academic Press, San Diego, 1992. ISBN 978-0-12-223651-8. doi: <https://doi.org/10.1016/B978-0-12-223651-8.50012-2>.
- D. W. Green and G. P. Willhite. *Enhanced Oil Recovery*. SPE textbook series. Henry L. Doherty Memorial Fund of AIME, Society of Petroleum Engineers, 1998. ISBN 9781555630775.
- K. H. Huebner, D. L. Dewhirst, D. E. Smith, and T. G. Byrom. *THE FINITE ELEMENT METHOD FOR ENGINEERS, 4TH ED.* Wiley India Pvt. Limited, 2008. ISBN 9788126516407.
- O. Meshioye, E. Mackay, E. Ekeoma, and C. Martinez. *Optimization of Waterflooding Using Smart Well Technology*, 2010.
- P. Ogbeiwi, Y. Aladeitan, and D. Udebhulu. An approach to waterflood optimization: case study of the reservoir X. *Journal of Petroleum Exploration and Production Technology*, 2017. ISSN 2190-0558. doi: 10.1007/s13202-017-0368-5.
- T. K. Perkins and O. C. Johnston. *A Review of Diffusion and Dispersion in Porous Media*. 1963. doi: 10.2118/480-PA.
- H. Salehfar. *The Black Oil Model*. pages 283–345, 2006.
- X. Zhang. *Upscaling of the Two-Phase Flows in Petroleum Reservoirs*. Number September. 2011. ISBN 9788792481542.

List of Figures

3.1	Artificial porous structure.	16
3.2	Velocity magnitude in the artificial porous structure; surface plot.	19
3.3	Velocity field in a zoomed area of the artificial porous structure; arrow surface plot.	20
3.4	Tracer concentration profile at different times in the artificial porous structure.	21
3.5	Average tracer concentration at different times for the pore-scale modeling.	22
3.6	Homogeneous porous medium.	24
3.7	Tracer concentration profile at different times in the homogeneous porous medium.	27
3.8	Average tracer concentration at different times for the REV-scale modeling.	28
4.1	The inverted five-spot network (Institute of Petroleum Engineering Heriot-Watt, 2010)	31
4.2	Reservoir geometry.	34
4.3	Pressure field; slice plots (Model including gravity).	43
4.4	Bottomhole pressure of the two wells (Model including gravity).	44
4.5	Average reservoir pressure (Model including gravity).	44

LIST OF FIGURES

4.6	Velocity field at the 2400th day; arrow volume plot (Model including gravity).	45
4.7	Velocity field; arrow volume plot. Zoom in injection well at two different times (Model including gravity).	46
4.8	Isosurfaces for the saturation evolution of the wetting phase (Model including gravity).	47
4.9	Average phase saturations (Model including gravity).	48
4.10	Oil production rate (Model including gravity).	49
4.11	Water production rate (Model including gravity).	50
4.12	Pressure field; slice plots (Model neglecting gravity).	52
4.13	Bottomhole pressure of the two wells (Model neglecting gravity).	53
4.14	Average reservoir pressure (Model neglecting gravity).	53
4.15	Velocity field; arrow volume plot (Model neglecting gravity).	54
4.16	Velocity field; arrow volume plot. Zoom in injection well at two different times (Model neglecting gravity).	55
4.17	Isosurfaces for the saturation evolution of the wetting phase (Model neglecting gravity).	56
4.18	Average phase saturations (Model neglecting gravity).	57
4.19	Oil production rate (Model neglecting gravity).	58
4.20	Water production rate (Model neglecting gravity).	59
4.21	Comparison of oil production rate with the two COMSOL models and ECLIPSE 100.	60
4.22	Comparison of cumulative oil production with the two COMSOL models and ECLIPSE 100.	61
4.23	Comparison of watercut at production well with the COMSOL models and ECLIPSE 100.	62

LIST OF FIGURES

4.24 Comparison of cumulative water production with the two COMSOL models and ECLIPSE 100.	62
5.1 Field pressure regime; slice plots.	76
5.2 Field average pressure.	77
5.3 Bottomhole pressure of the two wells.	77
5.4 Velocity field; arrow surface plot.	78
5.5 Saturation evolution of the water phase at different times; isosurface plots.	79
5.6 Oil production rate.	80
5.7 Solution gas production rate.	81
5.8 Water production rate.	82
5.9 Comparison of oil production rate with the two simulators.	83
5.10 Comparison of cumulative oil production with the two simulators.	83
5.11 Comparison of solution gas production rate with the two simulators. . . .	84
5.12 Comparison of cumulative solution gas production with the two simulators.	85
5.13 Comparison of watercut at production well with the two simulators. . . .	86
5.14 Comparison of water total production with the two simulators.	86

List of Tables

3.1	Parameters for the pore-scale modeling.	17
3.2	Hydrodynamic dispersion coefficient at different times in the pore-scale modeling.	23
3.3	Dispersion coefficient at different times.	25
3.4	Parameters for the REV-scale modeling.	25
3.5	Hydrodynamic dispersion coefficients at different times for the two models.	29
4.1	Intrinsic permeability in x,y,z directions for the two-phase incompressible flow models.	35
4.2	Water and oil relative permeability for the two-phase incompressible flow models.	35
4.3	Parameters for the two-phase incompressible flow models.	36
4.4	Variables for the two-phase incompressible flow models.	36
4.5	Velocity components for the model including gravity.	37
4.6	Pressure for the model including gravity.	37
4.7	Velocity components for the model neglecting gravity.	39
4.8	Pressure for the model neglecting gravity.	39

LIST OF TABLES

5.1	Phase relative permeability fractions vs water saturation for the black oil model.	69
5.2	Oil phase properties.	70
5.3	Water phase properties.	70
5.4	Parameters for the black oil model.	71
5.5	Variables for the black oil model.	72